12-15-2006

Nanocrystalline Transition Metal Ferrites Synthesis, Characterization and Surface Functionalization

Daniela Caruntu
University of New Orleans

Nanocrystalline Transition Metal Ferrites: Synthesis, Characterization and Surface Functionalization

A Thesis

Submitted to the Graduate Faculty of the

University of New Orleans

In partial Fulfillment of the

Requirements for the Degree of

Doctor of Philosophy

in

Chemistry

By

Daniela Caruntu

B. S. "Alexandru Ioan Cuza" University, Iasi, Romania, 1993
M. Sc. University of New Orleans, 2003

December 2006

ACKNOWLEDGEMENTS

This thesis is the result of the work performed at the Advanced Materials Research Institute (AMRI) at the University of New Orleans. I am indebted to several individuals from both AMRI and Chemistry Department at the University of New Orleans who helped me in successfully completing my doctoral training.

First, I thank my graduate advisor, Dr. Charles J. O'Connor, for accepting to supervise this thesis, for his support, kindness and insightful knowledge in the field.

I would also like to thank the members of my scientific committee, Dr. John B. Wiley, Dr. Kevin Stokes, Dr. Weilie Zhou and Dr. Michael Harmjanz, for their useful suggestions and feedback during the preparation of this thesis.

Dr. Vladimir Kolesnichenko was a key contributor in the early stages of this work. I appreciate his contribution as well as his assistance in answering my numerous questions about the colloidal chemistry, getting me started in the lab and for his help in optimizing the experimental conditions.

I am also indebted to Dr. Andriy Vovk for the useful discussions on modeling and interpreting the magnetic properties of the nanoparticles. We gratefully acknowledge the financial support of this work by Advanced Materials Research Institute and Department of Defense and DARPA through Grant No. HR0011-04-C-0068. I am grateful for help, assistance and friendship of the past and present members of the O'Connor group.

Last, but certainly not least, I express my gratitude to my husband, Gabriel and my son Paul Daniel for their patience, support and understanding during the preparation of this work.

TABLE OF CONTENTS

LIST OF TABLES

LIST OF FIGURES

LIST OF SCHEMES

ABSTRACT

In this thesis, a new synthetic methodology for the high yield synthesis of spinel-type transition metal ferrite nanoparticles has been developed. This approach is based on the complexation of the first-row transition metal cations with diethylene glycol (DEG) followed by the hydrolysis of the resulting chelate iron alkoxide complexes in the presence of an alkaline hydroxide. Due to the passivation of their surfaces with DEG molecules, the as-prepared nanoparticles are stable against agglomeration and can be easily dispersed in polar protic solvents (water, alcohols, etc.). Alternatively, a post-synthesis passivation with carboxylate ions can render the iron oxide nanocrystals highly dispersible in non-polar solvents. Optimization of the reaction conditions suggested that the size of the nanocrystals could be controlled by changing the complexing strength of the reaction medium. This hypothesis was verified in the case of the Fe_3O_4 nanoparticles: their sizes vary from 5.7 nm when the reaction is performed in neat diethylene glycol to 16.8 nm in *N*-methyl diethanolamine (NMDEA), whereas a 1:1 (%wt) mixture of these solvents yields nanocrystals with an average size of and 12.7 nm. A detailed characterization by using a wide variety of techniques, including powder X-Ray diffraction, IR spectroscopy, thermogravimetric analysis (TGA), transmission electron microscopy (TEM) and ^{1}H-NMR spectrometry was performed in order to elucidate the composition and the morphology of the variable-sized iron oxide nanoparticles. Both finite size and interparticle interaction effects were identified to influence the magnetic behavior of the oleate-capped nanosized particles. At low temperatures the Fe_3O_4 nanocrystals exhibit a ferromagnetic behavior with blocking temperatures which increase with the average particle size, whereas at room temperature, except for the largest nanoparticles, they undergo a superparamagnetic relaxation. We exploited the high surface reactivity of the 10 nm Fe_3O_4 nanoparticles to attach 2-3 nm gold grains to their surfaces through a simple, two-step chemically controlled procedure. By chemically bonding bioactive molecules to the attached Au nanoparticles these novel nano-architectures open up new opportunities for the implementation of the magnetic nanoparticles as a platform for various applications in the biomedical field.

CHAPTER 1

Introduction

1.1. Preface

Spinel-type iron oxides have been long used in various practical applications due to their natural occurrence and spontaneous magnetism. The attractive properties of the lodestone, a naturally-occurring Fe_3O_4 mineral, were first exploited in the ancient China (circa 1100 A.D) for the design of the magnetic compass[1]; a simple device which was used for many centuries in navigation and the discovery of new continents. Since then, the spinel-type iron oxides identified themselves as one of the most important families of technological materials for the mankind. Ferrites have always been a part of the human life, being traditionally used as pigments, catalysts or permanent magnets. Thus, it is not surprising that their technological importance increased continuously as many discoveries required the use of magnetic materials. However, the scientific and technological potential of ferrites was not completely unfolded since when they were introduced in the late 50's in the design of transformers and the non-reciprocal circuit elements.[2] Later, the ferrofluid technology introduced by NASA exploited the ability of the colloidal suspensions of micron-sized ferrite particles to combine the rheological proprieties of the liquids with the magnetism of the crystalline bulk ferrite materials for various applications such as sealing, position sensing as well as the design of actuators.

As such a tremendous technological progress in electronics was inevitably accompanied by the development of computing, transportation and non-volatile data

storage technologies, miniaturization of the electronic devices became critical, thereby leading to the reduction of the size of the magnetic materials to dimensions comparable to those of the atoms and molecules. At this point, nanoscale ferrites have found enormous potential applications in medicine and life sciences, since it is well known that many living organisms, from bacteria to vertebrates incorporate magnetic crystals. As an example, magnetite crystals were found in magnetosomes[3], whereas trace amounts of magnetite nanoparticles have been identified in the brain of fishes[4] and birds[5-6]. Magnetite crystals found in animals usually range from 40 to 100 nm and serve for navigation and their orientation with respect to the geomagnetic field. Due to very low toxicity and possesses high stability in physiological fluids and easy manipulation with a magnetic field, magnetite particles conjugated with biomolecules are the ideal candidates for the development of new strategies in the detection, diagnosis and treatment of various diseases. With all these exciting new biomedical applications to be developed in the next decade, the synthesis of ferrite nanoparticles with controllable dimensionality and tailorable magnetic properties, their functionalization with biomolecules along with the understanding of the structure-proprieties correlations have become of topics of fundamental scientific importance.

In this chapter we examine the structure of the spinel-type ferrites and the correlation with their magnetic properties. Additionally, we provide a comprehensive overview of the most important synthetic approaches, both physical and chemical, used in the preparation of nanocrystalline transition-metal ferrites.

1.2. The Spinel Structure of Ferrites

Ferrites are mixed oxides with general formula AB_2O_4, where A is a metal ion with +2 valence and B is the Fe^{+3} ion. They have a spinel-type structure similar to that of the mineral "spinel", $MgAl_2O_4$. In a typical spinel lattice, the voluminous oxide ions (r_O^{2-}=124 pm)[6] adopt a cubic close-packed arrangement, thereby forming two different types of sites, *i.e.*, tetrahedral (A) and octahedral (B). The interstitial sites are schematically represented in Figures 1.1(a) and 1.1(b).[7]

Spinel compounds possess a cubic unit cell which can be regarded as built of eight smaller cubes called octants or formula units (Figure 2a), corresponding to the formula of "$A_8B_{16}O_{32}$". Accordingly, the spinel unit cell contains 32 oxide ions, 64 tetrahedral sites and 32 octahedral sites. In order to achieve a charge balance of the ions, the interstitial voids will be only partially occupied by positive ions. Therefore, in stoichiometric spinels, only one-eighth of the tetrahedral sites and one-half of the octahedral sites are occupied by metal ions. There are two types of octants which alternate in the unit cell of a spinel crystal (Figure 1.2b). The A^{2+} ions are located at the centers of the A-type octants and are tetrahedrally coordinated by four oxide ions occupying half the corners of these small cubes. In addition, the A^{2+} ions lie at the corners and the face centers of the spinel unit cell. The B-type octants contain the B^{3+} ions in the octahedral interstitial sites so that half the corners are occupied by the trivalent metal ions and the other half by the oxide ions.[7, 8]

Depending on the cation distribution over the different crystallographic sites, the spinel compounds can be generally classified into two categories: normal and inverse spinels. Normal spinels have the general formula $A^t(B_2)^oO_4$ and contain all the trivalent

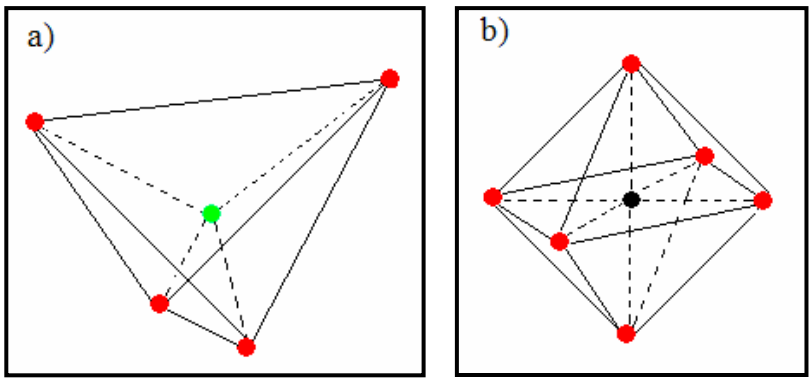

Figure 1.1 A tetrahedral site (a) and an octahedral site (b); the solid red spheres represent the oxide ions (O^{2-}), whereas the green and black spheres correspond to the divalent (A^{2+}) and trivalent (B^{3+}) cations.

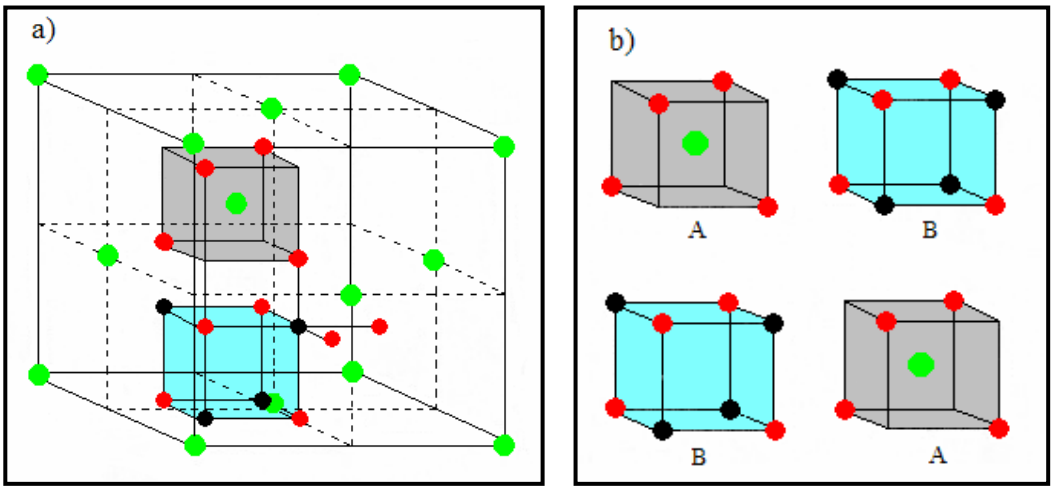

Figure 1.2. The cubic unit cell of spinels (a); the A-type octants alternating with the B-type octants in the spinel unit cell (b)[7-8]

metal ions (B^{3+}) in the octahedral sites (o), whereas all the divalent metal ions (A^{2+}) reside in the tetrahedral sites (t). Transition metal ferrites, such as $ZnFe_2O_4$ and $CdFe_2O_4$, assume the normal spinel structure. This structure is also adopted by some oxides containing Al^{3+} (MAl_2O_4, M^{2+}= Mg^{2+}, Fe^{2+}, Co^{2+}, Zn^{2+}), Co^{3+} (MCo_2O_4, M^{2+}= Zn^{2+}, Co^{2+}), Cr^{3+} (MCr_2O_4, M^{2+}= Mg^{2+}, Mn^{2+}, Ni^{2+}, Fe^{2+}, Co^{2+}, Cu^{2+}, Zn^{2+}), and Mn^{3+} (MMn_2O_4, M^{2+}= Mg^{2+}, Mn^{2+}, Co^{2+}, Cu^{2+}, Zn^{2+}) as trivalent metal ions. Additionally, a large number of sulphides, selenides, and tellurides possess the normal spinel structure. In the inverse spinels, the divalent cations (A^{2+}) and half of the trivalent cations (B^{3+}) occupy the octahedral sites, whereas the other half of the B^{3+} metal ions lie in the tetrahedral sites. Most of the first series transition metal ferrites, such as $NiFe_2O_4$, $CoFe_2O_4$, Fe_3O_4, and $CuFe_2O_4$, are inverse spinels; their site occupancy can be described by the general formula $B^t(AB)^oO_4$. Some other spinel compounds posses the divalent and the trivalent metal ions randomly distributed over both the tetrahedral and the octahedral interstices. These compounds are named mixed spinels and their composition is best represented by the general formula $(A_{1-\gamma}B_\gamma)^t(A_\gamma B_{2-\gamma})^oO_4$, where the inversion parameter, γ, denotes the fraction of the trivalent cations (B^{3+}) residing in the tetrahedral sites. Mixed spinels occur in a wide range of compositions and are usually considered as intermediate compounds between the two extreme cases, *i.e.*, normal and inverse spinels. Representative ferrites adopting the mixed spinel structure include $MgFe_2O_4$ and $MnFe_2O_4$. Since magnesium ferrite contains 10% of the Mg^{2+} ions in the tetrahedral interstices and 90% in the octahedral interstices, according to the above mentioned formula, the cation distribution can be described as $(Mg_{0.1}Fe_{0.9})^t(Mg_{0.9}Fe_{1.1})^oO_4$. Manganese ferrite, with 80% of the Mn^{2+} ions occupying the tetrahedral holes and 20%

occupying the octahedral holes, can be written as $(Mn_{0.8}Fe_{0.2})^{t}(Mn_{0.2}Fe_{1.8})^{o}O_4$. Therefore, the inversion parameter is 0.9 for $MgFe_2O_4$ and 0.2 for $MnFe_2O_4$. Usually, γ varies between 0 (for normal spinel compounds) and 1 (for inverse spinels); the inversion parameter can also take intermediate values ($0<\gamma<1$) and the corresponding ferrites adopt a mixed spinel structure characterized by a random occupancy of the tetrahedral and octahedral sites by the divalent (A^{2+}) and trivalent (B^{3+}) cations[7, 9].

The problem of site occupancy in spinels is not a trivial one since most of their properties are strongly dependent on the cation distribution. Several factors, both structural and experimental, have been identified in determining the coordination preference of the two metal ions, A^{2+} and B^{3+}, in spinel crystals[8]. One of them refers to the relative sizes of the divalent and trivalent cations. According to Shannon and Prewitt set of ionic radii determined from X-ray diffraction measurements (based on $r_{O^{2-},\,oct.}$=126 pm), the divalent metal ions encountered in 2,3 oxide spinels have octahedral radii ranging from 83 pm to 97 pm.[6] It was experimentally observed that the ionic radii vary with coordination number. For example, the radius of Mg^{2+} ion changes from 86 pm (when octahedrally coordinated) to 71 pm (for tetrahedral coordination). This is a consequence of the fact that ions are elastic and their outer sphere, characterized by a lower electron density, can be deformed with a certain extent depending on the coordination number and the nature of the surrounding anions.[7] The trivalent metal ions usually found in 2, 3 oxide spinels are Al^{3+}, Cr^{3+}, Co^{3+}, Mn^{3+}, and Fe^{3+} and their radii vary between 68 pm and 81 pm.[6] Since the cations bearing a higher positive charge are smaller than those with a lower charge, it is expected that the trivalent cations (B^{3+}) will occupy the smaller interstitials sites, *i.e.*, the tetrahedral sites, leaving the larger

octahedral sites available for the divalent cations (A^{2+}). This is not the case of normal spinels like $MgAl_2O_4$ where the larger Mg^{2+} ions (86 pm/71 pm, $r_{oct.}/r_{tet.}$) lie in the smaller tetrahedral sites, whereas the smaller Al^{3+} ions (67.5 pm/53 pm, $r_{oct.}/r_{tet.}$) occupy the larger octahedral sites. Similarly, other bulk materials, such as $ZnFe_2O_4$ and $CdFe_2O_4$, contain in their tetrahedral holes the larger, nonmagnetic Zn^{2+} (88 pm/71 pm, $r_{oct.}/r_{tet.}$) and Cd^{2+} (109 pm/92 pm, $r_{oct.}/r_{tet.}$) ions, whereas the octahedral holes are occupied by the smaller Fe^{3+} ions (78.5 pm/63 pm, $r_{oct.(HS)}/r_{tet.}$).

The ratio of the cation to anion radius (r_{cation}/r_{anion}), known as the Pauling's radius ratio rule, can also be used as a tool to predict the coordination preference of the metal ions in ionic crystals. However, the radius ratio rule was applied successfully only for a limited number of the investigated compounds. According to this rule, the metal ions will occupy preferentially the tetrahedral sites if the calculated radius ratios fall within the range 0.225-0.414. If the ratios of the ionic radii vary between 0.414 and 0.732, the cation will have preference for octahedral sites. Coordination numbers of eight are predicted for metal ions when the ratios take values between 0.732 and 1.00.[7, 9] In 2, 3 oxide spinels, each oxide ion (O^{2-}) is surrounded by four ions of opposite charge. For example, in $MgAl_2O_4$ each oxide ion has a four-fold coordination being surrounded by three trivalent cations (Al^{3+}) and one divalent cation (Mg^{2+}). Therefore, calculation of the radius ratio (r_{cation}/r_{anion}) is performed using the value of 124 pm (given by Shannon and Prewitt) for the radius of tetrahedrally coordinated oxide ion. For metal ions, both the tetrahedral and the octahedral radii are taken into account in determining the radius ratio and hence the crystallographic site preference. For Mg^{2+} ion, the calculated radius ratios are 0.573 ($r_{Mg^{2+},\,tet.}/r_{O^{2-}}$; $r_{Mg^{2+},\,tet.}$= 71 pm) and 0.694 ($r_{Mg^{2+},\,oct.}/r_{O^{2-}}$; $r_{Mg^{2+},\,oct.}$= 86 pm),

respectively. Since the obtained values fall within the range 0.414-0.732, according to the radius ratio rule, it is expected that the Mg^{2+} ions will occupy the octahedral sites inside the spinel crystal. The radius ratios of the Al^{3+} ion with O^{2-} ion are 0.427 ($r_{Al^{3+},\,tet.}/r_{O}^{2-}$; $r_{Al^{3+},\,tet.}$= 53 pm) and 0.544 ($r_{Al^{3+},\,oct.}/r_{O}^{2-}$; $r_{Al^{3+},\,oct.}$= 67.5pm), respectively. These values are lower than those obtained for the Mg^{2+} ion and they approach the borderline (0.414) between the two types of coordination. Therefore, the Al^{3+} ions might occupy both the tetrahedral and octahedral voids. Using the Pauling's ionic radii, the ratio of the radii for Mg^{2+} ion (65 pm) and O^{2-} ion (140 pm) was found to be 0.464. Regardless of the set of radii used, the calculated radius ratios for the Mg^{2+} ions clearly show their preference for octahedral sites. With Mg^{2+} ions in the octahedral sites and Al^{3+} ions distributed over both the tetrahedral and the octahedral sites, $MgAl_2O_4$ would adopt an inverse spinel structure. These results are not consistent with the real structure of the natural $MgAl_2O_4$ which is a normal spinel.

Similar results were obtained for $ZnFe_2O_4$. The ratios of the cation (Zn^{2+}) to anion (O^{2-}) are 0.597 ($r_{Zn^{2+},\,tet.}/r_{O}^{2-}$; $r_{Zn^{2+},\,tet.}$= 74 pm) and 0.710 ($r_{Zn^{2+},\,oct.}/r_{O}^{2-}$; $r_{Zn^{2+},\,oct.}$= 88 pm), respectively. These values fit into the range from 0.414 to 0.732 showing the ability of the Zn^{2+} ion to accommodate six oxide ions as its closest neighbors. The radius ratio rule predicts an inverse spinel structure for $ZnFe_2O_4$. Indeed, the bulk material is an inverse spinel at very low temperatures, but transforms into a normal spinel at room temperature.

Another important parameter to be taken into account in examining the coordination preference of the cations in 2,3 oxide spinels is the crystal field stabilization energy (CFSE).[9] The calculated values of the crystal field stabilization energy of the divalent cations (A^{2+}) in 2,3 oxide spinels are systematically found to be higher for

octahedral sites than for the tetrahedral ones.[10] These values indicate a strong preference of the divalent cations for octahedral interstices, thereby confirming the inverse spinel type-structure observed in some compounds such as Fe_3O_4, $NiFe_2O_4$, $CoFe_2O_4$, and $CuFe_2O_4$. The Fe^{3+} (d^5) ions have no contribution in determining the type of spinel structure since their crystal field stabilization energy is zero regardless of the coordination environment. Therefore, the smaller Fe^{3+} ions (78.5 pm/63 pm, $r_{oct.(HS)}/r_{tet.}$) show no preference for a particular crystallographic site; they will be equally shared between the tetrahedral and the octahedral sites, leaving the other half of the octahedral interstices available for larger cations such as Fe^{2+} (92 pm, $0.4\Delta_0$), Co^{2+} (88.5 pm, $0.8\Delta_0$), Ni^{2+} (83 pm, $1.2\Delta_0$), and Cu^{2+} (87 pm, $0.6\Delta_0$).

In addition to the crystal field stabilization energy (CFSE), the lattice energy was found to have close connection with the cation distribution in oxide spinels. The lattice energy characterizes the stability of an ionic crystal and is usually described as a sum of three energetic terms: electrostatic, non-Coulombian, and vibrational.[11] Since the electrostatic term, expressed as $U_E = \frac{Ne^2M}{4\pi\varepsilon_0 a}$ (where M stands for the Madelung constant and a is the lattice parameter), has the biggest contribution to the lattice energy, it results that the Madelung constant will play an important role on the energetics of the ionic crystals. In general, a larger value of the Madelung constant implies a larger value of the lattice energy and, therefore, a greater stability of the crystal structure. Several approaches were proposed for the calculation of the Madelung constant in oxide spinels. For example, Thompson *et al.* described the Madelung constant as the contribution of the average cationic (from both tetrahedral (Q_t) and octahedral (Q_o) sites) and anionic (Q_{an})

charges, respectively: $M = \alpha_1 Q_o^2 + \alpha_2 Q_o Q_t + \alpha_3 Q_t^2 + \alpha_4\, Q_o Q_{an} + \alpha_5 Q_{an}^2 + \alpha_6 Q_t Q_{an}$, where α_i (i=1, 2, 3) are constants, whereas α_i (i=4, 5, 6) represent quadratic functions of the crystallographic oxygen parameter u.[12] This parameter refers to the position of the oxide ions in the spinel lattice and can be accurately determined by structure refinement of the laboratory diffraction data. The dependency of the Madelung constant on the oxygen parameter u in simple oxide spinels was investigated by O'Neill and Navrotsky.[11] By plotting the values of the Madelung constant as a function of the oxygen parameter, they observed that M increases for normal 2,3 oxide spinels, whereas for normal 4,2 oxide spinels M decreases as u increases (Figure 1.3). The Madelung constant for inverse 2, 3 and 4,2 oxide spinels follows an opposite trend as compared to the normal spinel structures. For each type of oxide spinels, the curves corresponding to the normal and inverse structures intersect at a certain value of u, where the energetics of the crystal impose a change in the cation arrangement. Therefore, at a value of u=0.2555 the structure of 2,3 oxide spinels changes from inverse to normal, whereas for 4,2 oxide spinels the structure changes from normal to inverse at u=0.2625. These results are in good agreement with the classification of oxide spinels proposed by Hill *et al.* who describe Fe_3O_4 as an inverse spinel with a value of the oxygen parameter equal to 0.2548 and $ZnFe_2O_4$ as a normal spinel with a calculated u value of 0.2615.[13]

The structural parameters previously mentioned are not the only ones affecting the cation distribution in bulk 2,3 oxide spinels. Other factors which influence significantly the site occupancy in these compounds include the preparation method and the thermal history of the sample. Along with the particle size, these two parameters were also found to affect the site occupancy in nanostructured ferrites.

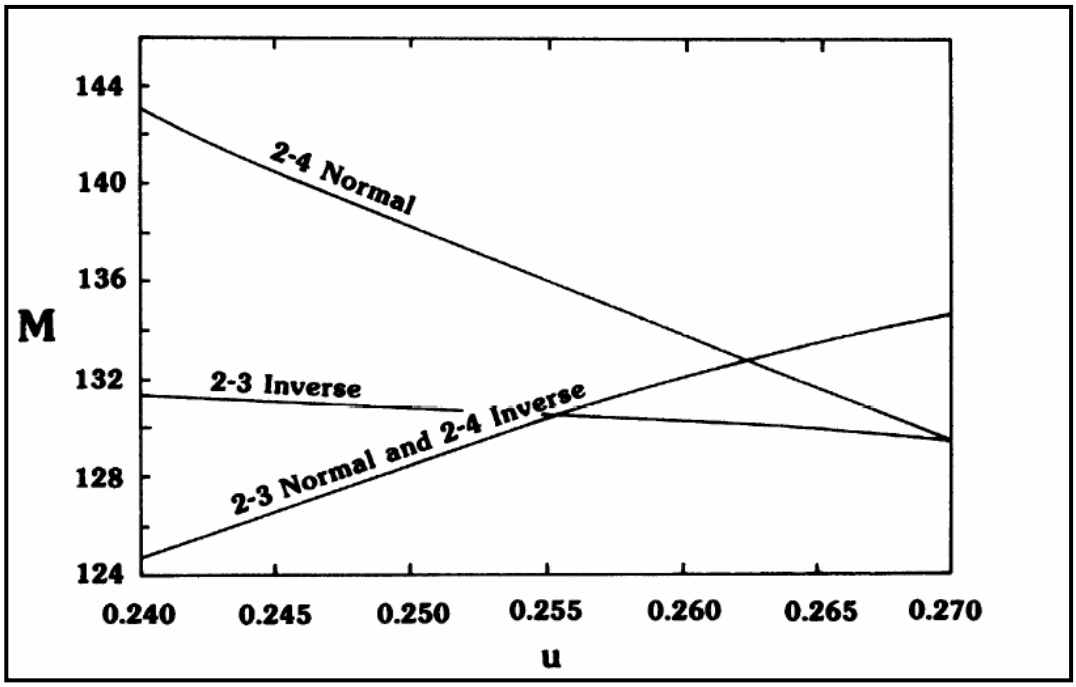

Figure 1.3 Oxygen parameter (u) dependence of the Madelung constant (M) for 2,3 and 4,2 oxide spinels [Ref.11].

A common feature of the ferrite nanomaterials is that they usually adopt a mixed spinel structure, $(A_{1-\gamma}Fe_{\gamma})^{t}(A_{\gamma}Fe_{2-\gamma})^{o}O_4$, characterized by the presence of divalent (A^{2+}) and trivalent (Fe^{3+}) cations in both crystallographic sites. In general, the inversion parameter (γ) of a given nanostructured ferrite is quite different from that of the bulk counterpart and varies with the preparation method. Ho *et al.* reported the preparation of 14nm-sized $ZnFe_2O_4$ particles by an aerogel or supercritical sol-gel method. The resulting nanocrystals have a mixed spinel structure with an inversion parameter of 0.205. If the as-prepared $ZnFe_2O_4$ nanopowders are subjected to a ball milling process, their size increases to about 40 nm, leading also to an increase of the inversion parameter to 0.55.[14] A lower value of the inversion parameter (γ=0.07) was reported for $ZnFe_2O_4$ nanoparticles produced by the ball milling (mechanosynthesis) process using ZnO and α-Fe_2O_3 as precursor materials. Ball milling followed by annealing (air, 1h) at temperatures up to 300° C led to an increase of the particle size from 30.6 nm to 50.6 nm. The coarsening process undergone by the as-prepared nanostructured material is accompanied by the variation of the inversion parameter from 0.07 to 0.163.[15] Kamiyama *et al.* examined the cation distribution in nanosized $ZnFe_2O_4$ particles obtained by coprecipitation method and observed that the inversion parameter decreases as the particle size increases. Variable-sized $ZnFe_2O_4$ nanoparticles were obtained by annealing (air, 1h) of the as-prepared nanopowders at 500° C and 700° C, respectively. Structure refinement of the neutron diffraction data revealed that the smaller particles (26 nm) have an inversion parameter of 0.142, whereas for the larger ones (96nm) the inversion parameter is 0.108.[16]

However, the variation of the inversion parameter with particle size does not always follow the same trend. Both the increase and the decrease of the inversion parameter with particle size have been reported in the literature. When ferrite nanopowders undergo post-synthesis heat treatments the particle size increases. This process is accompanied by the diffusion of the divalent and trivalent cations between the A and B sites leading to a change in the inversion parameter as compared to the as-prepared material. Such a change in the cation distribution presumably depends on several factors including the annealing temperature, the heating rate as well as rate at which the annealed sample is cooled down to room temperature.[9]

Particle size dependence of the inversion parameter was also reported for $ZnFe_2O_4$ particles obtained by forced hydrolysis in polyol medium. Differently sized $ZnFe_2O_4$ particles with mixed spinel structure were obtained by changing both the molar ratio water to metal (h) and the nature of the polyol. Interestingly, the variation of the reaction parameters caused a change not only in the particle size, but also in the cation distribution. Thus, the inversion parameter was found to decrease from 0.25 to 0.15 as the particles increases from 6.6nm (polyethylene glycol, h=6.7) to14.4 nm (diethylene glycol, h=0.7).[17]

1.3. Synthesis of the Nanocrystalline Ferrites

Bulk ferrites have been traditionally prepared by solid state reactions consisting in a succession of heat treatments/intermediate regrindings of stoichiometric mixtures of powdered precursors. Although this conventional “shake and bake” route is cheap and easily scalable, the slow rate of diffusional processes necessitates prolonged annealings at

relatively high temperatures resulting in a very limited control over the morphology of the reaction products.

Translation of the dimensions of ferrites to the nanometer scale can be achieved through a wide variety of methods, both physical and chemical. The physical methods are "top-down" strategies in which high purity powders of bulk precursor materials are transformed into nanocrystalline ferrites by a mechanical, mechano-chemical or laser-assisted process. Although they are simple, inexpensive and easily scalable, physical methods present limited control over the morphology and/or chemical composition of the final products. Conversely, solution-based chemical methods are "bottom-up" approaches where nanoparticles are produced via chemical reactions between sub-nanometer reactive species, such as atoms or molecules. Depending on the nature of the solvent used, solution-based chemical methods are classified into two main categories: aqueous solution-based techniques and non-aqueous techniques.

1.3.1. Preparation of Nanostructured Ferrites by Physical Methods

Physical methods employing the high-energy ball milling technique are widespread used in the preparation of nanostructured ferrite materials. These methods can be generally classified into three categories: mechanical activation, mechano-chemical synthesis (mechanosynthesis) and mechanical alloying.

Mechanical activation refers to the grinding of bulk ferrite material in planetary ball mills until the grain size reaches the nanometer scale. The bulk ferrites used as precursor materials in the ball-milling process were obtained by a conventional thermal (ceramic) method from mixtures of a divalent metal oxide (MO, M^{2+}=Mg^{2+}, Mn^{2+}, Ni^{2+},

Zn^{2+}) and α-Fe_2O_3. In order to obtain ferrite materials with nanocrystalline structure, the mechanical milling experiments were performed in air for all ferrites investigated (Table 1A), except for $MnFe_2O_4$, which was ball-milled under argon atmosphere. Kedesdy *et al.* showed that $MnFe_2O_4$ reacts with O_2 in the air at temperatures around 300ºC with the formation of the corresponding trivalent metal oxide: [18]

$$2MnFe_2O_4 + \frac{1}{2}O_2 \rightarrow 2Fe_2O_3 + Mn_2O_3$$

Indeed, X-ray diffraction measurements used to investigate the phase purity of the obtained ferrite nanopowders confirmed the formation of more than one phase when the ball milling of $MnFe_2O_4$ is carried out in air.[19] For the other ferrites ($ZnFe_2O_4$, $NiFe_2O_4$, $MgFe_2O_4$) mechanical milled in air, the reflections in X-ray diffractograms can all be assigned to a cubic spinel structure.

In general, one of the shortcomings of the physical methods is related to the limited number of parameters which can be varied in order to achieve a better control over the morphology of the resulting nanopowders. In the mechanical activation process, the average grain size of the ferrite powders could be tuned by varying the milling time. Chinnasamy *et al.* showed that the average grain size of the $NiFe_2O_4$ powders, determined from X-ray diffraction measurements, decreases from 60 nm to 10 nm as the milling time increases from 1 h to 30 h.[20] Mahmoud *et al.* observed a similar behavior for $MnFe_2O_4$ powders prepared by mechanical activation. Increasing the milling time from 10 min to 3 h decreased the particle size from 200 nm to 82 nm. A close examination of the TEM micrograph revealed a relatively small number of individual, roughly sherical

Table 1.1. Survey of Nanostructured Ferrites Prepared by Physical Methods
A) Mechanical Activation (Ceramic method/ Ball Milling Bulk Material)

Ferrite (MFe_2O_4)	Starting/Precursor Material	Conditions	Size (nm) TEM/XRD	Ref.
$MnFe_2O_4$	a) MnO, α-Fe_2O_3	a) ceramic: air, 900°C (12h), 1150°C (20h)	200 (10')	19
			120 (30')	
	b) Bulk $MnFe_2O_4$	b) ball milling: Ar, 10', 30', 120', 180'	90 (120')	
			82 (180')	
$ZnFe_2O_4$	a) ZnO, α-Fe_2O_3	a) ceramic	-	23
	b) Bulk $ZnFe_2O_4$	b) ball milling: air, 5', 12', 24'		
$MgFe_2O_4$	a) MgO, α-Fe_2O_3	a) ceramic: 1200K (24h), 1300K (24h)	-	21, 22
	b) Bulk $MgFe_2O_4$	b) ball milling: air, 750rpm 15', 30'		
$NiFe_2O_4$	a) NiO, α-Fe_2O_3	a) ceramic	60 (1h)	20
			40 (6h)	
	b) Bulk $NiFe_2O_4$	b) ball milling: air, 1h, 6h, 20h, 30h	15 (20h)	
			10 (30h)	

B) Mechano-Chemical Synthesis (Ball Milling Precursor and/or Heat Treatment)

Ferrite (MFe_2O_4)	Starting/Precursor Material	Conditions	Size (nm) (XRD)	Ref.
$CoFe_2O_4$	a) $Co(NO_3)_2{\cdot}6H_2O$ $Fe(NO_3)_3{\cdot}9H_2O$ Na_2CO_3	a) coprecipitation: pH=9, ultrasonication (1h, RT)	5.1 (5h), 8.6 (10h), 12.2 (15h)	31
	b) $CoFe_2(OH)_4(CO_3)_2 \cdot nH_2O$	b) ball milling: 5h, 10h, 15h		
$ZnFe_2O_4$	a) ZnO, α-Fe_2O_3	a) ball milling: 1320h, acetone	a) 36.6	15
	b) nanosized $ZnFe_2O_4$	b) annealing: air, 1h, 300°C	b) 50.6	
$NiFe_2O_4$	a) NiO, α-Fe_2O_3	a) ball milling: air, 10h, 35h, 50h	6 (50h)	30
	b) nanosized $NiFe_2O_4$	b) annealing: air, 1h, 1100°C		

Table 1.1. Survey of Nanostructured Ferrites Prepared by Physical Methods
C) Mechanical Alloying (Ball milling Precursor and/or Heat Treatment)

Metal ferrite	Starting/Precursor Material	Conditions	Size (nm) (XRD)	Ref.
$NiFe_2O_4$	a) $FeCl_3$, $NiCl_2$, NaOH, NaCl b) $Fe(OH)_3$, $Ni(OH)_2$	a) coprecipitation: RT b) ball milling: 30h (200pm), 30h, 33h (300rpm)	10	32
$Co_{0.5}Fe_{2.5}O_4$	Co_3O_4, Fe_3O_4	a) ball milling: Ar, 30h b) annealing: -vacuum (750°C, 0.5h) - in air (200°C, 2h) - magnetic (He, 30kOe, 1h 300°)	25	33
$Co_{0.8}Fe_{2.2}O_4$	Co_3O_4, Fe_3O_4	a) ball milling: air, 24h b) annealing: - in air (500-1000°C, 1h) - magnetic (30kOe, 2h, 300°C)	30 (750°C) 50 (1000°C)	34

nanoparticles as well as a large number of aggregates. The aggregated appearance of the $MnFe_2O_4$ nanoparticles made difficult the accurate determination of the average particle size from electron microscopy measurements.[19]

The high-energy ball milling process induces the diffusion of the divalent (M^{2+}) and trivalent (Fe^{3+}) metal ions between the two sublattices of the spinel structure, which results in a change of the inversion parameter, γ, of the obtained nanopowders as compared with the bulk material. It was also observed that the inversion parameter varies differently with the particle size depending on the type of spinel structure adopted by the bulk ferrites. For instance, the inversion parameter of the mixed spinel $MnFe_2O_4$ increases from 0.23 (corresponding to the bulk material) to 0.45 (for 82 nm-sized particles).[19] In the case of bulk $NiFe_2O_4$ which adopts an inverse spinel structure, the reduction of the grain size during the mechanical milling process is accompanied by a decrease of the inversion parameter from 1 (for the bulk material) to 0.94 (for 10 nm-sized particles).[20] A similar behavior was reported by Šepelák *et al.* for mixed spinel $MgFe_2O_4$. While the bulk, nonactivated material had an inversion parameter of 0.904, the nanopowders obtained after mechanical activation (approximately 10nm in size) were characterized by a γ value of 0.756.[21,22] As compared to the other ferrites presented in Table 1A, bulk $ZnFe_2O_4$ underwent a significant alteration of the cation distribution during the ball milling process. The Mössbauer measurements revealed a strong increase of the inversion parameter, γ from 0 (for the bulk $ZnFe_2O_4$) to 0.94 (for the ferrite nanopowders obtained after mechanical milling). Therefore, as the grain size is reduced, the normal spinel structure of the bulk $ZnFe_2O_4$ transforms into a mixed spinel phase characterized by a large occupancy of the tetrahedral interstices by the smaller Fe^{3+} ions.

It was observed that the change in the spinel-type lattice is accompanied by shrinkage of the ferrite unit cell. Using the X-ray diffraction measurements to determine the unit cell size of $ZnFe_2O_4$ before and after ball milling, Šepelák *et al.* noted that the lattice parameter, a, decreased from 0.84432 nm to 0.84136 nm as the fraction of the Fe^{3+} ions residing in the tetrahedral interstices increases.[23] A similar relationship between the site occupancy in ferrites and the lattice parameter was reported by Mozzi and Palladino for nonstoichiometric magnesium ferrite with formula $Mg_{1.06}Fe_{0.94}O_{3.97}$. The authors observed that the lattice parameter decreased from 8.398 Å to 8.385 Å with decreasing the fraction of larger divalent metal ions (Mg^{2+}) in the tetrahedral interstices.[24]

By studying the influence of temperature on the cation distribution in nanosized Mn-Fe ferrite, Zhang *et al.* also noted a dependence of the lattice parameter on the site occupancy in these compounds. 40 nm-sized Mn-Fe ferrite powders obtained by a coprecipitation method were subjected to a post-synthesis heat treatment at temperatures ranging from 25 to 485ºC. For the annealed samples including that obtained after cooling back to room temperature, the electron microscopy measurements showed no significant changes in the nanoparticle morphology. Investigation of the cation distribution in these samples by neutron diffraction followed by Rietveld refinement revealed a decrease of the inversion parameter from 0.61 to 0.39 as the nanopowders were annealed from room temperature to 363ºC. No meaningful changes in the cation distribution (γ=0.38) occurred when the Mn-Fe ferrite sample was further heated to 485ºC. This indicated that the nanoparticulate Mn-Fe ferrite system attained an equilibrium state which was maintained even after cooling the powdered sample back to room temperature. The authors attributed the slight decrease of the inversion parameter (from 0.38 to 0.29)

during the cooling process to the errors associated with the refinement of the experimental data using the Rietveld method. The change in the site occupancy during the heat treatment was accompanied by a small variation of the lattice parameter. X-ray diffraction measurements indicated an increase of the lattice parameter from 8.4811(3)Å to 8.4884(2)Å as the inversion parameter decreased from 0.61 ($Mn_{0.39}Fe_{0.61}(Mn_{0.82}Fe_{1.18})O_4$) to 0.29 ($Mn_{0.71}Fe_{0.29}(Mn_{0.39}Fe_{1.50})O_4$). The slight variation of the lattice parameter during the post-synthesis heat treatment was explained by taking into account the iron (III)-oxygen bond length as well as the oxidation state of the manganese in the Mn-Fe ferrite nanopowders. The iron (III)-oxygen bond length in ferrite spinels is a function of cation coordination environment, *i.e.*, tetrahedral or octahedral. Since this bond is shorter when the trivalent cation is tetrahedrally coordinated, a larger occupancy of the tetrahedral interstices by the Fe^{3+} (a larger γ value) can result in a slight shrinkage of the unit cell. The evolution of the oxidation state of manganese during the thermal treatment in vacuum is consistent with the observed variation of the lattice parameter. As determined from the electron energy loss spectroscopy (EELS) measurements, the mixture of the Mn^{2+} and Mn^{3+} ions contained in the as-prepared ferrite nanopowder is gradually transformed into Mn^{2+} ions. Such a reductive process compensates for the loss of negative charges associated with the decrease in the oxygen content of the ferrite nanopowders when subjected to the heat treatment in vacuum. Both the small fraction of the Fe^{3+} ions residing in the tetrahedral interstices and the presence of the Mn^{2+} ions ($r_{Mn^{2+},\,tet.} > r_{Mn^{3+},\,tet.}$) explained the larger value of the lattice constant of the annealed sample compared to the as-prepared ferrite nanopowders.[25]

In addition to the morphological changes, the structural modifications undergone by the bulk ferrites during mechanical activation process were found to have a significant effect on the magnetic properties of the resulting nanostructured ferrites. The mechanically activated ferrite nanopowders have been the subject of intense studies aiming at understanding the relationship between the crystal structure of nanosized ferrites and the observed magnetic properties. The slight contraction of the unit cell observed in some of the mechanically activated ferrites causes distortions of the cation (B)-anion-cation(B) bond angle, which in turn affect the strength of the interaction between the magnetic ions occupying the octahedral (B) interstices.

Defined as the process by which the spins of two neighboring metal ions interact through an intermediate O^{2-} ion, the exchange interaction depends on both the distance between cations and the cation-anion-cation bond angle.[7, 9, 26] The bond angle dependence of the exchange interaction was confirmed by Šepelák and coworkers who reported a change in the Fe^{3+} (B)-O^{2-}- Fe^{3+} (B) interaction strength in nanocrystalline $ZnFe_2O_4$ as a result of the deformation of the corresponding bond angle during mechanical milling. The authors also noted the existence of the intersublattice exchange interactions (Fe^{3+} (A)-O^{2-}-Fe^{3+} (B)) in nanosized $ZnFe_2O_4$ as compared to the bulk material where the normal spinel structure ($[Zn]^A[Fe_2]^BO_4$) allows only the intrasublattice Fe^{3+}(B)-O^{2-}-Fe^{3+}(B) interactions.[23,27]The occurrence of the intersublattice exchange interactions in nanocrystalline $ZnFe_2O_4$ powders was attributed to the alteration of the cation distribution during the ball milling process when the normal spinel $ZnFe_2O_4$ was converted into a mixed spinel $[Zn_{0.06}Fe_{0.94}]^A[Zn_{0.94}Fe_{1.06}]^BO_4$.

In spinel crystals, the intersublattice (A-O-B) exchange interactions are stronger than the intrasublattice (A-O-A and B-O-B) interactions.[28] The spins of the magnetic ions located in the tetrahedral interstices (A) are coupled antiferromagnetically with those of the cations residing in the octahedral sites (B). The antiparallel coupling of the metal ions is mediated, in the case of metal oxides, by the diamagnetic O^{2-} ion which contains paired electrons in each of its 2p orbitals.[7, 9] The exchange interaction between metal ions having unpaired 3d electrons is strong when the cation-oxide-cation bond angle approaches 180ºC. For the intersublattice A-O-B exchange interactions (or superexchange interaction) the bond angle is 126º, whereas for the intrasublattice A-O-A and B-O-B exchange interactions the bond angles are 79º and 90º, respectively.[29] The magnetic ions occupying the same type of interstitial sites are characterized by a parallel alignment of their spins which results in a weaker ferromagnetic coupling.[26]

Since both the inter- and intrasublattice exchange interactions are present in the mechanically activated $ZnFe_2O_4$ nanopowders, these materials show much higher Néel temperature, T_N, values as compared to their bulk counterpart. Mössbauer measurements performed on both bulk $ZnFe_2O_4$ and 20 nm-sized powders prepared by mechanical milling revealed an increase of the Néel temperature from 9K (for normal spinel $ZnFe_2O_4$) to 77K (for mixed spinel $[Zn_{0.58}Fe_{0.42}]^A[Zn_{0.42}Fe_{1.58}]^BO_4$ as the grain size decreases.[28]Experimental results also showed that the Néel temperature strongly depends on the preparation method when ferrite nanopowders with similar particle size are investigated. While the mechanical activation process is limited to the grinding of the bulk ferrites pre-prepared by a solid state reaction, the mechano-chemical synthesis uses the high-energy ball milling technique to reduce the grain size of the powdered

precursors ($M^{II}O$ and α-Fe_2O_3) to the nanometer scale and to promote the reaction between the two metal oxides with the formation of nanocrystalline ferrites. The mechano-chemical syntheses (or mechanosyntheses) require long milling times to complete the reactions between the two oxide precursors and to obtain single-phase nanocrystalline ferrites (Table 1B). The X-ray diffraction measurements used to determine the phase purity of the nanopowders obtained by mechanosynthesis showed that pure nanosized $NiFe_2O_4$ was obtained only after 35 h of mechanical milling. Shorter milling times led to mixtures of $NiFe_2O_4$ and oxide precursors.[30] In most of the cases, the mechano-chemical synthesis requires a subsequent thermal treatment to improve the crystallinity and the chemical composition of the obtained ferrite nanopowders. The heat treatment process is often accompanied by an increase in the crystallite size and a change in the inversion. Neutron diffraction refinement revealed that the $ZnFe_2O_4$ nanopowders prepared by mechanosynthesis are oxygen deficient and the oxygen content can be increased by post-synthesis annealing in air at temperatures up to 300ºC.[15]

Manova *et al.* reported the preparation of nanocrystalline by ball milling induced decomposition of a layered cobalt-iron hydroxy-carbonate precursor:

$$CoFe_2(OH)_4(CO_3)_2 \cdot nH_2O \rightarrow CoFe_2O_4 + (n+2)H_2O + 2CO_2$$

The mixed metal precursor material was obtained by addition of a Na_2CO_3 solution to an aqueous mixture of the two metal nitrates, cobalt (II) nitrate and iron (III) nitrate, taken in stoichiometric amounts. Subsequent mechanical treatment of the layered mixed metal hydroxy-carbonate precursor resulted in pure 5.1 nm-sized $CoFe_2O_4$ powder after a relatively short milling time of 5 h. The transmission electron microscopy (TEM) measurements revealed the aggregated nature of these particles. Interestingly, the

crystallite size of the $CoFe_2O_4$ powders increased from 5.1 nm to 8.6 nm as the milling times increased to 10 h. Longer milling times resulted in the formation of mixtures containing cobalt ferrite and metallic cobalt.[31]

Similar to the mechano-chemical synthesis, the mechanical alloying process employs the high-energy ball milling technique to prepare nanocrystalline ferrites both by fracturing the large particles of the precursor materials and promoting the solid state reactions between the resulting nanosized powders. Mixtures of metal hydroxides or mixed metal oxides with spinel structure are usually used as precursor materials to prepared nanosized ferrites by mechanical alloying.[32-34] Shi *et al.* prepared nanostructured $NiFe_2O_4$ particles by combining the coprecipitation method, used to synthesize the precursor mixture of divalent and trivalent hydroxides, with the mechanical alloying (Table 1C). Prolonged milling (63 h) of the metal hydroxides with a large amount of NaCl (1:6, w/w) resulted in 10nm-sized $NiFe_2O_4$ particles which are subsequently subjected to annealing at 650ºC. A close examination of the TEM micrograph of the nanocrystalline $NiFe_2O_4$ prepared by mechanical alloying revealed slightly aggregated spherical particles. The morphology did not change significantly during annealing process which indicates that NaCl played an important role in preventing the particles aggregation.[32]

Other physical methods used to produce nanosized ferrite powders include pulse laser ablation (for mixtures of iron oxides with sizes ranging from 30-100 nm)[35], radio-frequency plasma torch synthesis (for 20 nm and 26 nm Ni-substituted Fe_3O_4 and 18 nm $NiFe_2O_4$)[36], CO_2 laser pyrolysis (for 5 nm-sized γ-Fe_2O_3)[37] and γ-ray radiation (for 14 nm-sized Fe_3O_4).[38]

1.3.2. Preparation of Nanocrystalline Ferrites by Wet Chemical Methods

Although the physical methods are simple and versatile, enabling the preparation of a wide variety of ferrite nanopowders in large quantities and with a relatively low cost, their reliability is often questionable due to the contamination of the products (especially in the mechanical milling processes) and the limited control of the morphology of the resulting nanosized materials. The wet chemical synthetic routes have proven to be much more advantageous for the preparation of transition metal ferrites than the physical methods since they provide a better control over the size, size distribution, shape, and degree of agglomeration of the resulting nanocrystals. These characteristics, along with the chemical composition were found to influence significantly the magnetic properties of the ferrite nanoparticles and, therefore, their potential application in high-density magnetic storage media[39], magnetic resonance imaging[40,41], magnetic refrigeration[42], magneto-optical devices[43], and ferrofluids[44,45]. The use of nanophase ferrites in certain biological and biomedical areas requires them to possess not only uniform sizes (usually smaller than 20nm), shapes, and high values of the saturation magnetization, but also individual coatings with biocompatible molecules.[46-48] The solution-based chemical methods produce nanostructured transition metal ferrites with relatively good crystallinity even though they are, usually, low-temperature synthetic approaches. Moreover, a limited number of synthetic routes do afford large-scale preparations of high quality ferrite nanocrystals without a significant alteration of the morphology and properties of the resulting materials. However, the great disadvantages of the chemical methods lie in the fact that some of them use highly toxic reagents as metal precursors and necessitate a

rigorous control over the reaction parameters in order to obtain nanocrystalline ferrites with the desired morphology. In addition, most of the chemical methods use large amounts of capping ligands and surfactants rendering the resulting ferrite nanocrystals soluble in non-polar media. This imposes some restrictions on the use of the ferrite nanocrystals in certain biological systems which require solubility in aqueous media. Several solution-based approaches, both in aqueous and non-aqueous media, have been reported for the preparation of nanocrystalline ferrites particles; they include coprecipitation, microemulsion, sol-gel, hydrothermal/solvothermal and sonochemical methods.

1.3.2.1. Nucleation and Growth of the Nanoparticles

The common feature of the solution-based approaches is the precipitation of solid products from homogeneous solutions. Precipitation of solid particles is a dynamic process involving three stages: nucleation, growth, and coarsening/aggregation.[49-51] According to LaMer and Dinegar, who firstly described the theory behind the formation of monodispersed sulfur colloids from sodium thiosufate and hydrochloric acid, uniformly sized and shaped particles are obtained only when the nucleation and growth processes are completely separated. They proposed a diagram showing the variation of the solute concentration in time where three regions, corresponding to the prenucleation, nucleation and growth processes, can be easily identified (Figure 1.4)[52-54]. The pre-nucleation process (region I) is characterized by a relatively sharp increase of the solute (monomer) concentration as the chemical reaction progresses. At a critical value of the solute concentration ("nucleation concentration ") corresponding to a certain level of the

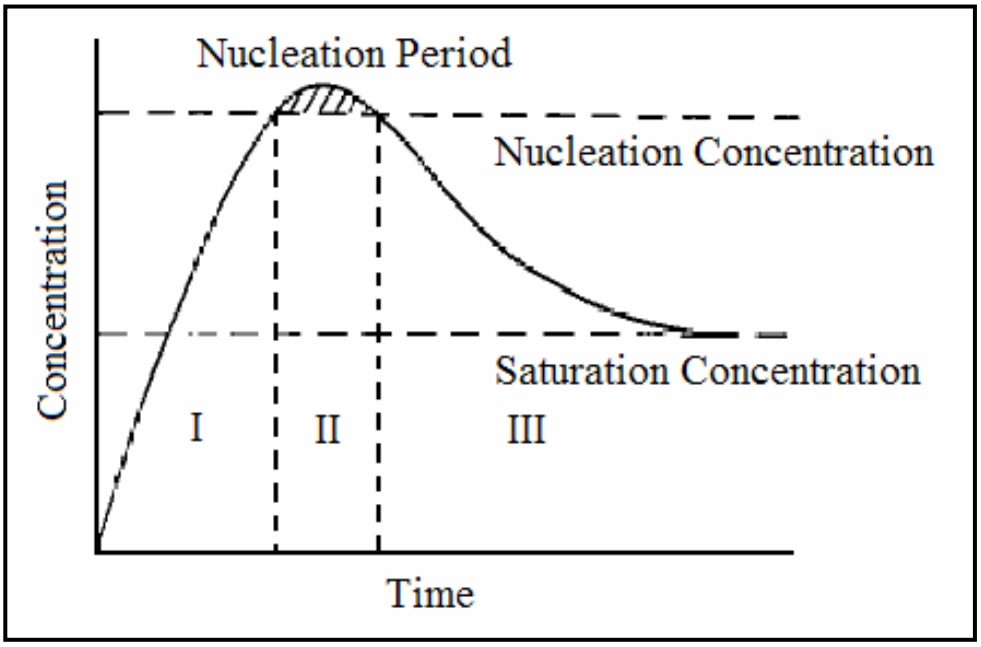

Figure 1.4. LaMer's diagram describing the formation mechanism for monodisperse colloidal particles [Ref. 52-54].

supersaturation, a transition from the homogeneous to heterogeneous state occurs as a result of the onset of the nucleation process. The solute concentration continues to increase with time during the "nucleation period" (region II), but is shortly followed by a rapid decrease due to an intensive colloid nucleation. Once the solute concentration approaches the "nucleation concentration" again, the nuclei are no longer produced in the system because the supersaturation level is now too low to further sustain the nucleation process. The existing nuclei enlarge by migration of the monomer species from the slightly supersaturated solution toward their surfaces, thereby causing a further decrease of the concentration (region III). The growth process occurs until the monomer concentration reaches the "saturation concentration". According to the LaMer diagram, the shape of the concentration–time curve suggests that the precipitation takes place through a fast nucleation process followed by a slower diffusional growth eventually leading to the formation of monodisperse colloidal particles.

The free energy associated with the formation of a nucleus by the aggregation of the solute species (monomers) in the supersaturated solution is given by the following equation: $\Delta G = -\left(\frac{V}{\Omega}\right) k_B T \ln \beta + S\gamma$, where V is the volume of the nucleus, S represents its surface area, Ω stands for the volume of a monomer molecule contained in the nucleus, β denotes the saturation ratio and γ is the normalized surface free energy. Particularly, for spherically-shaped nuclei with $V = \frac{4\pi}{3} r^3$ and $S = 4\pi r^2$, the free energy can be expressed as: $\Delta G(r) = -\left(\frac{4\pi r^3}{3\Omega}\right) k_B T \ln \beta + 4\pi r^2 \gamma$ and its sign is principally determined by the value of the saturation ratio (β). Thus, when β is less than 1.0 (the

solution is not enough supersaturated to induce the nucleation), the free energy, ΔG(r), takes positive values and the nucleation processes do not occur spontaneously. Conversely, when β is higher than 1.0, the free energy reaches a maximum, $\Delta G^*(r)$, corresponding to a certain value of the nuclear radius, $r^* = \frac{2\Omega\gamma}{k_B T \ln \beta}$, which is calculated by considering $\frac{d(\Delta G)}{dr} = 0$. Therefore, all the nuclei having a radius smaller than r^* are energetically unstable and shrink until they completely dissolve, whereas those with r higher than r^* continue to enlarge and become more stable since their energy decreases with increasing the size.[55, 56]

However, recent developments in the synthesis of nanostructured materials have demonstrated that the mechanistic pathway proposed by LaMer and Dinegar for sulfur colloids cannot explain itself the formation of solid particles in various other systems. For example, Cheon *et al*. observed that the precipitation of nearly monodisperse nanocrystalline γ-Fe_2O_3 by the thermal decomposition of iron pentacarbonyl precursor in the presence of different capping ligands occurs through an intermediate growth stage when variable sized particles are obtained.[57] The detailed investigation of the formation mechanism revealed that the γ-Fe_2O_3 nanocrystals capped with dodecylamine (DDA) undergo a size evolution upon heating the solution for different periods of time. Specifically, the powder isolated after 9 h of annealing in solution consisted of a mixture of 40 nm-sized hexagonal particles and 10 nm spherical particles, whereas the solid material collected after 16h contained 50 nm hexagonally-shaped particles as the main fraction with a very small amount of tiny (~ 3 nm) nanocrystals. These experimental observations suggest that nucleation and growth of the particles is followed by a

coarsening process in which the larger particles continue to grow until they attain the final morphology, whereas most of the smaller particles gradually decrease their sizes and eventually dissolve. Such a solution-mediated mass transport from the small to the large particles with the improvement of the size distribution is called Ostwald ripening.[50, 58-60]. As it can be deduced from the Gibbs-Thompson equation, the driving force of the Ostwald ripening process is the variation of the solubility (equilibrium concentration) of the particles with their size: $c_r = c_{r=\infty} \exp\left(\frac{2 \cdot \gamma \cdot \Omega}{k_B \cdot T} \cdot \frac{1}{r}\right)$, where c_r represents the solubility of a grain with the radius r and $c_{r=\infty}$ stands for the solubility of a large-sized solid material (the bulk solubility). [53, 55, 58] Thus, for a system containing nanoparticles with a wide size distribution, the equilibrium concentration of the monomers (solutes) at the solid-liquid interfaces is not constant but instead it fluctuates depending on the particle size. For example, according to the Gibbs-Thomson equation, the monomer (solute) concentration in the nearby solution of the large nanoparticles is smaller than that in the bulk solution. This determines the formation of a concentration gradient at the interface between each nanoparticle and the bulk solution which will induce the particle growth via migration of the monomers (solutes) from the surrounding solution to the nanocrystal surface. Conversely, for the small nanoparticles, the monomer (solute) concentration at the particle-solution boundary is higher compared to that in the bulk solution. This will determine the diffusion of the solute species from the nanocrystal surface to the solution, thereby leading to the gradual dissolution of the small nanoparticles during the coarsening process.[60, 61]

The Ostwald ripening process has been observed to take place in either aqueous or non-aqueous media and is influenced by several parameters including the reaction

time[57], the pH[62], the ionic strength[62] of the solution and the nature of solvent and the capping ligand[57, 63]. For example, Vayssières *et al.* showed that during the preparation and aging of aqueous suspensions of Fe_3O_4 nanoparticles, the increase of the pH and the ionic strength of the solution will significantly inhibit the Ostwald ripening process. This is due to the fact that at high values of the pH and the ionic strength of the solution, a large number of HO^- ions and cations provided by the solvent and the electrolyte are adsorbed on the surface of the nanoparticles, thereby decreasing their surface free energy (γ) and stabilizing them against a further coarsening process during the aging period. [62]

Recently, Sastry and coworkers reported a novel synthetic approach for the preparation of the nanocrystalline iron oxides in slightly acidic solutions containing $K_4Fe(CN)_6$ and $K_3Fe(CN)$ as precursors. The bacterium-mediated reaction results in the formation of polydisperse spherical-shaped particles with sizes ranging from 10 to 40 nm. Longer reaction times cause clustering and coalescence of the spheroidal particles initially produced in the system into larger cubically-shaped crystals with sizes varying between 50 and 150 nm.[64]

Such a growth mechanism by which small-sized particles called "primary particles" cluster into intermediate shapeless aggregates to produce well-defined, nearly monodisperse "secondary particles" is referred as aggregation (coalescence).[65] In many cases, formation of nanostructured materials involves a single aggregation step by which the primary particles resulted from the nucleation and diffusional growth processes tend to minimize their surface free energy by clustering and coalescence into larger, more stable structural entities.[66-68] However, as Zheng *et al.* have recently demonstrated for nanocrystalline α-Fe_2O_3 prepared solvothermally, the growth mechanism can occur

through more than one aggregation step. A close examination of the TEM micrographs corresponding to the iron oxide samples collected at different reaction times revealed that the small 5-8 nm-sized crystals cluster together to give larger particles with sizes ranging between 15 and 30 nm. The resulting nanoparticles act as building blocks for the subsequent growth of the 40-50 nm irregularly-shaped aggregates. Each of these single crystalline entities undergoes a coarsening (Ostwald ripening) process leading to the formation of highly faceted α-Fe_2O_3 particles with a relatively narrow size distribution.[69]

The secondary particles resulting by the clustering and coalescence of two or more primary nanocrystallites can be either monocrystalline or polycrystalline in nature, depending on the arrangement of the smaller units within each larger structural entity.[67] Polycrystalline secondary structures have been obtained when the nanosized primary particles aggregate in a random manner.[70] The random clustering of the nanocrystalline units can also yield monocrystalline secondary particles when the aggregation is followed by an internal recrystallization process.[66] However, monocrystalline particles are commonly obtained by the oriented attachment of the primary nanocrystallites which necessitates a continuity of the crystal lattices of the neighboring particles through each shared interface.[67-69, 71, 72] In such a case, a perfect alignment of the lattice fringes over the whole assembly can be easily identified by examining the HRTEM micrographs. The formation of secondary particles through the oriented attachment mechanism is often accompanied by the formation of various packing defects including dislocations, twins, phase boundaries and stacking faults.[73-75] In some cases, both the aggregation and the Ostwald ripening processes contribute to the formation of nanocrystalline ferrite particles.[63,69] Barker and coworkers conducted a comparative study of the growth

processes based on the strength of the interaction between different stabilizing agents and the surface of the Fe_3O_4 nanoparticles prepared by the thermal decomposition of iron (III) acetylacetonate in organic media. For this reason, the authors performed two separated experiments using trioctylamine, which acts both as a solvent and a stabilizing agent, and a mixture of trioctylamine (solvent) and heptanoic acid (capping ligand), respectively. According to them, when the experiment is carried out in trioctylamine, the small particles initially formed in the system aggregate into larger shapeless assemblies with polycrystalline structure and broad size distribution. The clustering and coalescence stage is followed by an Ostwald ripening process when the resulting intermediate aggregates undergo internal recrystallization leading to the formation of monocrystalline, highly faceted particles. However, the growth mechanism changes significantly when the synthesis is performed in the presence of heptanoic acid. In this case, the growth process which occurs by Ostwald ripening is much slower and yields smaller single crystalline particles with a narrow size distribution. These two mechanistic pathways observed in the formation of the Fe_3O_4 nanoparticles were ascribed to the different binding properties of the trioctylamine and heptanoic acid, respectively.

1.3.2.2. Synthesis of Nanocrystalline Ferrites in Aqueous Solutions

1.3.2.2.1. The Coprecipitation Method

Coprecipitation of nanocrystalline ferrites from aqueous homogeneous solutions is one of the most popular liquid phase synthetic approaches due to its simplicity, low cost and versatility. Transition metal ferrite nanoparticles with a wide variety of

compositions ranging from ternary metal oxides[48, 76-78] (AFe_2O_4, A^{2+}=Mn^{2+}, Fe^{2+}, Co^{2+}, Cu^{2+}, Zn^{2+}) to mixed metal oxides containing two[79] ($A_xB_{1-x}Fe_2O_4$, A^{2+}=Co^{2+}, B^{2+}=Ni^{2+}) or three[80] ($A_xB_yC_{1-x--y}Fe_2O_4$, A^{2+}=Ni^{2+}, B^{2+}=Cu^{2+}, C^{2+}=Zn^{2+}) different divalent metal ions have been prepared by using the coprecipitation technique. In a typical coprecipitation process, aqueous solutions containing divalent metal precursors, such as acetates, chlorides, nitrates or sulphates, and an iron (III) salt are treated with a precipitating agent.[76, 80, 81, 83, 84] Alternatively, the synthesis can be performed by replacing the ferric precursor with a ferrous salt, but in this case the partial oxidation of the iron (II) compound is required.[80, 82] In addition to alkaline hydroxides (NaOH, KOH)[77, 81] and ammonia solutions[85, 86], another commonly used precipitant is urea.[84, 85] This organic compound undergoes a hydrolysis reaction[87] when heated at temperatures higher than 60ºC with the formation of hydroxide ions (HO^-):

$$CO(NH_2)_2 + 3H_2O \rightarrow 2NH_4^+ + CO_2 + 2HO^-$$

The nature of the precipitating agent was found to influence significantly the morphology of the ferrite nanopowders synthesized by the coprecipitation method. For example, Ryu and coworkers reported the preparation of nanophase $Co_{1-x}Ni_xFe_2O_4$ ($0<x<1$) and compared the morphology of the particles obtained in the presence of two different precipitating agents, that is, NaOH and NH_4OH, respectively.[79] When the precipitation is performed with NaOH the resulting particles possess a relatively good crystallinity, their sizes vary between 15 and 25 nm, depending on the Co/Ni ratio and have a needle-like aspect, except for the first term of the series (x=0), where the particles are spherical. This is not the case of the nanopowders precipitated in the presence of NH_4OH, when the particles are found to be less crystalline and their sizes range from 2 to 10 nm.

However, regardless of the morphology of the as-prepared nanopowders, the nanostructured ferrite materials resulting from their heat treatment at 600^{o}C consist of agglomerated particles with an average size of 30 nm. The morphological changes of the as-prepared nanopowders during the annealing process were found to depend on their initial composition. Thus, while in the alkaline medium the transition metal ions precipitate as hydroxides, in the presence of an ammonia solution the coprecipitation occurs with the formation of transition metal complexes incorporating the NH_4^+ ions.

The temperature is one of the most important parameters in the coprecipitation process. When the metal ions are precipitated at room temperature, amorphous intermediate compounds such as hydroxides or oxyhydroxides separate from the reaction solution. In such a case, a subsequent heat treatment of the hydroxo-intermediates is required in order to obtain the corresponding nanocrystalline ferrite materials.[80, 86, 88] Chen *et al.* prepared nanosized $MnFe_2O_4$ particles by mixing stoichiometric amounts of Mn(II) and Fe(III) chlorides with NaOH at room temperature followed by the digestion of the resulting precipitate at 100°C. In addition to promoting the dehydration of the metal hydroxide intermediates and the crystallization of the nanophase $MnFe_2O_4$, the thermal treatment was found to strongly influence the size of the ferrite nanoparticles.[78]

However, if the coprecipitation reaction takes place in boiling solutions containing the metal precursors and the precipitating agent, the hydroxo-intermediates formed at elevated temperature are immediately converted into nanocrystalline ferrites.[76] For instance, Sousa and coworkers prepared a series of nanosized transition metal ferrites (MFe_2O_4, M^{2+}= Ni^{2+}, Cu^{2+}, Zn^{2+}) by precipitating the metal ions in alkaline media at 100°C. As demonstrated by the X-ray diffraction measurements, the isolated solid

products were found to be single-phase mixed metal oxides with spinel structure and good crystallinity.[77]

Unlike the other transition metal ferrites, Fe_3O_4 can be obtained as an oxide even at room temperature.[43, 83, 85] Kang *et al*. reported the synthesis of 8.5 nm-sized Fe_3O_4 particles by room temperature coprecipitation of a 1:2 molar mixture of Fe(II) and Fe(III) precursors with a solution of NaOH. The resulting black solid was treated with a diluted solution of HCl and then dispersed in water to form an aqueous colloid. The positive charges built up at the surface of the Fe_3O_4 nanocrystals upon acidification induce electrostatic repulsions between neighboring particles thereby stabilizing the colloidal dispersion against aggregation. The TEM investigation of the aqueous colloid revealed that the Fe_3O_4 nanoparticles are uniformly sized and shaped and they assemble into monolayers.[43]

Kim *et al.* showed that by performing the coprecipitation reaction at different temperatures, variable-sized Fe_3O_4 nanoparticles can be obtained. 6nm particles were synthesized by adding a stoichiometric mixture of Fe(II) and Fe(III) salts to a solution of NaOH at room temperature. The same reaction carried out at 80°C yielded Fe_3O_4 particles with an average size of 12 nm.[89] In the preparation of the Fe_3O_4 nanopowders by coprecipitation instead of mixtures of Fe(II) and Fe(III) salts in molar ratios of 1:1[48] or 1:2[83], other Fe(II) compounds (chlorides or sulphates) have also been used[81, 90]. In such cases, the partial oxidation of the ferrous ions is necessary in order to obtain Fe_3O_4 nanoparticles. For example, Tada and coworkers synthesized nanocrystalline Fe_3O_4 powders containing traces of γ-Fe_2O_3 by oxidation of $Fe(OH)_2$ in the presence of H_2O_2.

Prior to the oxidation, the iron (II) hydroxide intermediate was obtained by the precipitation of the iron(II) salt with a solution of KOH under ambient conditions.[81]

1.3.2.2.2. The Sol-Gel Method

Nanocrystalline ferrites have also been synthesized by the sol-gel method[91-94], a synthetic route widely used for the preparation of various types of ceramic materials (magnetic[95, 96], ferroelectric[97, 98] and thermomechanic[99]) as well as glasses[100] and catalysts.[101, 102] The sol-gel technique is a multi-step synthetic route in which a precursor dissolved in a suitable solvent is converted into the corresponding crystalline oxide through a succession of chemical and physical processes.[103] The precursor materials generally used in the sol-gel approach are the metal/metalloid alkoxides and the metal salts. For example, various silicon alkoxide precursors, such as tetraalkoxysilanes ($Si(OR)_4$, R=CH_3, C_2H_5, n-C_3H_7, n-C_4H_9, $OCH_2CH_2OCH_3$), organoalkoxysilanes ($R'_xSi(OR)_{4-x}$, x=1-3 and R' is an organic radical unreactive towards hydrolysis) and alkoxysiloxanes (oligomeric compounds consisting of 1 to 8 silicon atoms) have been employed in the sol-gel preparation of silicon-based compounds including silica (SiO_2), silicones, and silicate gels, respectively.[104] Likewise, binary metal oxides such as M_2O_z (M= Ti, Zr, Hf, Nb, Ta, Ce, Th) have been synthesized from the corresponding metal alkoxides ($M(OR)_z$)[102, 105], whereas the more complex cubic and hexagonal ferrites (MFe_2O_4 and $MFe_{12}O_{19}$, M is a divalent metal ion) are usually prepared by using metal salts (nitrates, chlorides and acetates) as precursor materials.[96, 106, 107, 108] Regardless of the nature of the oxide product, two types of chemical reactions are usually involved in

the sol-gel technique: the hydrolysis of the metal/metalloid precursor and the condensation of the resulting intermediates.[103, 105] Hydrolysis and condensation are complex reactions occurring either concurrently or separately in the course of the sol-gel process and being closely dependent on the nature of the precursor. As an example, when metal salts are used as precursors, the hydrolysis reaction involves solvated cations generated in aqueous solutions by the electron transfer from the water molecules to the metal ions:[104, 105]

$$M^{z+} + NH_2O \longrightarrow [\, M(H_2O)_N]^{z+}$$

In such a case, the hydrolysis reaction occurs by the elimination of the protons from the coordination sphere of the solvated cation:

$$[M(H_2O)_N]^{z+} \overset{-H^+}{\rightleftharpoons} [M(OH)(H_2O)_{N-1}]^{(z-1)+} \overset{-H^+}{\rightleftharpoons} \text{.....} [M(OH)_N]^{(N-z)-} \overset{-H^+}{\rightleftharpoons}$$

$$[MO(OH)_{N-1}]^{(N-z-1)-} \overset{-H^+}{\rightleftharpoons} \text{.....} [MO_{N-1}(OH)]^{(2N-z-1)-} \overset{-H^+}{\rightleftharpoons} [MO_N]^{(2N-z)-}$$

According to Livage *et al.*, several types of intermediates can be generated in the course of the hydrolysis process: aquo ($[M(H_2O)_N]^{z+}$, where N stands for the coordination number), hydroxo-aquo ($[M(OH)(H_2O)_{N-1}]^{(z-1)+}$), hydroxo $(M(OH)_N]^{(N-z)-}$, oxy-hydroxo ($[MO(OH)_{N-1}]^{(N-z-1)-}$) and oxy ($[MO_N]^{(2N-z)-}$)species, respectively.[104, 105] Once formed in the aqueous solution, these intermediates undergo subsequent condensation reactions eventually leading to the formation of metal oxide products. However, the mechanistic pathways through which the intermediates are transformed into the final product are substantially different, being primarily determined by the nature of the groups coordinated to the metal ions. Thus, when hydroxo-aquo species are involved in the condensation process, hydroxo bridges are created between the M^{z+} cations. Such a

condensation reaction is called olation and proceeds through a nucleophilic substitution (S_N) mechanism with elimination of a water molecule:[104, 105]

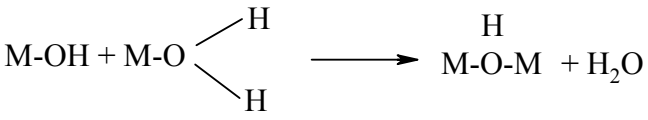

Conversely, when the condensation reaction takes place in the presence of oxo-hydroxo intermediates, oxo bridges are created between the M^{z+} cations. Such a reaction refers to as oxolation and can proceed either through a nucleophilic addition (A_N) or through a nucleophilic substitution (S_N), depending on the saturation of the coordination sphere of the M^{z+} cations. For the M^{z+} cations with unsaturated coordination spheres, the oxolation reaction between the corresponding oxo-hydroxo intermediates takes place through a nucleophilic addition mechanism:[104, 105]

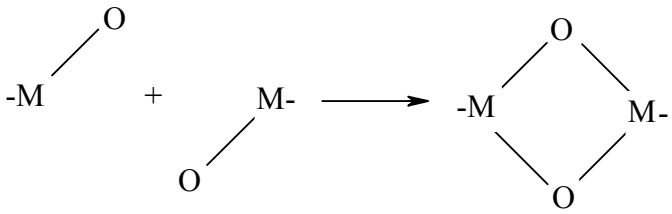

If the coordination sphere of the M^{z+} cations is saturated, the oxolation reaction takes place through a nucleophilic substitution mechanism. In such a case, the oxo-hydroxo species undergo a condensation reaction which is usually described as a two-step process consisting of a nucleophilic addition and a β-elimination. The hydroxo-bridged intermediate formed by the nucleophilic addition loses a water molecule to give a compound in which the M^{z+} cations are linked by an oxo bridge:[104, 105]

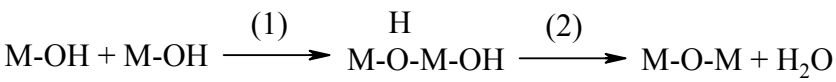

In general, the sol-gel processing involves several successive stages: (a) the formation of a sol which represents a colloidal suspension containing small particles with a diameter less than 1000 nm dispersed in a continuous liquid medium; (b) the gelation of the sol to give a three-dimensional M-O-M/M-OH-M network whose pores are filled with solvent molecules (wet gel); (c) the aging of the resulting wet gel, process known as syneresis; (d) the elimination of the solvent from the gel pores (drying) and (e) the calcination of the resulting porous gels with the formation of metal oxide ceramic materials (densification).[103, 104]

Kim *et al.* have extensively used the sol-gel method to prepare various nanocrystalline spinel-type oxides including $Co_{1-x}Zn_xFe_2O_4$ ($0<x<1$), $Ni_{0.65}Zn_{0.35}Cu_{0.2}Fe_{1.8}O_4$, $Cu_{0.9}Mn_{0.1}Fe_2O_4$ and $CoFe_{1.9}Re_{0.1}O_4$ (RE=Y, La), respectively. Transition metal ferrite nanopowders were typically obtained by calcining the amorphous gels resulting from the hydrolysis of metal salts (acetates, nitrates) dissolved in different solvent mixtures. It is worth noting that, in all cases, the temperature effect on the magnetic properties of the nanocrystalline ferrites shows a similar trend regardless of their chemical composition. Specifically, the saturation magnetization (M_s) of the ferrite powders increases with increasing the calcination temperature, whereas the coercivity (H_c) increases to reach a maximum and then drops abruptly. Such a variation of the magnetic properties of the nanophase ferrites is dependent on the particle size which was found to increase with the calcination temperature.[91-94]

Since the magnetic properties of the spinel-type metal oxides are very sensitive to both the M^{2+}/M^{3+} molar ratio and the cation distribution within the spinel lattice, a strict control over the chemical composition of the ferrite products is highly desirable in the

sol-gel process. To this end, the bimetallic sources have proven to be more suitable for the preparation of single phase ferrite nanopowders than the mixtures of single-metal precursors. Veith and coworkers have synthesized nanophase $ZnFe_2O_4$ by calcining the solid intermediates resulting from the hydrolysis of mixed metal alkoxides $Zn[Fe(OR)_4]_2$ (R= $-C(CH_3)_3$, $-CH(CH_3)_2$) dissolved in both polar and non-polar solvents.[109] While the mixed metal precursors ($Zn[Fe(OR)_4]_2$) were prepared from the reaction of alkoxo sodium ferrate ($NaFe(OR)_4$) and zinc chloride ($ZnCl_2$) under inert atmosphere, the ferrate compound was pre-synthesized by treating sodium alkoxide (NaOR) with iron (III) alkoxide ($Fe(OR)_3$). Alternatively, the alkoxo sodium ferrate could be obtained by reacting sodium alkoxide (NaOR) with iron(III) chloride with the elimination of sodium chloride.

The bimetallic alkoxide $Zn[Fe(OR)_4]_2$ is then hydrolyzed with a mixture of water and 2-propanol and the resulting xerogel is thermally decomposed to a nanocrystalline $ZnFe_2O_4$ product. Interestingly, the phase purity of the prepared ferrite nanopowders was found to be very sensitive to the nature of the solvent used in the hydrolysis step. Unlike the polar solvents, which lead to single phase $ZnFe_2O_4$ nanoparticles even when the xerogel is heat treated at relatively low temperatures (200^oC), the hydrolysis reactions performed in non-polar solvents yield nanocrystalline product which is slightly impurified by zinc and iron oxides, respectively. In such a case, the detrimental effect of the polarity of the solvent can be eliminated only upon calcination of the xerogel at high temperatures (800^oC), when the secondary phases disappear with formation of a single phase ferrite nanopowders.

1.3.2.2.3. The Hydrothermal/Solvothermal Method

Aqueous solution-based synthetic strategies have been extensively used for the preparation of nanophase ferrites by virtue of their simplicity, low cost and versatility. However, due to the low boiling point of water (b.p.=100°C at 1 atm) the chemical reactions in aqueous medium usually take place at low temperatures, thus leading to nanostructured metal oxides with a relatively poor crystallinity. Due to the mild reaction conditions, a subsequent annealing step is often required to convert the as-prepared powders into highly crystalline nanophase ferrites. Although the grain size and the crystallinity of the as-prepared nanopowders can be significantly improved during the post-synthesis heat treatment, in most of the cases the resulting particles have a wide size distribution, irregular shapes and a high degree of agglomeration.

An effective approach to obtain highly crystalline ferrites from aqueous solutions, eliminating the annealing step, consists of heating the reaction mixture in a sealed container at moderate temperatures. In such conditions, a high pressure is built up inside the bomb-type reactor, thereby increasing the temperature of the solution high enough to promote the chemical reactions between the precursors and to produce ferrite powders with good crystallinity. As the pressure inside the reaction vessel increases, significant changes on the physical properties of the solvent are observed over a wide temperature interval. Thus, the polarity and density of the water decrease, whereas its temperature increases rapidly to reach values much higher than the boiling point. Additionally, its solvent properties are greatly enhanced, thereby enabling the complete dissolution of various compounds, both organic and inorganic, which otherwise have a sparse solubility

in aqueous media. Finally, when the temperature and pressure attain the so-called "critical values" (T_C=374°C, P_C=218 atm), the dissimilarities between the gaseous and liquid phases disappear completely and a new phase known as supercritical water is formed. In the supercritical state, water combines the individual characteristics of the liquid and gas phases making it very attractive as reaction medium for various chemical reactions.[110] However, such a behavior is not restricted only to water; other many non-aqueous solvents can serve as reaction media under similar conditions. Thus, when the chemical reactions take place in aqueous solutions the process is known as hydrothermal, whereas for non-aqueous solvents the technique is called solvothermal.[111] Under such extreme conditions, chemical reactions can occur in both sub-critical and super-critical regime, thereby resulting into highly crystalline single-phase products which do not necessitate post-synthesis annealings. However, although the hydrothermal/solvothermal process is a one-pot, highly efficient "green-chemistry" preparative route for various ferrite materials, it allows only for a limited control of the nucleation and growth processes usually yielding particles with irregular shapes, relatively large sizes and a wide size distribution.[112]

Yu and coworkers noted that hydrothermal heating at 180°C of an ammoniacal $FeCl_2$ solution containing metallic Zn leads to the formation of octahedrally-shaped $ZnFe_2O_4$ nanoparticles with an average size of 300 nm. While the purity of the ferrite material is controlled by the reaction time and temperature, its crystallinity was found to be significantly enhanced by increasing the concentration of ammonia in the reaction solution.[113] The reaction time and temperature as well as the dielectric constant of the reaction medium were also found to exert a significant effect on both the particle size and

the crystallinity of the hydrothermally-prepared nanophase ferrites. For example, the particle size of the nanocrystalline $NiFe_2O_4$ synthesized from an alkaline solution containing the corresponding transition metal salts could be varied from 10 nm to 120 nm by simply raising the reaction temperature from 60°C to 120°C. Increasing the reaction time from 3h to 6h increased the dimensions of the ferrite particles from 10 nm to 70 nm. The same size variation was observed when decreasing the dielectric constant of the reaction medium by increasing the *i*-PrOH/H_2O volume ratio from 0.05 to 0.10.[114] Likewise, in the case of solvothermal reactions, both the crystallinity and morphology of the ferrite nanoparticles is significantly affected by the variation of several parameters including the reaction time, temperature, concentration of the metal precursor and the nature of the solvent and the capping agent.[115-117] Hou and coworkers prepared nearly spherical Fe_3O_4 nanocrystals by the partial reduction of iron (III) acetylacetonate with hydrazine in the presence of different organic molecules as stabilizers.[116] Prior to the solvothermal reaction the iron source was dissolved into a mixture containing ethylene glycol (EG) and polyvinyl pyrrolidone (PVP), followed by the slow addition of the reducing agent. As revealed by the TEM investigation, the size of the nanoparticles decreases when a second stabilizer, is added to the reaction solution. Thus, while the size of the Fe_3O_4 nanoparticles prepared in neat PVP was found to be close to 11 nm, similar experiments performed in mixtures of PVP with tri-n-octylphosphine oxide (TOPO) or hexadecylamine (HAD) yielded 8 nm Fe_3O_4 nanoparticles.

1.3.2.2.4. The Microemulsion Method

The microemulsion technique has proven to be a viable synthetic route for the preparation of a wide range of nanostructured inorganic materials including metals (Pt[118], Ag[119], Cu[120]), alloys (Pt/Pd[121, 122], Au/Pt[123]), halides (AgCl[124, 125], AgBr[125], $KMnF_3$[126, 127]), sulfides (PbS[128], CdS[129], ZnS[130]) and oxides (SnO_2[131], TiO_2[132]). In particular, this synthetic approach has been extensively used for the synthesis of spinel-type ferrites containing one (MFe_2O_4, where M^{2+}=Mn^{2+}, Fe^{2+}, Co^{2+}, Ni^{2+})[133-137] or more ($M'_XM_{1-X}Fe_2O_4$, where M'^{2+}=Mn^{2+}, Ni^{2+} and M^{2+}=Zn^{2+})[138-141] divalent metal cations.

Microemulsions are colloidal systems in which one of the two mutually insoluble liquids is dispersed as fine droplets (with a size typically less than 100nm) in a second continuous liquid phase.[142] The two liquids are commonly referred to as the "aqueous phase", that is an aqueous solution containing transition metal salts ($[M^{2+}]/Fe^{3+}]$=1:2, $[M^{2+}]/[Fe^{2+}]$=1:2 and $[M'^{2+}]/[M^{2+}]/[Fe^{2+}]$=1:1:4)[133, 134, 143, 144] or a precipitating agent (tetramethyl ammonium hydroxide-$(CH_3)_4NOH$, ammonium hydroxide-NH_4OH, sodium hydroxide-NaOH and methyl amine-CH_3NH_3OH)[133-135, 143, 144], and the "oil phase", represented by an organic solvent immiscible with water. Among the most frequently used non-polar organic solvents are heptane[145], isooctane[133, 137, 138, 140, 146], toluene[134, 143], (o-, m-, p-) xylenes[147]. In addition to the hydrocarbons, other organic substances, such as fatty alcohols (1-hexanol)[139, 141, 144, 148] and halogenated compounds (1,1,1-trichloroethane)[142], as well as supercritical fluids (CO_2)[142] have been employed in the microemulsion technique. However, because of the high interfacial tension between the two mutually insoluble liquids, such heterogeneous systems are labile with respect to

separation and surface active agents (surfactants) are often required to stabilize the microemulsion. Surfactants are amphiphilic organic molecules containing a polar (hydrophilic) group attached to a non-polar hydrocarbon (lipophilic) chain.[150] Depending on the charge of the hydrophilic group, the surfactants can be classified into three main categories: ionic (anionic or cationic), non-ionic (neutral), and amphoteric (possess both positively and negatively charged moieties), respectively. The hydrophobic part of the surfactant molecule usually consists of one or more aliphatic chains, aromatic rings or combinations of them where the number of carbon atoms typically varies between 10 and 20.[142, 151] When a certain amount of surfactant is added to a mixture of two immiscible liquids, its molecules tend to self-organize at the liquid-liquid interfaces with the formation of spherically-shaped aggregates called micelles. The minimum surfactant concentration at which the micelles form in the heterogeneous system is referred to as "critical micellar concentration".[150] Micelles are categorized in two types, that is "normal" and "reverse", depending on the nature of the liquid phase contained in their cores. For example, in the normal micellar solutions (oil-in-water) the surfactant-stabilized nanodroplets of a non-polar liquid (oil phase) are dispersed in a continuous polar medium (aqueous phase). In this case, the surfactant molecules will have the hydrophilic functional groups (heads) oriented to the continuous aqueous phase, whereas the hydrophobic chains (tails) will point to the non-polar liquid confined in the micellar core.[142]

In general, micelles experience a random movement in solution leading to collisions which can be followed by the formation of either pairing micelles or short time-living dimers. Since these mutual interactions facilitate the exchange of the content

of their cores, thus promoting chemical reactions, micelles are suitable as nanoreactors for the preparation of various nanocrystalline materials, including metals or oxides. For example, nanocrystalline ferrites can be synthesized in reverse micelles by precipitating a micellar solution of transition metal ions with a base. The base can be either dispersed in a water-in-oil microemulsion or can be a bulk solution. In these conditions the precipitation occurs either by diffusion of the molecules of the reagents through the surfactant bilayer of the pairing micelles or by direct mixing of their contents when the surfactant molecules at the surface contact of the interacting nanodroplets are temporarily eliminated during their collision and fussion. Once the reagents are mixed, the nucleation and growth of the nanoparticles occurs within the confined space of the micelles yielding nearly spherical nanocrystals with a size comparable to the diameter of the surfactant-stabilized water pools.[142] In many cases, the chemical reactions are performed at room temperature and the isolated solid products consist of mixtures of metal hydroxides/oxyhydroxides with a poor crystallinity. In these conditions, a post-synthesis annealing is often necessary to convert them into crystalline mixed metal oxides. However, this would be detrimental for the ferrite nanopowders since it results not only in complex structural changes like the cation redistribution, but also in morphological transformations such as aggregation of the nanoparticles[134, 138, 146, 149] or increase in the grain size[148]. Such side effects can be decreased upon elimination of the post-synthesis heat treatment. This is possible if the microemulsion-based syntheses are carried out at moderate temperatures (45-95^{o} C) when the as-prepared ferrites nanopowders possess a relatively good crystallinity and a supplementary heat treatment is not longer necessary.[139, 141]

Pileni and coworkers applied the oil-in-water microemulsion technique to the preparation of various nanocrystalline transition metal ferrites. In these syntheses, the nanophase ferrites were precipitated by introducing a controlled amount of methylamine into a normal micellar solution containing transition metal dodecyl sulfates. Interestingly, these metal compounds act both as metal sources for the synthesis of nanostructured ferrites and as surfactants for the formation of the normal micellar systems. The metal dodecyl sulfates were prepared prior to the synthesis by reacting divalent metal salts, typically chlorides and acetates, with sodium dodecyl sulfate (NaDS). The experiments were usually carried out in air in order to promote the oxidation of the Fe^{2+} ions to Fe^{3+} ions necessary in the synthesis of the ferrite materials.[135, 136] The investigation of the formation mechanism of the nanophase magnetite revealed that two parameters influence the size of the resulting nanoparticles, i.e., the reaction temperature and the concentration of the iron (II) dodecyl sulfate ($Fe(DS)_2$). Transmission electron microscope (TEM) measurements showed that by changing the iron(II) dodecyl sulfate concentration from 2.5×10^{-3}M to 10^{-2} M the particle size increased from 3.7 nm to 7 nm when the reaction was performed at room temperature. Likewise, by varying the reaction temperature from 25ºC to 80ºC and keeping constant the concentration of the iron (II) dodecyl sulfate at 2.5×10^{-3}M, the dimensions of the particles increased from 3.7 nm to 6.6 nm. The largest magnetite particles (11.6 nm) were obtained for the highest values of both the $Fe(DS)_2$ concentration (10^{-2} M) and the reaction temperature (80ºC). The authors assumed that the variation of the nanoparticle size is dictated by the fraction of the Fe^{2+} ions being oxidized to the Fe^{3+} ions rather than the modification of the morphology of the normal micelles. Their hyphothesis was supported by a series of small angle X-ray spectroscopy

(SAXS) measurements which indicated that neither the surfactant concentration nor the reaction temperature affected the dimensions of the normal micelles. When either of these parameters is increased, a larger amount of oxygen is dissolved in the normal micellar solution which induces the oxidation of a higher proportion of the Fe^{2+} ions and, eventually, the enlargement of the magnetite particles.[135]

Vestal *et al.* performed a comparative study on the properties of the nanocrystalline $CoCrFeO_4$ synthesized by using both the oil-in-water and water-in-oil microemulsion techniques.[149] Although the resulting ferrite particles were quite different in size, their shape, relative size distributions as well as the trends in the variations of the magnetic properties showed similarities regardless of the nature of the micellar solution used in the synthesis. Thus, while $CoCrFeO_4$ particles synthesized from normal micellar solutions possess a size which ranges from 8 nm to 16 nm depending on the reaction temperature, the average diameters of the nanocrystals obtained by the reverse micelle technique can be varied between 6 nm and 11 nm upon adjustment of the water/oil volume ratio.

The large-scale preparation of the nanophase ferrites using the microemulsion technique has long been a challenge since this synthetic approach usually produces small amounts of solid materials, typically on the order of several tens of milligrams. According to two recent reports, large quantities of nanocrystalline ferrites could be produced in a single experiment by performing the precipitation reactions in a reverse micelle system.[146, 147] Lee and coworkers reported the multi-gram preparation of variable-sized Fe_3O_4 nanocrystals by precipitating stoichiometric mixtures of iron salts with hydrazine in a water-sodium dodecylbenzenesulfonate-xylene micellar system. Refluxing

the reaction solution for several hours under argon atmosphere resulted in the formation of pure nanometer-sized Fe_3O_4 particles with a high crystallinity. Interestingly, the prolonged refluxing at temperatures around 100ºC did not disrupt the micellar structure of the solution and allowed the preparation of non-aggregated Fe_3O_4 nanocrystals with spheroidal shape and relatively tight size distribution. The particle dimensions could be varied between 2 nm and 10 nm by adjusting the relative amounts of the divalent and trivalent iron salts and the polar solvent/surfactant molar ratio. This large–scale preparation technique was adapted to the synthesis of other nanocrystalline transition metal ferrites, such as $MnFe_2O_4$, $CoFe_2O_4$, $NiFe_2O_4$ and $ZnFe_2O_4$. The obtained particles have sizes that range from 4 nm to 6.5 nm depending on the nature of the divalent metal cation. Compared to Fe_3O_4, the mixed metal ferrite nanocrystals are characterized by more irregular shapes and broader size distributions. The great advantage of the synthetic procedure developed by Lee and coworkers lies in the use of relatively small quantities of organic solvents, similar to those employed in the conventional water-in-oil microemulsion method, whereas the amounts of the metal precursors are up to 10 times larger than those used in a regular experiment .[147]

1. 3. 2. 3. Synthesis of Nanocrystalline Ferrites in Non-Aqueous Medium

In addition to the precipitation in aqueous solutions, nanocrystalline mixed metal oxides can be alternatively synthesized by chemical reactions performed in non-aqueous media. Although they are not always environmentally friendly, non-aqueous approaches present some major advantages over the conventional aqueous solution methods.

Examples include a strict control over the size of the nanoparticles, a high crystallinity, as well as a tunable solubility in polar and non-polar solvents. Due to the high boiling point of the organic solvents, chemical reactions in non-aqueous solutions take place at much more elevated temperatures than those in aqueous media, usually leading to the formation of highly crystalline products without the need of post-synthesis heat treatment. In addition, the reaction rates can be controlled much easier in non-aqueous media, thus allowing for a complete separation of the nucleation and growth processes and yielding nearly monodisperse nanoparticles with a controllable size, shape and agglomeration degree. One of the characteristics common to the organic solution techniques is the use of capping agents. In general, capping ligands are long chain organic molecules that passivate the nanoparticles'surface, thus inhibiting their growth and stabilizing them against clustering and aggregation. Depending on the nature of their free groups, the capping ligands facilitate the dispersion of the passivated nanocrystals into various solvents, either polar or non-polar, with the formation of stable colloidal suspensions. The non-aqueous techniques involved in the preparation of the nanocrystalline ferrites usually fall within two categories, *i. e.* the hydrolysis of the transition metal ions in polyol medium (the polyol method) and the thermal decomposition of single molecular precursors.

1. 3. 2. 3. 1. The Polyol Method

The hydrolysis of the transition metal ions in polyol (ethylene glycol, diethylene glycol or 1,2-propanediol) solutions with the formation of nanophase binary or mixed metal oxides is traditionally referred to as the polyol method. [152-154] Although the polyol

process was initially aimed at the synthesis of various micrometer to nanometer-sized metallic particles (Co, Ni, Cu, Ag, Pt, Pd, Sn, W, Rh, Ru, $Co_XNi_{(100-X)}$, $Fe_Z[Co_XNi_{(100-X)}]_{(1-Z)}$)[155-157], due to its simplicity and versatility this technique has been successfully extended to other types of nanocrystalline materials, including ferrites. In this process, the metallic particles were obtained by reducing the corresponding metal oxides or hydroxides with a polyol which acts not only as a reducing agent, but also as a solvent for the starting materials and a stabilizing agent for the resulting compounds.[155, 156] When transition metal salts are used as precursor materials, their conversion into the corresponding metal hydroxides will require the presence of sodium hydroxide in the reaction system.[157] It was also observed that the addition of sodium hydroxide into the reaction mixture can affect the rate of the reduction process as well as the size of the as-prepared metallic particles.[156] Because the presence of water in the system can potentially affect the reduction of the metal ions, syntheses in polyol media are usually performed by refluxing the reaction mixture for extended periods of time. Thus, in addition to the water molecules, other organic compounds resulting from the oxidation of the polyols will be also removed during the course of the synthetic process.[155, 157] Several factors, such as the reaction temperature[155, 156], the metal precursor/polyalcohol molar ratio[155] the reaction time[156] and the nature of the noble metal used as seeds in the heterogeneous nucleation of other metals or alloys were found to play an important role on the size of the resulting metallic nanoparticles.[157]

Unlike the metals, the presence of a certain amount of water in the reaction mixture is essential for the preparation of metal oxide nanoparticles through the polyol process. This synthetic pathway, known as “forced hydrolysis in polyol medium” has

been successfully applied to the preparation of various nanocrystalline oxides, such as α-Fe_2O_3[152, 158] and spinel-type ferrites ($CoFe_2O_4$, $NiFe_2O_4$)[153, 154], respectively.

1. 3. 2. 3. 2. Thermal Decomposition of Single Molecular Precursors

A non-hydrolytic synthetic approach extensively used for the preparation of nanocrystalline ferrites is the thermolysis of single molecular precursors (organometallic compounds or metal-fatty acid complexes) in high boiling point organic solvents (long-chain ethers, amines, alkenes).[159-161, 164, 165] A major advantage of such one-pot synthetic route is related to the possibility to obtain large amounts of variable-sized metal oxide nanoparticles with high crystallinity and tight size distributions.[160] The similarity in both the size and the shape of the nanocrystals is critical for the formation of multidimensional architectures (superlattices) which can be used as building blocks for the design of nanoscale optical, electronic and magnetic devices. Several organometallic compounds and metal-fatty acid complexes have been used as precursor materials in the thermolysis process; these compounds along with the corresponding solvents and capping ligands are summarized in the Table 1.2.

Sun *et al.* synthesized highly crystalline MFe_2O_4 (M=Mn, Fe, Co) nanoparticles by refluxing solutions of metal acetylacetonates ($M(acac)_n$, n=1, 2) in phenyl (or benzyl) ether in the presence of 1,2-hexadecanediol as a reducing agent under a protected atmosphere. The as-prepared nanocrystals stabilized with oleic acid and oleyl amine had narrow size distributions ($\sigma<5\%$) and average diameters which can be varied between 3 and 10 nm by increasing the reaction time and temperature. According to them, bigger ferrite particles (10-20 nm) can be obtained through the so-called “seed-mediated

growth" method, which consists of performing the reaction between metal acetylacetonates and 1,2-hexadecanediol in solutions containing variable amounts of the as-prepared nanoparticles (3-10 nm) serving as seeds.[166, 167]

However, because the thermolysis process presents some limitations due to the toxicity and high cost of the organometallic compounds ($(\eta^5\text{-}C_5H_5)CoFe_2(Co)_9$)[165], other metal sources have been considered as potential precursors for the preparation of the nanocrystalline metal oxides. There are several reports on the synthesis of ferrite nanoparticles by the thermal decomposition of the metal-fatty acid complexes.[160, 161, 164] Although most of these compounds are not commercially available, they represent attractive metal sources for the thermolysis reactions since they can be conveniently prepared from simple precursors and decompose at relatively low temperatures, typically around 300^{o}C. For example, Yu *et al.* prepared an iron-oleate complex by dissolving FeOOH into a hot solution of oleic acid in 1-octadecene[161], whereas Jana *et al.* and Park *et al*. obtained the metal precursors by treating the transition metal chlorides with sodium carboxylate (myristate, palmitate, stearate, oleate) salts.[160, 164] The resulting metal-fatty acid complexes are subsequently converted into nanocrystalline ferrites by a thermolysis reaction in hot organic solvents (t~300-320ºC) in the presence of capping agents.[160, 161, 164] Alternatively, Wang *et al*. reported that the transition metal-fatty acid complexes can be obtained by exchange reactions taking place at the interface between the solid and the solution phases of a system containing a sodium fatty acid salt (solid), an aqueous solution of the transition metal salts (solution), and a fatty acid (liquid), respectively. Again, the resulting transition metal-fatty acid complexes undergo a thermolysis reaction

Table 1.2. Survey of Metal Precursors, Solvents and Capping Ligands Used in the Synthesis of Nanocrystalline Ferrites by Thermolysis Method

Ferrite	Metal Precursor	Solvent	Capping Ligand	Particle Morphology	Ref.
γ-Fe_2O_3	$Fe(Cup)_3$ $Cup=C_6H_5N(NO)O^-$	Octylamine	Trioctylamine	Spherical, 5-10 nm	159
Fe_3O_4	FeO(OH)	1-Octadecene	Oleic Acid	Spherical, 6-28 nm	161
	$Fe(acac)_3$	Benzyl Alcohol	Undecanoic acid Dopamine	Spherical, 8 nm 12 nm	162
	$Fe(acac)_3$	Phenyl Ether, 1,2-Dodecanediol	Oleic Acid, Oleylamine	Spherical, 4-14 nm	163
	$Fe(oleate)_3$	1-Hexadecene Octyl Ether 1-Octadecene 1-Eicosene Trioctylamine	Oleic Acid	Spherical, 5 nm 9 nm 12 nm 16 nm 22 nm	160
	$Fe(oleate)_3$	1-Octadecene	Oleic Acid	Spherical, 8-50 nm	164
	$Fe(oleate)_2$	1-Octadecene	Oleic Acid	Cubic, 50 nm	
$CoFe_2O_4$	$(\eta^5\text{-}C_5H_5)CoFe_2(Co)_9$	Octyl Ether	Oleic Acid Oleic Acid, Lauric Acid	Spherical, 6 nm 9 nm	165
MFe_2O_4	$M(acac)_n$, n=2,3 M=Fe, Co, Mn	Fe_3O_4 Phenyl Ether, Benzyl Ether	Oleic Acid, Oleyl Amine	Spherical, Hexagonal 4-20 nm	166
		$CoFe_2O_4$ Phenyl Ether, Benzyl Ether	Oleic Acid, Oleyl Amine	3-20 nm	
		$MnFe_2O_4$ Phenyl Ether, Benzyl Ether	Oleic Acid, Oleyl Amine	7-18 nm	

under solvothermal conditions yielding nanocrystalline ferrites (Fe_3O_4, $CoFe_2O_4$) with an average size of 10 nm and a tight size distribution. The nanoparticles' dimensions can be controlled by varying several parameters, such as the reaction temperature, the capping agent/transition metal ions molar ratio and the nature of the capping ligand.[168]

In addition to the control over the chemical composition and the size of the nanoparticles, another advantage of the thermolysis reactions is represented by the possibility to control the shape of the resulting nanocrystals. The capping agent/metal precursor molar ratio as well as the reaction time and temperature were found to affect not only the size of the ferrite nanocrystals, but also their shape.[169, 170] For example, Zeng *et al*. demonstrated that the increase of the capping ligand/iron precursor molar ratio to 3:1 produces a change of the shape of the oleic acid/oleyl amine-passivated $MnFe_2O_4$ nanocrystals, prepared by the thermolysis of the metal acetylacetonates ($[Fe(acac)_3]/[Mn(acac)_2]=2/1$), from spherical to cubic.[169] Redl and coworkers studied the influence of the reaction time and the amount of capping ligand on the morphology of the iron oxide nanocrystals synthesized by the thermal decomposition of ferrous acetate in a solution containing trioctylamine and oleic acid. By decreasing the oleic acid/ferrous acetate molar ratio from 3:1 to 1.5:1, the morphology of the nanostructured iron oxide particles changes from spherical (4 nm) to a mixture of faceted (14 nm) and spherical (5 nm). A further decrease of the molar ratio to 0.75:1 leads to the formation of cubically-shaped nanocrystals (8 nm) with relatively tight size distribution (8%). Therefore, the decrease of the amount of oleic acid in the reaction solution is accompanied by significant alteration not only of the shape of the nanoparticles, but also of the size and size distribution. If both the molar ratio (0.75:1) and the reaction temperature (255ºC) are

kept constant, the increase of the reaction time from 10 min to 140 min causes a change of the shape of the particles from cubic (8 nm) to octahedral (19 nm).[170]

1.4. References

1. Temple, R. *The Genius of China: 3000 years of science, discovery and invention*, Prion Books Ltd., London, **1998**.
2. Goldman, A. Modern Ferrite Technology, Springer-Verlag New York, **2006**.
3. Dunin-Borkovski, R. E.; McCartney, M. R.; Frankel, R., B.; Bazylinski, D. A.; Posfai, M.; Buseck, P. R. *Science*, **1998**, *282*, 1868.
4. Diebel, C. E.; Proksch, R.; Green, C. R.; Neilson, P.; Walker, M. M. *Nature*, **2000**, *406*, 299.
5. Edwards, H. H.; Schnell, G. D.; Dubois, R. L.; Hutchinson, V. H. *Auk.* **1992**, *109*, 43.
6. Wiltschko, R.; Wiltschko, W. *Magnetic Orientation in Animals*, Springer Verlag, Berlin, **1995**.
7. Smart, L.; Moore, E. *Solid State Chemistry: An Introduction*; Fong & Sons Printers Pte Ltd.: Singapore, **1992**; p. 24, 30, 32, 34, 39.
8. Greenwood, N. N.; Earnshaw, A. *Chemistry of the Elements*; Pergamon Press Ltd.: Oxford, England, **1984**, p. 279.
9. West, A. R. *Basic Solid State Chemistry*; John Wiley & Sons Ltd.: 1984, p. 57, 73, 104, 106, 357.
10. Dunitz, J. D.; Orgel, L. E. *J. Phys. Chem. Solids* **1957**, *3*, 318.

11. O'Neill, H. St. C.; Navrotsky, A. *Amer. Mineralogist* **1983**, *68*, 181.

12. Thompson, P.; Grimes, N.W. *Philosophical Magazine* **1977**, *36*, 501.

13. Hill, R. J.; Craig, J. R.; Gibbs, G. V. *Phys. Chem. Minerals* **1979**, *4*, 317.

14. Ho, J. C.; Hamdeh, H. H.; Chen, Y. Y.; Lin, S. H.; Yao, Y. D.; Willey, R.J.; Oliver, S. A. *Phys. Rev. B* **1995**, *52*(14), 10122.

15. Goya, G. F.; Rechenberg, H. R. ; Chen, M. ; Yelon, W. B. *J. Appl. Phys.* **2000**, *87*(11), 8005.

16. Kamiyama, T.; Haneda, K.; Sato, T.; Ikeda, S.; Asano, H. *Solid State Commun*. **1992**, *87*(7), 563.

17. Ammar, S.; Jouini, N.; Fiévet, F. ; Stephan, O.; Marhic, C.; Richard, C.; Villain, F.; Cartier dit Moulin, Ch.; Brice, S. ; Sainctavit, Ph. *J. Non-Crystalline Solids* **2004**, *345&346*, 658.

18. Kedesdy, H. H.; Tauber, J. *J. Am. Ceram. Soc.* **1956**, *39*, 425.

19. Mahmoud, M. H.; Hamdeh, H. H.; Ho, J. C.; O'Shea, M.J.; Walker, J. C. *J. Magn. Magn. Mater.* **2000,** *220*, 139.

20. Chinnasamy, C. N.; Narayanasamy, A.; Ponpandian, N.; Chattopadhyay, K.; Shinoda, K.; Jeyadevan, B.; Nakatsuka, K.; Furubayashi,T.; Nakatani, I. *Phys. Rev. B* **2001**, *63*, 184108.

21. Šepelák, V.; Baabe, D.; Litterst, F.J.; Becker, K. D. *J. Appl. Phys*. **2000**, *88* (10), 5884.

22. Šepelák, V.; Baabe, D.; Mienert, D.; F.J.; Becker, K. D. *Scr. Materialia* **2003**, *48*, 961.

23. Šepelák, V.; Tkáčová, K; Boldyrev, V. V.; Wißmann, S.; Becker, K. D. *Physica B*

1997, *234-236,* 617.

24. Mozzi, R. L.; Paladino, A. E. *J. Chem. Phys*. **1963**, *39*(2), 435.
25. Zhang, Z. J.; Wang, L. Z.; Chakoumakos, B. C.; Yin, J. S. *J. Am. Chem. Soc.* **1998**, *120*, 1800.
26. Goya, G. F.; Rechenberg, H. R.; Jiang, J. Z. *J. Appl. Phys.* **1998**, *84*(2), 1101.
27. Oliver, S. A. ; Hamdeh, H. H. ; Ho, J. C. *Phys. Rev. B* **1999**, *60*(5), 3400.
28. Li, F. S.; Wang, L.; Wang, J. B.; Zhou, Q. G.; Zhou, X. Z.; Kunkel, H. P.; Williams G. *J. Magn. Magn. Mater*. **2004**, *268*, 332.
29. Mandrus, D.; Keppens, V.; Chakoumakos, B. C. *Mater. Res. Bull*. **1999**, *34*(7), 1013.
30. Jovalekić, Č.; Zdujić, M.; Radaković, A.; Mitrić, M. *Mater. Lett.* **1995**, *24*, 365.
31. Manova, E.; Kunev, B.; Paneva, D.; Mitov, I.; Petrov, L.; Estournés, C.; D'Orleans, C.; Rehspringer, J.-L.; Kurmoo, M. *Chem. Mater*. **2004**, *16*, 5689.
32. Shi, Y.; Ding, J.; Liu, X.; Wang, J. *J. Magn. Magn. Mater.* **1999**, *205*, 249.
33. Ding, J.; Reynolds, T.; Miao, W.F.; McCormick, P. G.; Street, R. *Appl. Phys. Lett.* **1994**, *65* (24), 3135.
34. Ding, J.; McCormick, P. G.; Street, R. *Solid State Commun*. **1995**, *95* (1), 31.
35. Shinde, S. R.; Kulkarni, S. D.; Banpurkar, A. G.; Nawathey-Dixit, R.; Date, S. K.; Ogale, S. B. *J. Appl. Phys.* **2000**, *88*(3), 1566.
36. Son, S.; Taheri, M.; Carpenter, E.; Harris, V. G.; McHenry, M. E. *J. Appl. Phys.* **2002**, *91*(10), 7589.
37. Veintemillas-Verdaguer, S.; Morales, M. P. ; Serna, C. J. *Mater.Lett.* **1998**, *35*, 227.
38. Wang, S.; Xin, H.; Qian, Y. *Mater. Lett*. **1997**, *33*, 113.
39. Yamaguchi, K.; Matsumoto, K.; Fujii, T. *J. Appl. Phys.* **1990**, *67*, 4493.

40. Oswald, P.; Clement, O.; Chambon, C.; Schouman-Claeys, E.; Frija, G. *Magn. Reson. Imaging* **1997**, *15*, 1025.

41. Lawaezeck, R.; Menzel, M.; Pietsch, H. *Appl. Organomet. Chem.* **2004**, *18*, 506.

42. McMichael, R. D.; Shull, R. D.; Swartzendruber, L. J.; Bennett, L. H.; Walson, R. E. *J. Magn. Magn. Mater.* **1992**, *111*, 29.

43. Kang, Y. S.; Risbud, S.; Rabolt, J.F.; Stroeve, P. *Chem. Mater.* **1996**, *8*(9), 2209.

44. Anton, A. I. *J. Magn. Magn. Mater.* **1990**, *85*, 137.

45. Raj, K.; Moskovitz, B.; Casciari, R. *J. Magn. Magn. Mater.* **1995**, *149*, 174.

46. Robinson, D. B. ; Persson, H. H. J. ; Zeng, H. ; Li, G. ; Pourmand, N. ; Sun, S. ; Wang, S. X. *Langmuir* **2005**, *21*, 3096.

47. Grancharov, S. G,; Zeng, H.; Sun, S.; Wang, S. X.; O'Brien, S.; Murray, C. B.; Kirtley, J. R. *J. Phys. Chem. B* **2005**, *109*, 13030.

48. Gee, S. H.; Hong, Y. K.; Erickson, D.W.; Park, M. H.; Sur, J. C. *J. Appl. Phys.* **2003**, *93*(10), 7560.

49. Enomoto, Y.; Tokuyama, M.; Kawasaki, K. *Acta Metall.* **1986**, *34*(11), 2199.

50. Madras, G.; McCoy, B. J. *J. Chem. Phys.* **2002**, *117*(17), 8042.

51. Marqusee, J. A.; Ross, J. *J. Chem. Phys.* **1983**, *79*(1), 373.

52. LaMer, V. K.; Dinegar, R. H *J. Am. Chem. Soc.* **1950**, *72*(11), 4847.

53. Sugimoto, T. *Adv. Colloid Interface Sci.* **1987**, *28*, 65.

54. Beattie, J. K. *Pure & Appl. Chem.* **1989**, *61*(5), 937.

55. Boistelle, R.; Astier, J. P. *J. Cryst. Growth* **1988**, *90*, 14.

56. Dirksen, J. A.; Ring, T. A. *Chem. Eng. Science* **1991**, *46* (10), 2389.

57. Cheon, J.; Kang, N.-J.; Lee, S.-M.; Lee, J.-H.; Yoon, J.-H; Oh, S. J. *J. Am. Chem.*

Soc. **2004**, *126*, 1950.

58. Lifshitz, I. M.; Slyozov, V. V *J. Phys. Chem. Solids* **1961**, *19* (1-2), 35.
59. Wagner, C. *Elecktrochem.* **1961**, *65*, 581.
60. Dadyburjor, D. B.; Ruckenstein, E. *J. Cryst. Growth* **1977**, *40*, 279.
61. Oskam, G.; Hu, Z.; Penn, R. L.; Pesika, N.; Searson, P. C. *Phys. Rev. E* **2002**, *66*, 011403.
62. Vayssières, L.; Chanéac, C. ; Tronc, E. ; Jolivet, J. P. *J. Colloid Interface Sci.* **1998**, *205*, 205.
63. Barker, A. J.; Cage, B.; Russek, S.; Stoldt, C. R. *J. Appl. Phys.* **2005**, *98*, 063528.
64. Bharde, A.; Wani, A.; Shouche, Y.; Joy, P. A.; Bhagavatula, L.V.P.; Sastry, M. *J. Amer. Chem. Soc.* ***2005***, *127,* 9326.
65. Privman, V.; Goia, D. V.; Park, J.; Matijević, E. *J. Colloid Interface Sci.* **1999**, *213*, 36.
66. Sugimoto, T.; Matijević, E. *J. Colloid Interface Sci.* **1980**, *74*(1), 227.
67. Penn, R. L.; Oskam, G.; Strathmann, T. J.; Searson, P. C.; Stone, A. T.; Veblen, D. R. *J. Phys. Chem. B*, **2001**, *105*(11), 2177.
68. Ocaña, M.; Morales, M. P.; Serna, C. J. *J. Colloid Interface Sci.* **1995**, *171*, 85.
69. Zheng, Y.; Cheng, Y.; Wang, Y.; Bao, F. *J. Cryst. Growth* **2005**, *284*, 221.
70. Matijević, E; Scheiner, P. *J. Colloid Interface Sci.* **1978**, *63*, 509.
71. Banfield, J. F.; Welch, S. A.; Zhang, H.; Thompsen Ebert, T.; Penn, R. L. *Science* **2000**, *289*, 751.
72. Niederberger, M.; Krumeich, F.; Hegetschweiler, K.; Nesper, R. *Chem. Mater.* **2002**, *14*(1), 78.

73. Penn, R. L. *J. Phys. Chem. B* **2004**, *108*(34), 12707.

74. Penn, R. L.; Banfield, J. F.; *Science* **1998**, *281*, 969.

75. Gilbert, B.; Zhang, H.; Huang, F.; Finnegan, M. P.; Waychunas, G. A.; Banfield, J. F *Goechem. Trans.* **2003**, *4*(4), 20.

76. Grasset, F.; Labhsetwar, N.; Li, D.; Park, D. C.; Saito, N.; Haneda, H.; Cador, O.; Roisnel, T.; Mornet, S.; Duguet, E.; Portier, J.; Etourneau, J. *Langmuir* **2002**, *18*(21), 8209.

77. Sousa, M. H. ; Tourinho, F. A.; Depeyrot, J.; José da Silva, G.; Lara, M. C. F. L. *J. Phys. Chem. B* **2001**, *105*(6), 1168.

78. Chen, J. P.; Sorensen, C. M.; Klabunde, K. J.; Hadjipanayis, G. C.; Devlin, E.; Kostikas, A. *Phys. Rev. B* **1996**, *54*(13), 9288.

79. Ryu, B.-H.; Chang, H.-J.; Choi, Y.-M.; Kong, K.-J.; Lee, J.-O.; Kim, C.-G.; Jung, H.-K.; Byun, J.-H. *Phys. Stat. Sol.* **2004**, *201*(8), 1855.

80. Hsu, W.-C.; Chen, S.C.; Kuo, P. C.; Lie, C. T.; Tsai, W. S. *Mat. Sci. Eng. B* **2004**, *111*, 142.

81. Tada, M.; Hatanaka, S.; Sanbonsugi, H.; Matsushita, N.; Abe, M. *J. Appl. Phys.* **2003**, *93*(10), 7566.

82. Kuo, P. C.; Tsai, T. S. *J. Appl. Phys.* **1989**, *65*(11), 4349.

83. Lyon, J. L.; Fleming, D. A.; Stone, M. B.; Schiffer, P.; Williams, M. E. *Nano Lett.* **2004**, *4*(4), 719.

84. Kundu, A.; Upadhyay, C.; Verma, H. C. *Phys. Lett. A* **2003**, *311*, 410.

85. Bruce, I. J.; Taylor, J.; Todd, M.; Davies, M. J.; Borioni, E.; Sangregorio, C.; Sen, T. *J. Magn. Magn. Mater.* **2004**, *284*, 145.

86. Sharma, R. K.; Suwalka, O. ; Lakshmi, N. ; Venugopalan, K.; Banerjee, A.; Joy, P. A. *Mat. Lett.* **2005**, *59*, 3402.

87. Khoudiakov, M.; Gupta, M. C.; Deevi, S. *Nanotechnology* **2004**, *15*, 987.

88. Yamamoto, H.; Nissato, Y. *IEEE Trans.* **2002**, *38*(5), 3488.

89. Kim, D.K.; Mikhaylova, M.; Zhang, Y.; Muhammed, M. *Chem. Mater.* **2003**, *15*(8), 1617.

90. Si, S.; Kotal, A.; Mandal, T. K.; Giri, S.; Nakamura, H.; Kohara, T. *Chem. Mater.* **2004**, *16*(18), 3489.

91. Kim, C. S.; Yi, Y. S.; Park, K.-T.; Namgung, H.; Lee, J.-G. *J. Appl. Phys.* **1999**, *35*(8), 5223.

92. Kim, W. C.; Park, S. I.; Kim, S. J.; Lee, S. W.; Kim, C. S. *J. Appl. Phys.* **2000**, *87*(9), 6241.

93. Kim, W. C.; Kim, S. J.; Sur, J. C.; Kim, C. S. *J. Magn. Magn. Mater.* **2002**, *242-245*, 197.

94. Lee, S. W.; Ryu, Y. G.; Yang, K. J.; Jung, K.-D.; An, S. Y.; Kim, C. S. *J. Appl. Phys.* **2002**, *91*(10), 7610.

95. An, S. Y.; Shim, I.-B.; Kim, C. S. *J. Appl. Phys.* **2002**, *91*(10), 8465.

96. Pullar, R. C.; Bhattacharya, A. K. *Mat. Lett.* **2002**, *57*, 537.

97. Hernandez, B. A.; Chang, K.-S.; Fisher, E. R.; Dorhout, P. K. *Chem. Mater.* **2002**, *14*(2), 480.

98. Barbooram, K.; Ye, Z.-G. *Chem. Mater.* **2006**, *18*(2), 532.

99. Fantozzi, G.; Chevalier, J.; Guilhot, B. *Adv. Eng. Mater.* **2001**, *3*(8), 563.

100. Del Castillo, J.; Rodríguez, V. D.; Yanes, A. C.; Méndez-Ramos, J.; Torres, M. E.

Nanotechnology **2005**, 16, S300.

101. Hu, Q.; Zhao, J.; Wang; Zhao, J.; Wang, Y.; Zhu, L.; Li, M.; Li, G.; Wang, Y.; Ge, F. *J. Molec. Catalysis A: Chem.* **2003**, *200*, 271.
102. Tseng, I.-H., Wu, J. C. S.; Chou, H.-Y. *J. Catalysis* **2004**, *221*, 432.
103. Hench, L. L.; West, J. K. *Chem. Rev.* **1990**, *90*(1), 33.
104. Brinker, C. J.; Scherer, G. W. *Sol-Gel Science: The Physics and Chemistry of Sol-Gel Processing*; Academic Press, Inc.: San Diego, 1990, p. 112.
105. Livage, J.; Henry, M.; Sanchez, C. *Prog. Solid St. Chem.* **1988**, *18*, 259.
106. Plocek, J.; Hutlová, A.; Nižňansky, D.; Buršík, J.; Rehspringer, J.-L.; Mička, Z. *J. Non-Cryst. Solids* **2003**, *315*, 70.
107. Li, J.-J.; Xu, W.; Yuan, H.-M.; Chen, J.-S. *Solid State Commun.* **2004**, *131*, 519.
108. He, X.; Song, G.; Zhu, J. *Mater. Lett.* **2005**, *59*, 1941.
109. Veith, M.; Haas, M.; Huch, V. *Chem. Mater.* **2005**, *17*(1), 95.
110. Cansell, F.; Chevalier, B.; Demourgues, A.; Etourneau, J.; Even, C.; Garrabos, Y.; Pessey, V.; Petit, S.; Tressaud, A.; Well, F. *J. Mater. Chem.* **1999**, *9*, 67.
111. Li, J.; Chen, Z.; Wang, R.-J.; Proserpio, D. M. *Coord. Chem. Rev.* **1999**, *190-192*, 707.
112. Sun, Y.-P. *Supercritical Fluid Technology in Materials Science and Engineering*; Marcel Dekker, Inc.: New York, 2002, p. 335.
113. Yu, S.-H.; Fujino, T.; Yoshimura, M. *J. Magn. Magn. Mater.* **2003**, *256*, 420.
114. Wang, Y.; Tao, J.; Zhu, X. *J. Am. Ceram. Soc.* **2005**, *88*(12), 3535.
115. Chaianansutcharit, S.; Mekaswandumrong, O.; Praserthdam, P. *Crystal Growth & Design* **2006**, *6*(1), 40.

116. Hou, Y.; Yu, J.; Gao, S. *J. Mater. Chem.* **2003**, *13*, 1983.

117. Thimmaiah, S.; Rajamathi, M.; Singh, N.; Bera, P.; Meldrum, F.; Chandrasekhar, N.; Seshadri, R. *J. Mater. Chem.* **2001**, *11*, 3215.

118. Rivadulla, J. F.; Vergara, M. C.; Blanco, M. C.; López-Quintela, M. A.; Rivas, J. *J. Phys. Chem. B* **1997**, *101*(44), 8897.

119. Ohde, H.; Hunt, F.; Wai, C. M. *Chem. Mater.* **2001**, *13*(11), 4130.

120. Qi, L.; Ma, J.; Shen, J. *J. Colloid Interface Sci.* **1997**, *186*(2), 498.

121. Touronde, R.; Girard, P.; Maire, G. ; Kizling, J.; Boutonnet-Kizling, M.; Stenius, P. *Colloids and Surfaces* **1992**, *67*, 9.

122. Wu, M.-L.; Chen, D.-H.; Huang, T.-C. *J. Colloid Interface Sci.* **2001**, *243*(1), 102.

123. Wu, M.-L.; Chen, D.-H.; Huang, T.-C. *Chem. Mater.* **2001**, *13*(2), 599.

124. Ohde, H; Rodriguez, J. M.; Ye, X.-R.; Wai, C. M.; *Chem. Comm.* **2000**, 2353.

125. Jeunieau, L.; Verbouwe, W.; Rousseau, E.; Van der Auweraer, M.; Nagy, J. B. *Langmuir*, **2000**, *16*(4), 1602.

126. Agnoli, F.; Zhou, W. L.; O' Connor, C. J. *Adv. Mater.* **2001**, *13*(22), 1697.

127. Sangregorio, C.; Carpenter, E. E.; O' Connor, C. J. *Mater. Res. Soc. Symp. Proc.* **1999***, 577,* 435.

128. Wang, H.; Zhang, J.-R.; Zhu, J.-J. *J. Crystal Growth* **2002**, *246*(1-2), 161.

129. Qingmin, Z.; Fuzhi, H.; Yan, L. *Colloids and Interfaces, A: Physicochemical & Engineering Aspects* **2005**, *257-258*, 497.

130. Xu, J.; Li, Y. *J. Colloid Interface Sci.* **2003**, *259*(2), 275.

131. Chen, D.; Gao, L. *J. Colloid Interface Sci.* **2004**, *279*(1), 137.

132. Lee, M. S.; Park, S. S.; Lee, G.-D.; Ju, C.-S.; Hong, S.-S. *Catalysis Today* **2005**,

101(3-4), 137.

133. Carpenter, E. E; O' Connor, C.J.; Harris, V.G. *J. Appl. Phys.* **1999**, *85*(8), 5175.
134. Liu, C.; Zou, B.; Rondinone, A. J.; Zhang, Z. J. *J. Phys. Chem. B* **2000**, *104*(6), 1141.
135. Feltin, N.; Pileni, M. P. *Langmuir* **1997**, *13*(15), 3927.
136. Moumen, N.; Pileni, M. P. *Chem. Mater.* **1996**, *8*(5), 1128.
137. Kale, A.; Gubbala, S.; Misra, R. D. K. *J. Magn. Magn. Mater.* **2004**, *277*, 350.
138. Poddar, P.; Srikanth, H.; Morrison, S. A.; Carpenter, E. E. *J. Magn. Magn. Mater.* **2005**, *288*, 443.
139. Košak, A.; Makovec, D.; Žnidaršič, A.; Drofenik, M. *J. Eur. Ceram. Soc.* **2004**, *24*, 959.
140. Morrison, S. A.; Cahill, C. L.; Carpenter, E. E.; Swaminathan, R.; McHenry, M. E. Harris, V. G. *J. Appl. Phys.* **2004**, *95*(11), 6392.
141. Uskoković, V.; Drofenik, M. *Surf. Rev. Lett.* **2005**, *12*(1), 97.
142. Ganguli, D.; Ganguli, M. Inorganic *Particle. Synthesis via Maacroemulsion and Microemulsion. A Micrometer to Nanometer Landscape*; Kluwer Academic/ Plenum Academic: New York, Boston, Dordrecht, London, Moscow, 2003; p.1-3, 8, 10, 29, 32, 68.
143. Dresco, P. A.; Zaitsev, V. S.; Gambino, R. J.; Chu, B. *Langmuir* **1999**, *15*(6), 1945.
144. Makovek, D.; Košak, A.; Drofenik, M. *Nanotechnology* **2004**, *15*, S160.
145. Nakanishi, T.; Iida, H.; Osaka, T. *Chem. Lett.* **2003**, *32*(12), 1166.
146. Morrison, S. A.; Cahill, C. L.; Carpenter, E. E.; Harris, V. G. *Ind. Eng. Chem. Res*. **2006**, *45*(3), 1217.

147. Lee, Y.; Lee, J.; Bae, C. J.; Park, J.-G.; Noh, H.-J.; Park, J.-H.; Hyeon, T. *Adv. Funct. Mater.* **2005**, *15*(3), 503.

148. Uskoković, V.; Drofenik, M.; Ban, *I. J. Magn. Magn. Mater.* **2004**, *284*, 294.

149. Vestal, C. R.; Zhang, Z. J. *Chem. Mater.* **2002**, *14*(9), 3817.

150. Capek, I. *Adv. Colloid Interface Sci*. **2004**, *110*, 49.

151. Lange, R. F. *Surfactants: A Practical Handbook*; Hanser-Gardner Publications: Cincinnatti, 1999, p.1-5.

152. Feldmann, C. *Adv. Mater.* **2001**, *13*(17), 1301.

153. Chkoundali, S.; Ammar, S.; Jouini, N.; Fiévet, F.; Molinié, P.; Danot, M.; Villan, F.; Grenèche, J.-M. *J. Phys.: Condens. Matter.* **2004**, *16*, 4357.

154. Ammar, S.; Helfen, A.; Jouini, N.; Fiévet, F.; Rosenman, I.; Villain, F.; Molinié, P.; Danot, M.; *J. Mater. Chem.* **2001**, *11*, 186.

155. Fiévet, F.; Lagier, J. P. ; Blin, B. ; Beaudoin, B.; Figlarz, M. *Solid State Ionics* **1989**, *32/33*, 198.

156. Kurihara, L. K.; Chow, G. M.; Schoen, P. E. *Nanostruct. Mater.* **1995**, *5*(6), 607.

157. Toneguzzo, P.; Viau, G.; Acher, O.; Fièvet-Vincent, F.; Fièvet, F. *Adv. Mater.* **1998**, *10*(13), 1032.

158. Feldmann, C.; Jungk, H.-O. *Angew. Chem. Int. Ed.* **2001**, *40*(2), 359.

159. Rockenberger, J.; Scher, E. C.; Alivisatos, A. P. *J. Am.. Chem. Soc.* **1999**, *121*(49), 11595.

160. Park, J.; An, K.; Hwang, Y.; Park, J.-G.; Noh, H.-J.; Kim, J.-Y.; Park, J.-H.; Hwang, N.-M.; Hyeon, T. *Nature Mater.* **2004**, *3*, 891.

161. Yu, W. W.; Falkner, J. C.; Yavuz, C. T.; Colvin, V. L. *Chem. Com.* **2004**, 2306.

162. Pinna, N.; Grancharov, S.; Beato, P.; Bonville, P.; Antonietti, M. Niederberger, M. *Chem. Mater.* **2005**, *17*(11), 3044.

163. Yang, T.; Shen, C.; Li, Z.; Zhang, H.; Xiao, C.; Chen, S.; Xu, Z.; Shi, D.; Li, J.; Gao, H. *J. Phys. Chem*. B **2005**, *109*(49), 23233.

164. Jana, N. R.; Chen, Y.; Peng, X. *Chem. Mater.* **2004**, *16*, 3931.

165. Hyeon, T.; Chung, Y.; Park, J.; Lee, S. S.; Kim, Y.-W.; Park, B.H. *J. Phys. Chem. B* 2002*, 106*(27)*,* 6831.

166. Sun, S.; Zeng, H.; Robinson, D. B.; Raoux, S.; Rice, P. M.; Wang, S. X.; Li, G. *J. Am. Chem. Soc.* **2004**, *126*(1), 273.

167. Sun, S.; Zeng, H. *J. Am. Chem. Soc.* **2002**, *124*(28), 8204.

168. Wang, X.; Zhuang, J.; Peng, Q.; Li, Y. *Nature* **2005**, *437*, 121.

169. Zeng, H.; Rice, P. M.; Wang, S. X.; Sun, S. *J. Am. Chem. Soc.* **2004**, *126*(37), 11458.

170. Redl, F. X.; Black, C. T.; Papaefthymiou, G. C.; Sandstrom, R. L.; Yin, M.; Zeng, H.; Murray, C. B.; O'Brien, S. P. *J. Am. Chem. Soc.* **2004**, *126*(44), 14583.

CHAPTER 2

Reactivity of 3d Transition Metal Cations in Diethylene Glycol Solutions. Synthesis of Hydrocarbon-Soluble Transition Metal Ferrite Nanocrystals

2.1 Introduction

Transition metal ferrites are well-established materials for various technological applications due to their useful magnetic properties. Their composition, both elemental and stoichiometric, is easily altered without major structural changes, which permits tuning their ferrimagnetic properties in a wide range. Bringing the dimensionality of ferrites to the nanometer scale opens up new perspectives for cutting-edge applications, in high-density magnetic and magneto-optic recording media, ferrofluids, drug carriers, color imaging, and MRI contrast agents, etc.[1-5] Additionally, high stability in different chemical environment, compared to metallic nanoparticles, makes ferrites particularly useful for biological and medical applications.[6,7] Most of these areas require nanomaterials with the structure of discrete nanoparticles that can be dispersed or dissolved in some common solvents. Synthesis of nanocrystalline ferrites has been achieved using microemulsion techniques, where agglomeration is suppressed by the micellar structure of the reaction fluids. These

techniques exploit the geometrically restricted growth of particles in the nanometer space defined by either normal (oil in water) or inverse (water in oil) microemulsions stabilized by surfactants.[8-13]

However, once products are liberated from solvent and surfactant, the resulting nanopowders would not be soluble in regular solvents. Solubility is one of the biggest challenges since nanocrystals of metal oxides tend to agglomerate due to their large surface energy. This problem can be overcome by passivating the surface of the (nano)crystal by attaching capping ligands. There are a number of reports on successful synthesis of nanoparticles of metals[14-16] and metal chalcogenides[17-22] stabilized by complexing with ligands containing long hydrocarbon chains. However, only a few publications deal with soluble nanoparticles of metal oxides.[23-26] Although the developed methods for synthesis of capped metal oxides are reported to produce high-quality nanoparticles, their applicability at industrial scale remains questionable for a number of reasons, such as hazardous nature of precursors, hazardous or complicated process, high cost of the materials, and/or low product yield. The latter issue is worth pointing out with a special emphasis, since analysis of the literature data indicates that the yield of nanocrystalline products is rarely reported.

In this work, we intended to develop a new method for synthesis of transition metal ferrites with the structure of discrete nanoparticles. This method was supposed to provide a high product yield, be versatile enough so that different transition metals can be used, and be easily scalable. To ensure the nanocrystalline state of the ferrites, their surface metal atoms would be complexed with capping ligands containing hydrocarbon chains of variable lengths as substituents. An initial issue for the designed strategy was to find a way to control kinetics of the nanoparticles growth. After evaluation of different types of reactions, we excluded ion metathesis reactions that usually run instantaneously yielding precipitates of a random morphology. The reaction of our choice is the

hydrolysis of metal complexes that can be performed in nonaqueous solutions. It seems that the rate of this reaction might be adjusted by varying either the concentration of water in nonaqueous solutions or the temperature. The nonaqueous approach seems also to be beneficial for solving the problem of the nanocrystals surface composition.

2.2 Experimental

2.2.1. Reagents. Chemicals and solvents were used as received from Aldrich, $ZnCl_2$ 98%, $FeCl_2{\cdot}4H_2O$ 99%, $CoCl_2{\cdot}6H_2O$ 98%, $FeCl_3{\cdot}6H_2O$ 97%, $MnCl_2{\cdot}4H_2O$ 98+%, $CuCl_2{\cdot}2H_2O$ 99+%, NaOH 97% (20-40 mesh beads), diethylene glycol 99%, myristic acid 99.5%, oleic acid 90%, phenyl ether 99%, and methyl alcohol 99.8%, and from Alfa Aesar, $CoCl_2$ 99.7%, $CoBr_2$ (Co 26.6%), $NiCl_2{\cdot}6H_2O$ 99.3%, and $NaOCH_3$ 98%.

The air-sensitive chemicals were manipulated in a VAC glovebox with a nitrogen atmosphere. Syntheses were carried using Schlenk technique under argon.

2.2.2. Synthesis Methods

2.2.2.1 Preparation of Metal Ferrite Nanoparticles at Room- Temperature.

A 1 mmol amount of $MCl_2{\cdot}nH_2O$ (M = Fe, Co, or Zn) and 2 mmol of $FeCl_3{\cdot}6H_2O$ were dissolved in 20 g of diethylene glycol (DEG) in a Schlenk flask under protection with argon. Separately, 8 mmol of NaOH was dissolved in 10 g of diethylene glycol. A solution of NaOH was added to solution of metal chlorides while stirring at room temperature causing an immediate color change. A mixture of 3.00 g of water in 3.00 g of diethylene glycol was added to the above solution. As the liquid turned turbid, the

reaction was stopped by adding 1 mmol of myristic acid dissolved in 10 mL of methanol. This addition caused immediate precipitation of solids. The mixture was stirred for 30-60 min at room temperature and then centrifuged. The precipitate was washed with methanol and redissolved in 20 mL of phenyl ether. The resulting solution was thermally treated in a Schlenk flask under protecting flow of argon. The temperature was raised to 220 °C in the course of 30 min and kept for another 10 min. After cooling, the solution was mixed with 1-2 volumes of methanol and the precipitate was separated by centrifuging, washed with methanol, and dried under opened air or stored moistened with methanol. A typical yield of dark brown powders was 0.35-0.40 g. Powder X-ray diffraction data were consistent with a spinel structure.

2.2.2.2. Preparation of Metal Ferrite Nanoparticles by the Elevated- Temperature Method.

$MnFe_2O_4$ (Method A)

A 2 mmol amount of $MnCl_2 \cdot 4H_2O$ and 4 mmol of $FeCl_3.6H_2O$ were dissolved in 40 g of diethylene glycol in a Schlenk flask under protection with argon. Separately, 16 mmol of NaOH was dissolved in 40 g of diethylene glycol. A solution of NaOH was added to solution of metal chlorides while stirring at room temperature causing an immediate color change. After 4 h, the temperature of solution was raised during 1 h to 210-220 °C and then kept constant for 0.5 h. As the solution turned turbid, the reaction was terminated by adding 2.3 mmol of oleic acid dissolved in 20 g of DEG. This addition caused immediate precipitation of solids. The mixture was cooled to room temperature and then centrifuged. The precipitate was washed with methanol and redissolved in 20 mL of toluene. The

resulting solution was centrifuged and mixed with 1-2 volumes of methanol. The precipitate was separated by centrifuging, washed with methanol, and dried under opened air or stored moistened with methanol. The yield of dark brown powder was 0.53 g.

$MnFe_2O_4$ (Method B)

A 1 mmol amount of $MnCl_2 \cdot 4H_2O$ and 2 mmol of $FeCl_3 \cdot 6H_2O$ were dissolved in 100 g of diethylene glycol in a Schlenk flask under protection with argon. Separately, 8 mmol of NaOH was dissolved in 40 g of diethylene glycol. A solution of NaOH was added to solution of metal chlorides while stirring at room temperature causing an immediate color change. After 4 h, the temperature of the resulting solution was raised during 1 h to 200-210 °C and then kept constant for 0.5 h. As the solution turned turbid, the reaction was terminated by adding 1 mmol of oleic acid dissolved in 20 g of DEG. This addition caused immediate precipitation of solids. The mixture was cooled to room temperature and then centrifuged. The precipitate was washed with methanol and redissolved in 10 mL of toluene. The resulting solution was centrifuged and mixed with 1-2 volumes of methanol. The precipitate was separated by centrifuging, washed with methanol, and dried under opened air or stored moistened with methanol. The yield of dark brown powder was 0.25 g.

$FeFe_2O_4$ (Method A)

A 2 mmol amount of $FeCl_2 \cdot 4H_2O$ and 4 mmol of $FeCl_3 \cdot 6H2O$ were dissolved in 80 g of diethylene glycol in a Schlenk flask under protection with argon. Separately, 16 mmol of NaOH was dissolved in 40 g of diethylene glycol. A solution of NaOH was added to solution of metal chlorides while stirring at room temperature causing an immediate color

change. The temperature of the resulting solution was raised during 1-1.5 h to 210- 220 °C and then kept constant for 0.5-1 h. As the solution turned turbid, the reaction was terminated by adding 2.6 mmol of oleic acid dissolved in 20 g of DEG. This addition caused immediate precipitation of solids. The mixture was cooled to room temperature and then centrifuged. The precipitate was washed with methanol and redissolved in 20 mL of toluene. The resulting solution was centrifuged and mixed with 1-2 volumes of methanol. The precipitate was separated by centrifuging, washed with methanol, and dried under opened air or stored moistened with methanol. The yield of dark brown powder was 0.511 g.

$CoFe_2O_4$ (Method A)

A 2 mmol amount of $CoCl_2 \cdot 6H_2O$ and 4 mmol of $FeCl_3 \cdot 6H_2O$ were dissolved in 40 g of diethylene glycol in a Schlenk flask under protection with argon. Separately, 16 mmol of NaOH was dissolved in 20 g of diethylene glycol. A solution of NaOH was added to solution of metal chlorides while stirring at room temperature causing an immediate color change. After 1 h, the temperature of solution was raised during 1.5 h to 180-190 °C and then kept constant for 1 h. As the solution turned turbid, the reaction was terminated by adding 2 mmol of oleic acid dissolved in 20 g of DEG. This addition caused immediate precipitation of solids. The mixture was cooled to room temperature and then centrifuged. The precipitate was washed with methanol and redissolved in 20 mL of toluene. The resulting solution was centrifuged and mixed with 1-2 volumes of methanol. The precipitate was separated by centrifuging, washed with methanol, and dried under opened air or stored moistened with methanol. The isolated yield of the obtained dark brown powder was 0.5 g.

$CoFe_2O_4$ (Method B)

A 2 mmol amount of $CoCl_2 \cdot H_2O$ and 4 mmol of $FeCl_3 \cdot 6H_2O$ were dissolved in 80 g of diethylene glycol in a Schlenk flask under protection with argon. Separately, 16 mmol of NaOH was dissolved in 40 g of diethylene glycol. A solution of NaOH was added to solution of metal chlorides while stirring at room temperature causing an immediate color change. After 2-2.5 h, the temperature of the resulting solution was raised during 1 h to 220 °C and then kept constant for 0.5 h. As the solution turned turbid, the reaction was terminated by adding 2.5 mmol of oleic acid dissolved in 20 g of DEG. This addition caused immediate precipitation of solids. The mixture was cooled to room temperature and then centrifuged. The precipitate was washed with methanol and redissolved in 20 mL of toluene. The resulting solution was centrifuged and mixed with 1-2 volumes of methanol. The precipitate was separated by centrifuging, washed with methanol, and dried under opened air or stored moistened with methanol. The isolated yield of dark brown powder was 0.5 g.

$NiFe_2O_4$ (Method A)

A 2 mmol amount of $NiCl_2 \cdot H_2O$ and 4 mmol of $FeCl_3 \cdot H_2O$ were dissolved in 40 g of diethylene glycol in a Schlenk flask under protection with argon. Separately, 16 mmol of NaOH was dissolved in 40 g of diethylene glycol. A solution of NaOH was added to solution of metal chlorides while stirring at room temperature causing an immediate color change. After 4 h, a solution 1.2 g of water + 15 g of DEG was added in three equal portions while the temperature was raised during 1-1.5 h to 200- 210°C. Finally, the temperature was kept constant for 0.5-1 h. As the solution turned turbid, the reaction was terminated by adding 2.6 mmol of oleic acid dissolved in 20 g of DEG. This addition

caused immediate precipitation of solids. The mixture was cooled to room temperature and then centrifuged. The precipitate was washed with methanol and redissolved in 20 mL of toluene. The resulting solution was centrifuged and mixed with 1-2 volumes of methanol. The precipitate was separated by centrifuging, washed with methanol, and dried under opened air or stored moistened with ethanol. The isolated yield of dark brown powder was 0.5 g.

$NiFe_2O_4$ (Method B)

A 2 mmol amount of $NiCl_2 \cdot 6H_2O$ and 4 mmol of $FeCl_3 \cdot 6H_2O$ were dissolved in 100 g of diethylene glycol in a Schlenk flask under protection with argon. Separately, 16 mmol of NaOH was dissolved in 50 g of diethylene glycol. A solution of NaOH was added to solution of metal chlorides while stirring at room temperature causing an immediate color change. After 4 h, 1.0 g of water mixed with 10 g of DEG was added in two equal portions while temperature was raised during 1-1.5 h to 200-210 °C. Finally, the temperature was kept constant for 0.5-1 h. As the solution turned turbid, the reaction was terminated by adding 2 mmol of oleic acid dissolved in 20 g of DEG. This addition caused immediate precipitation of solids. The mixture was cooled to room temperature and then centrifuged. The precipitate was washed with methanol and redissolved in 20 mL of toluene. The resulting solution was centrifuged and mixed with 1-2 volumes of methanol. The precipitate was separated by centrifuging, washed with methanol, and dried under opened air or stored moistened with methanol. The yield of dark brown powder was 0.525 g.

$ZnFe_2O_4$ (Method A)

A 1 mmol amount of $ZnCl_2$ and 2 mmol of $FeCl_3 \cdot 6H_2O$ were dissolved in 20 g of diethylene glycol in a Schlenk flask under protection with argon. Separately, 8 mmol of NaOH was dissolved in 10 g of diethylene glycol. A solution of NaOH was added to solution of metal chlorides while stirring at room temperature causing an immediate color change. After 2-2.5 h, the temperature of the resulting solution was raised during 1 h to 210 °C and then kept constant for another1 h. As the solution turned turbid, the reaction was terminated by adding 1.25 mmol of oleic acid dissolved in 10 g of DEG. This addition caused immediate precipitation of solids. The mixture was cooled to room temperature and then centrifuged. The precipitate was washed with methanol and redissolved in 20 mL of toluene. The resulting solution was centrifuged and mixed with 1-2 volumes of methanol. The precipitate was separated by centrifuging, washed with methanol, and dried under opened air or stored moistened with methanol. The isolated yield of a brown powder was 0.32 g.

$ZnFe_2O_4$ (Method B)

A 2 mmol amount of $ZnCl_2$ and 4 mmol of $FeCl_3 \cdot 6H_2O$ were dissolved in 40 g of diethylene glycol in a Schlenk flask under protection with argon. Separately, 16 mmol of NaOH was dissolved in 40 g of diethylene glycol. A solution of NaOH was added to solution of metal chlorides while stirring at room temperature causing an immediate color change. After 2-2.5 h, the temperature of the resulting solution was raised during 1 h to 210 °C and then kept constant for another1 h. As the solution turned turbid, the reaction was terminated by adding 2.5 mmol of oleic acid dissolved in 20 g of DEG. This addition caused immediate precipitation of solids. The mixture was cooled to room temperature

and then centrifuged. The precipitate was washed with methanol and redissolved in 20 mL of toluene. The resulting solution was centrifuged and mixed with 1-2 volumes of methanol. The precipitate was separated by centrifuging, washed with methanol, and dried under opened air or stored moistened with methanol. The isolated yield of a brown powder was 0.5 g.

2.2.3. Characterization Techniques

Electron microscopy (TEM, HRTEM), EDX, and SAD were performed on a JEOL 2010 transmission electron microscope. The samples were prepared by depositing the toluene solutions containing ferrite nanoparticles on the carbon-coated copper grids and drying at room temperature. The powder X-ray diffraction measurements were performed using a Philips X`Pert system equipped with a graphite monochromator (CuKα radiation, λ = 1.54056 Å); the X-ray diffraction patterns were recorded from 20 to 95 (2θ value) and analyzed using Philips X`Pert Suite of Programs. The IR spectra were recorded over the range 4000-500cm^{-1} with a Perkin-Elmer 1600 spectrometer; the samples were prepared as KBr pellets. Elemental analysis was performed by Galbraith Laboratories, Inc. on the powders resulted after sintering the ferrite nanoparticles.

2.3 Results and Discussion

2.3.1 Study of the reactivity of 3d transition metal cations in diethylene glycol solutions

The newly designed method is different from currently available methods by its controlled stepwise character. Every step is responsible for a particular process, such as

metal complexation, hydrolysis/condensation, and terminating/capping ligation. Preliminary investigations revealed that diethylene glycol (DEG) can function as a complexing agent and a solvent for performing the synthesis. It remains liquid in a wide range of temperatures (-10 to 245°C) and has a high dielectric constant ($\varepsilon = 32$) that enables it to dissolve polar and ionic substances. In addition, the structure of its molecule is ideal for forming chelated complexes with metals, either neutral or anionic when its molecules are deprotonated. Application of DEG as a solvent was reported for synthesis of ZnO nanopowder by thermal decomposition of zinc acetate hydrate.[27]

Many of the first-row transition metal chlorides, both hydrated and anhydrous, are soluble in DEG, and this property was used for preparing their 0.1 or 0.2 *m* stock solutions. The tested cations include Mn^{2+}, Fe^{2+}, Fe^{3+}, Co^{2+}, Ni^{2+}, Cu^{2+}, and Zn^{2+}. Anhydrous sodium hydroxide is also soluble in DEG, and its stock 0.8 *m* solution was used to perform reactions with metal precursors. Mixing both solutions in equivalent quantities usually causes immediate color change (in case of open-shell cations) without precipitation of any solids in all cases except for Cu^{2+}. In the case of DEG and $CoCl_2 \cdot 6H_2O$, we found that its original 0.1 *m* deep blue solution turns to deep purple upon addition of 2 equiv of NaOH. The resulting solution is air-sensitive and turns brown on contact with oxygen. This can be explained by an increased energy splitting between metal orbitals (like between t_{2g} and e_g in octahedral complexes) when the softer ligands are replaced with the harder ones. Evidently, this facilitates oxidation of d^7 Co^{2+} into d^6 Co^{3+} cation. The reaction between $CoCl_2$ and NaOH was also tested in solutions of different polyols such as ethylene glycol and 1,1,1-tris(hydroxymethyl)propane (50% solution in ethanol), and it was found that precipitation of cobalt hydroxo salts (or

hydroxide) occurs instantaneously. This indicates the unique chelating properties of DEG that help to stabilize the complexed Co^{2+} in basic solution.

Two alternative scenarios were proposed for this observation. According to one, the softer Cl^- ligands are substituted with the harder OH^- in the inner sphere, but the metal atom remains chelated with DEG; according to the other, ligands remain intact, but chelated complex becomes deprotonated, so that the softer alcohol ligand is converted into the harder alkoxide. To identify the right path, similar reaction (with Co^{2+}) was performed in different solvent, diethylene glycol monobutyl ether that cannot form a dianion as DEG does but has the same chelating strength. Mixing solutions of cobalt chloride and sodium hydroxide in this solvent caused immediate precipitation of cobalt hydroxy salts or cobalt hydroxide. This observation indicates that hydroxo groups of DEG are involved in the process and, thus, supports the second mechanism (Scheme 2.1). We also observed that precipitation of metal oxides does not happen even when the alkaline DEG solutions of anhydrous salts are heated to temperatures above 200°C. This probably would be different with a neutral dihydroxo complex and an alcohol form of DEG. Another method for identification of the reaction pathway would be spectroscopic, but unfortunately, due to band broadening, evaluation of the UV-vis spectra of DEG solutions containing $CoBr_2$ instead of $CoCl_2$ and $NaH(OCH_2CH_2)_2O$ or $NaOCH_3$ instead of NaOH was inconclusive. The metal DEG complexes undergo nucleophilic substitution reactions when the temperature or concentration of water in the system is increased. This causes the beginning of condensation of mononuclear hydroxide reactive intermediates and eventually leads to precipitation of metal hydroxides or oxides (Scheme 2.1). The advantage of this method over a simple ion metathesis reaction is that the rate of nucleo-

philic substitution reaction with neutral molecules of water is much lower. The crystal growth is slow enough to be monitored visually or using optical methods, and this process can be stopped at any moment. The reaction is terminated by adding a capping ligand that binds to the surface of growing nanoparticles and passivates it. Due to long hydrocarbon chains of capping ligands, the nanoparticles become insoluble in highly polar solvent DEG and immediately precipitate. We tested several long-chain carboxylates for their activity and found that in a form of sodium salts they did not react with metal oxide nanoparticles; only corresponding acids were reactive. In this study oleic $CH_3(CH_2)_7CHCH(CH_2)_7COOH$ and myristic $CH_3(CH_2)_{12}COOH$ acids were used as capping ligands. The described results have been used as a base for synthesis of the nanoscale metal oxides $M^{II}Fe^{III}{}_2O_4$ that have a cubic structure of spinel or inversed spinel as bulk solids. Solutions of two metal salts, $FeCl_3$ and MCl_2 (M = Mn, Fe, Co, Ni, and Zn), were used in stoichiometric ratio 2:1. We also tried to synthesize nanoparticles of γ-Fe_2O_3 that has the same crystal structure.

2.3.2. Synthesis of Ferrite Nanoparticles by Room-Temperature Hydrolysis

This method was applied for synthesis of Fe, Co, and Zn ferrites. The diethylene glycol (DEG) solution of metal chlorides containing a stoichiometric quantity of sodium hydroxide is treated with water (2-3 g/30 mL of reaction solution) mixed with equal amount of DEG. The reaction of hydrolysis was performed at room temperature, and as the solution turned turbid, the capping agent (myristic acid) dissolved in methanol was added to stop the reaction. The precipitated nanoparticles contained cores with mixed metal hydroxides that were still partially ligated with DEG (this was evidenced by IR

1) Formation of metal-hydroxo complexes in diethylene glycol solutions.

a) Complex formation

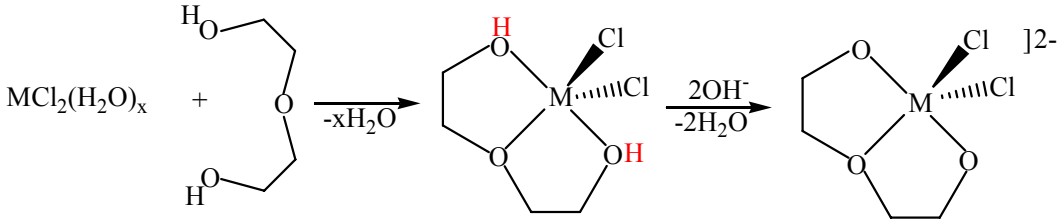

b) Hydrolysis of the metal alkoxide complex

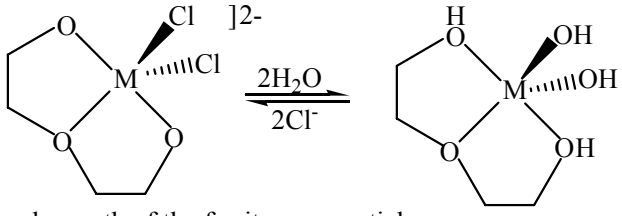

2) Nucleation and growth of the ferrite nanoparticles.

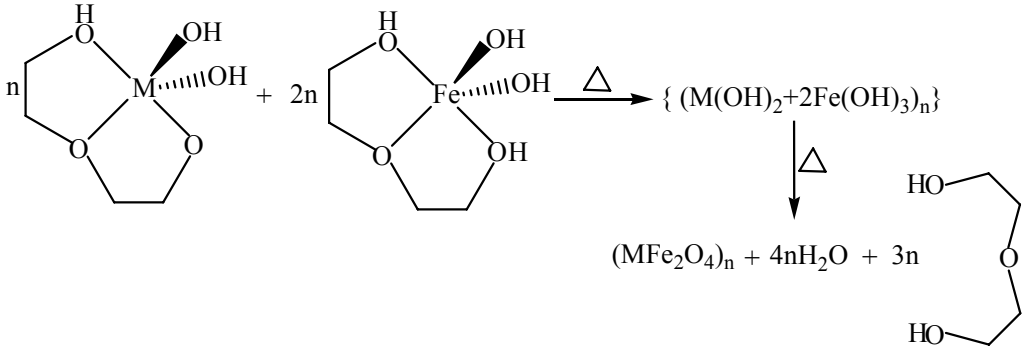

3) Passivation of the surface of ferrite nanoparticles.

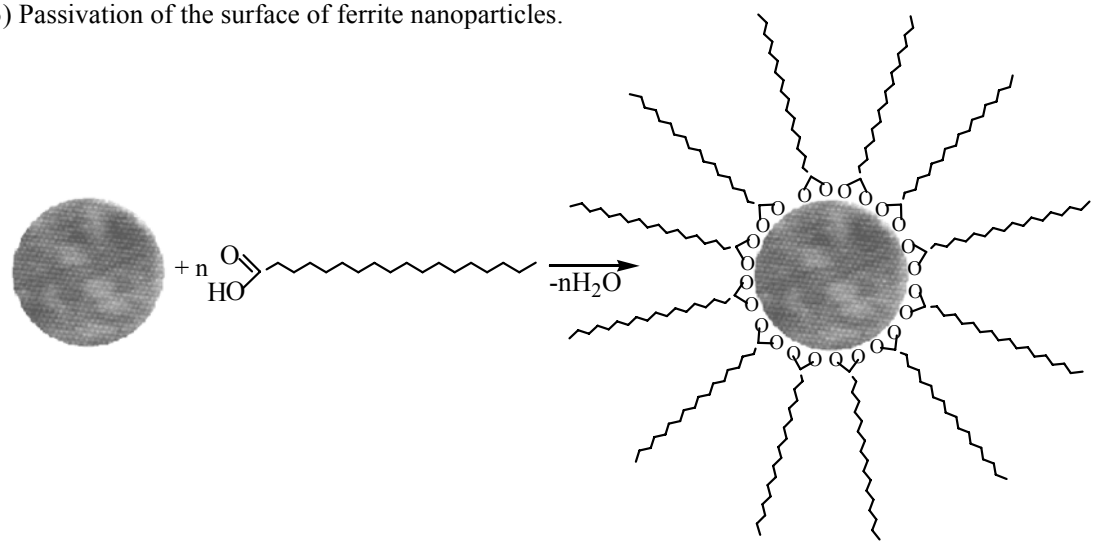

Scheme 2.1. Formation of ferrite nanoparticles in diethylene glycol solutions by elevated temperature method.

spectra) and had low crystallinity. To convert them into mixed-metal oxide nanoparticles, thermal treatment was necessary. For obtaining bulk metal oxides, corresponding powdered hydroxides usually undergo thermal treatment; dehydration is accompanied by crystallization. This conventional thermal dehydration could not be used in the synthesis of ferrite nanoparticles since the products loose their identity as nanocrystalline, and also they cannot be obtained as individual nanoparticles soluble in organic solvents. Since our raw products were colloidal hydroxides stabilized with long-chain carboxylates, they were soluble in different nonpolar solvents. This made possible to perform their dehydration and crystallization by thermal treatment in solutions of high-boiling low-polar solvents (Scheme 2.2). Phenyl ether (b.p. 259°) was found to be a good candidate as solvent, allowing the thermal treatment of the solutions in the temperature range 220-250°C. The resulting nanocrystalline products were stable against aggregation and remained in solution. To isolate them, 1-2 volumes of methanol were added to the solution at room temperature. The suspensions were centrifuged, and the solids were washed with methanol.

Ligand composition of the ferrite nanoparticles was identified using IR spectroscopy. Figure 2.1 shows the IR spectra of the intermediate product $ZnFe_2O_4$ containing DEG (a) and $ZnFe_2O_4$ nanoparticles capped with myristate anion and obtained by room temperature method (b). The IR spectrum of the intermediate product $ZnFe_2O_4$ shows strong bands at 3401.1 cm^{-1} and 1055.2 cm^{-1} corresponding to O-H and C-OH stretching vibrations, respectively. Strong bands are also observed at 2931 cm^{-1} and 2870.2 cm^{-1} which can be attributed to the asymmetric and symmetric stretches of the CH_2 group in diethylene glycol. The shoulder at 1119.9 cm^{-1} can be assigned to the

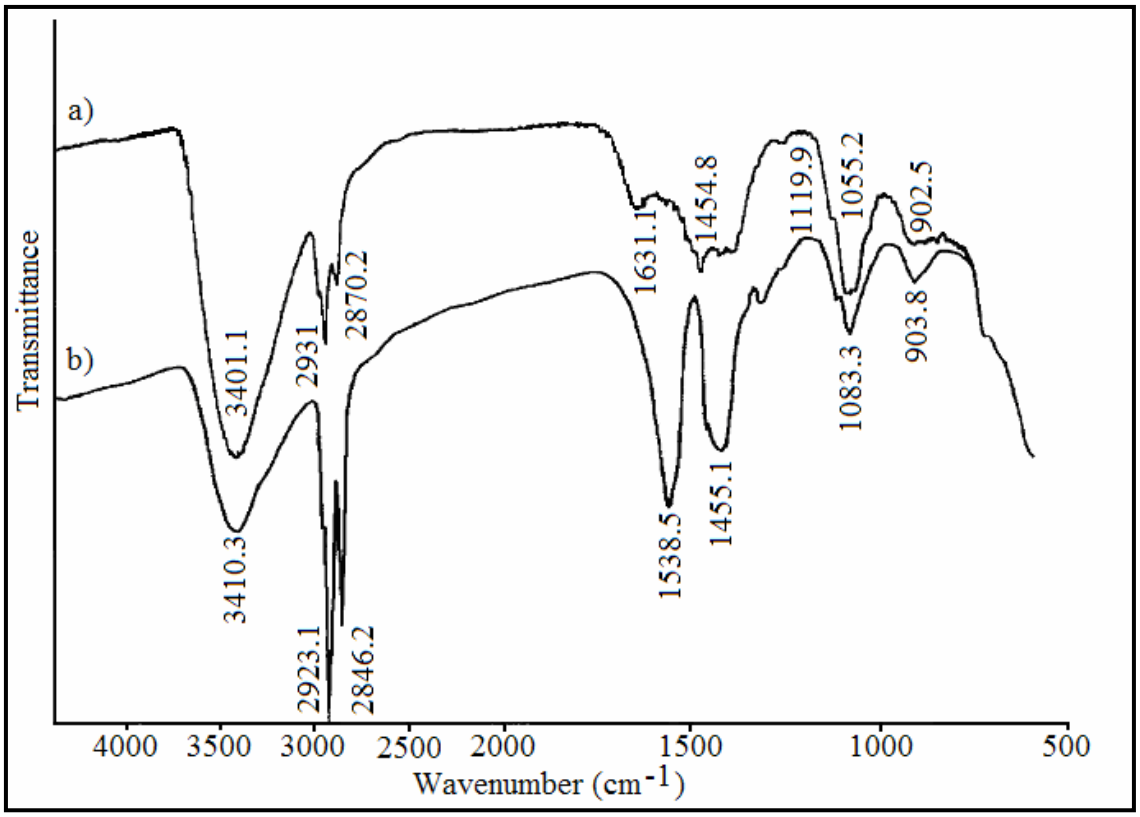

Figure 2.1. IR spectra of the intermediate product $ZnFe_2O_4$ containing diethylene glycol (a) and $ZnFe_2O_4$ nanoparticles capped with myristate anion and obtained by room temperature method (b).

$$\{M(OH)_2 + 2Fe(OH)_3\}_X[O_2CR]_Y \xrightarrow{\Delta} \{MFe_2O_4\}_X[O_2CR]_Y + 4XH_2O$$

Scheme 2.2. Dehydration of the mixed-metal hydroxide nanoparticles stabilized with long-chain carboxylate anions.

C-O-C stretching vibration. The IR spectrum also reveals a relatively weak absorption band at 1454.8 cm^{-1} corresponding to the symmetric bending mode of the methylene group. The band at 902.5 cm^{-1} was associated with a deformation mode of CH_2 group.

The second spectrum identifies long-chain carboxylate groups (strong band at 1538.5 cm^{-1} corresponding to asymmetric COO^- stretching mode and at 1455.1cm^{-1} assigned to symmetric COO^- stretching vibration)[28] as well as hydroxo groups of the residual DEG or metal hydroxides (broad band at 3410.3cm^{-1}). The two strong bands at 2923.1 cm^{-1} and 2846.2 cm^{-1} are due to asymmetric and symmetric CH_2 stretching modes, respectively.[29] The "fingerprints" region of both spectra closely resembles the spectra of free DEG and sodium myristate, respectively.

2.3.3. Synthesis of Ferrite Nanoparticles by the Elevated-Temperature Hydrolysis.

This method was applied for synthesis of Mn, Fe, Co, Ni, and Zn ferrites. The high boiling point of diethylene glycol (245°C) allowed performing the reactions of hydrolysis at elevated temperature. This modification of the process requires a smaller quantity of water present in solution; in the case of Mn^{2+}, Fe^{2+}, Co^{2+}, and Zn^{2+}, no water was added in addition to those few equivalents introduced together with metal salt hydrates. The reaction solutions containing stoichiometric quantities of metal salt hydrates and sodium hydroxide were heated to 190-220°C. As the solution turned turbid, the reaction was stopped by adding a DEG solution of capping ligand (oleic acid). This addition caused immediate decomposition of the colloid and precipitation of the product. After cooling, the product was isolated by centrifugation, washed with methanol, dissolved in toluene, and reprecipitated by adding methanol. Since the resulting nanoparticles were formed in

an anhydrous, highly crystalline form, the additional step of annealing in solution of high-boiling low-polar solvent was not necessary (Scheme 2.1).

The isolated yield of the nanopowders after air-drying was 75-90%; the yield was calculated after the metal oxide content was determined. The as-prepared ferrite nanopowders were highly soluble in toluene producing deep brown solutions that exhibited neither turbidity nor a Tyndall effect with a laser beam and were stable for indefinitely long time. These systems can be considered as colloidal in terms of size of the dispersed phase. On the other hand, they are stabilized similarly to molecular systems rather than colloidal with electric double layers. For this reason the term "solution" was used instead of term "dispersion".

TEM images for all ferrites obtained by elevated-temperature method are displayed in Figure 2.2 (a-e). As it follows from these images, the particles have spherical shape and size between 3 and 7 nm for different metal ferrites and are clearly deposited apart from each other. Corresponding histograms are displayed in Figure 2.3 (a-e). The data on mean particle size and calculated standard deviations for all metal ferrites (synthesized using both the room-temperature and elevated-temperature methods) are given in Table 2.1. Products obtained by elevated-temperature method are labeled as (A) and (B). The main difference between these products is in concentration of the reaction solutions. The overall concentration of metal cations in case of (A) was 0.075-0.15 m while in case of (B) it was 0.03-0.075 *m*. The presented data indicate that there is no clear relationship between the concentration of solutions and the size and size distribution of the obtained nanoparticles. High-resolution TEM images often exhibit crystal lattice, as it is evident for a nanoparticle of manganese ferrite shown in Figure 2.4.

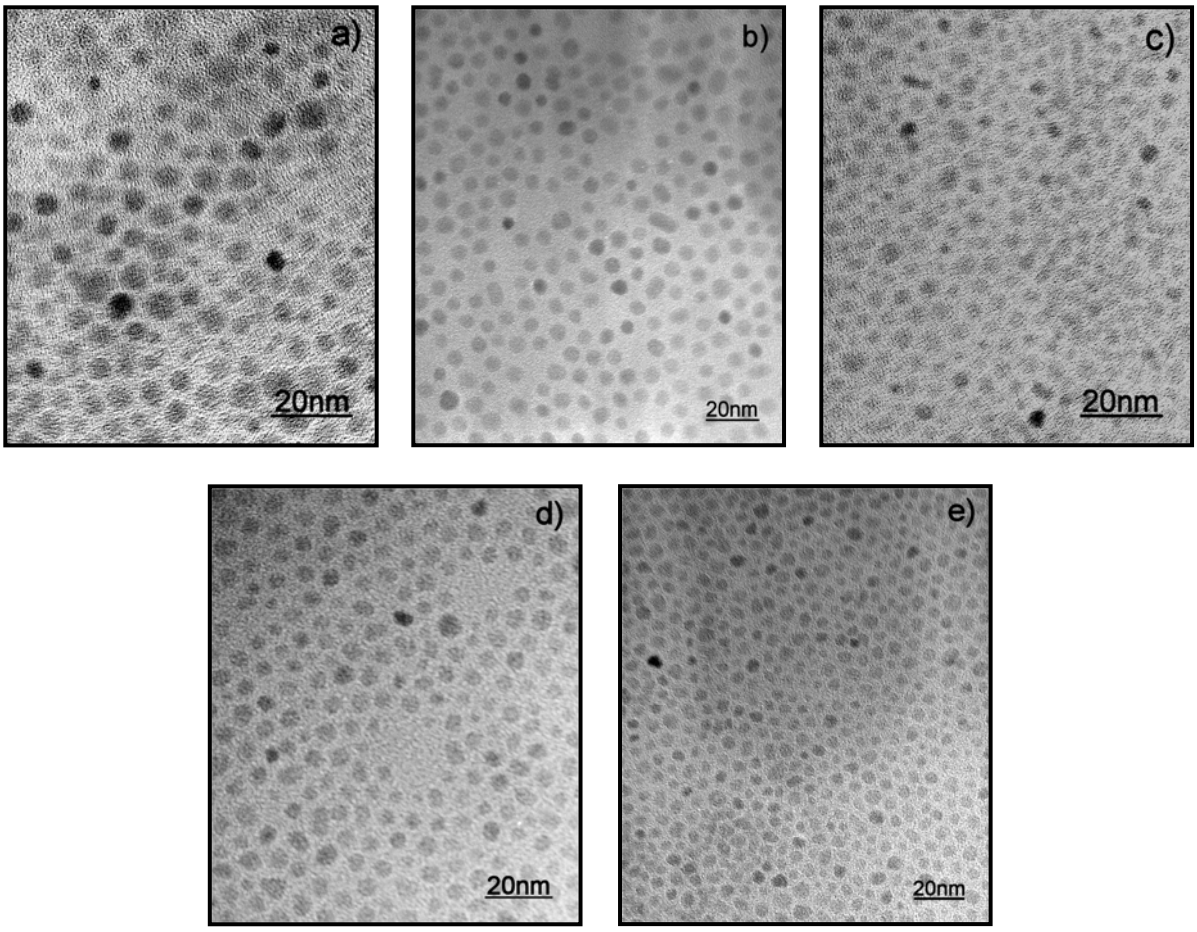

Figure 2.2. Bright field TEM images of $MnFe_2O_4$ (a), $FeFe_2O_4$ (b), $CoFe_2O_4$ (c), $NiFe_2O_4$ (d), and $ZnFe_2O_4$ (e); Fe ferrite was obtained using method (A), whereas Mn, Co, Ni, and Zn ferrites were synthesized using method (B).

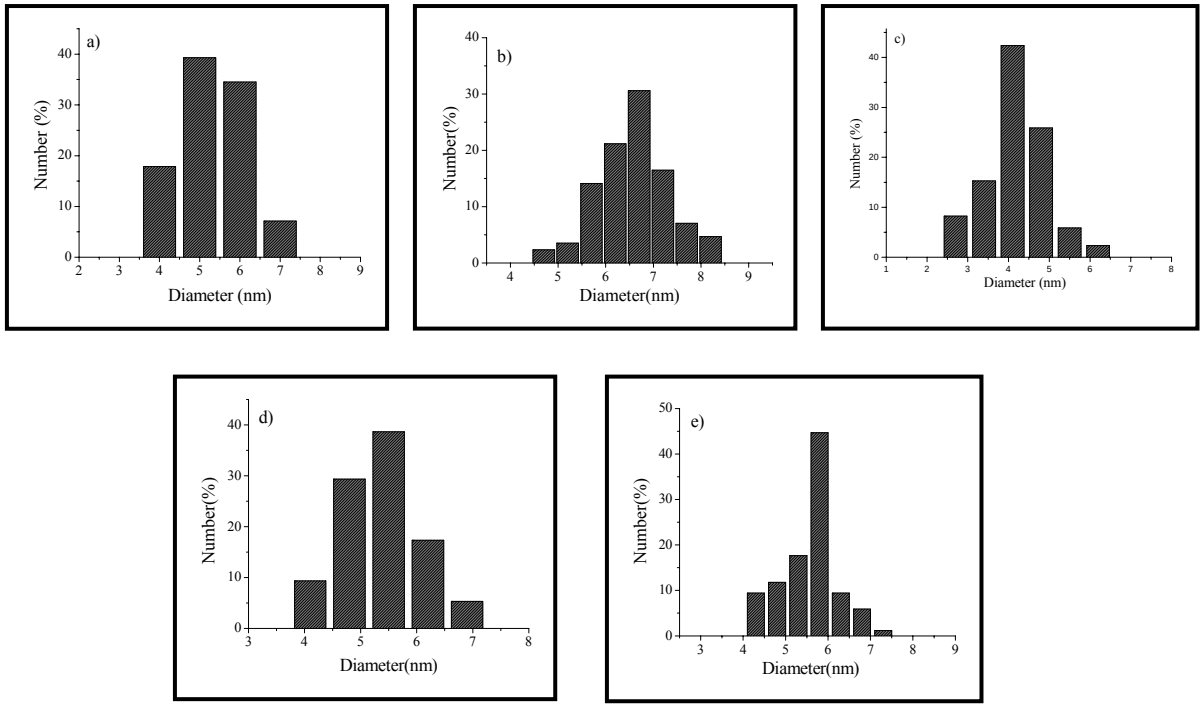

Figure 2.3. Particle size histograms of $MnFe_2O_4$ (a), $FeFe_2O_4$ (b), $CoFe_2O_4$ (c), $NiFe_2O_4$ (d), and $ZnFe_2O_4$(e); Fe ferrite was prepared using method (A), whereas Mn, Co, Ni, and Zn ferrites were synthesized using method (B).

Table 2.1. Size of the Transition Metal Ferrites Nanoparticles (Determined from TEM Images).

I) Obtained by Room-Temperature Method

Metal Ferrite	Mean Particle Size (nm)	Relative Standard Deviation (%)
$FeFe_2O_4$	4.2	18
$CoFe_2O_4$	4	*a*
$ZnFe_2O_4$	3	*a*

[a] Accurate measurements were not possible due to the lack of sharpness

II) Obtained by Elevated-Temperature Method

Metal Ferrite	Mean Particle Size (nm)	Relative Standard Deviation (%)
$MnFe_2O_4$ (method A)	6.6	28
$MnFe_2O_4$ (method B)	5.3	16
$FeFe_2O_4$ (A)	6.6	11
$CoFe_2O_4$ (A)	3.3	10.5
$CoFe_2O_4$ (B)	4.2	18
$NiFe_2O_4$ (A)	3.6	19
$NiFe_2O_4$ (B)	5.3	13.4
$ZnFe_2O_4$(A)	5.1	11
$ZnFe_2O_4$(B)	5.6	12

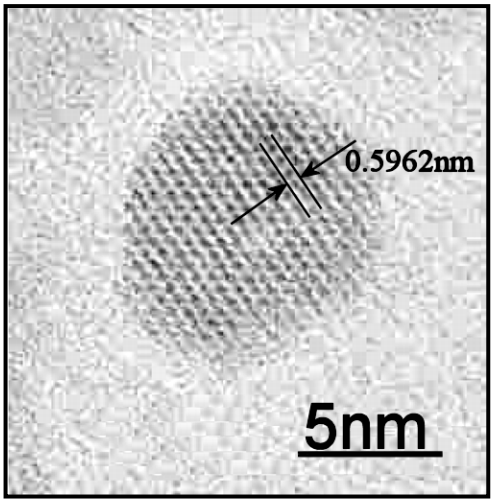

Figure 2.4. High-resolution TEM image of one particle of $MnFe_2O_4$

This micrograph reveals lattice fringes with a distance between two adjacent fringes of 0.5962 nm corresponding to {110} family of planes. This value leads to an estimated lattice parameter of 8.4326 Å, which is in a good agreement with that calculated from powder X-ray data (8.439(1) Å; Figure 2.5) and previously reported for bulk $MnFe_2O_4$ (8.499 Å; ASTM file No. 10-319).

The attempt to synthesize nanoparticles of γ-Fe_2O_3 using high-temperature method yielded nanopowder with poor crystallinity and solubility; no information about its particle size could be obtained. Phase composition was evaluated using powder X-ray diffractometry; in all cases the observed pattern corresponded to a crystal lattice with cubic symmetry. Diffractograms of all transition metal ferrites synthesized by the elevated-temperature method are displayed in Figure 2.5. The diffraction peaks are broadened due to the reduced size of the particles. The mean particle size was determined from the full width at half maximum (FWHM) of the three most intense peaks by using the Scherrer`s equation. Calculation of a particle size for $ZnFe_2O_4$ using peak broadening gave the result of 4.95 nm, while the TEM experiment gave the value of 5.60 nm.

In order to determine the metal oxide content of the as-prepared transition metal ferrite nanopowders, a quantitative analysis using a combustion method was performed. Sintering under open air at 400-600°C caused their complete deligation and aggregation with formation of larger crystallites; diffractograms of both nanopowder and sintered $ZnFe_2O_4$ are displayed in Figure 2.6. The residual after sintering nanopowders have been analyzed (Galbraith Laboratories, Inc.) to determine their metal ratio; the results are presented in the Table 2.2.

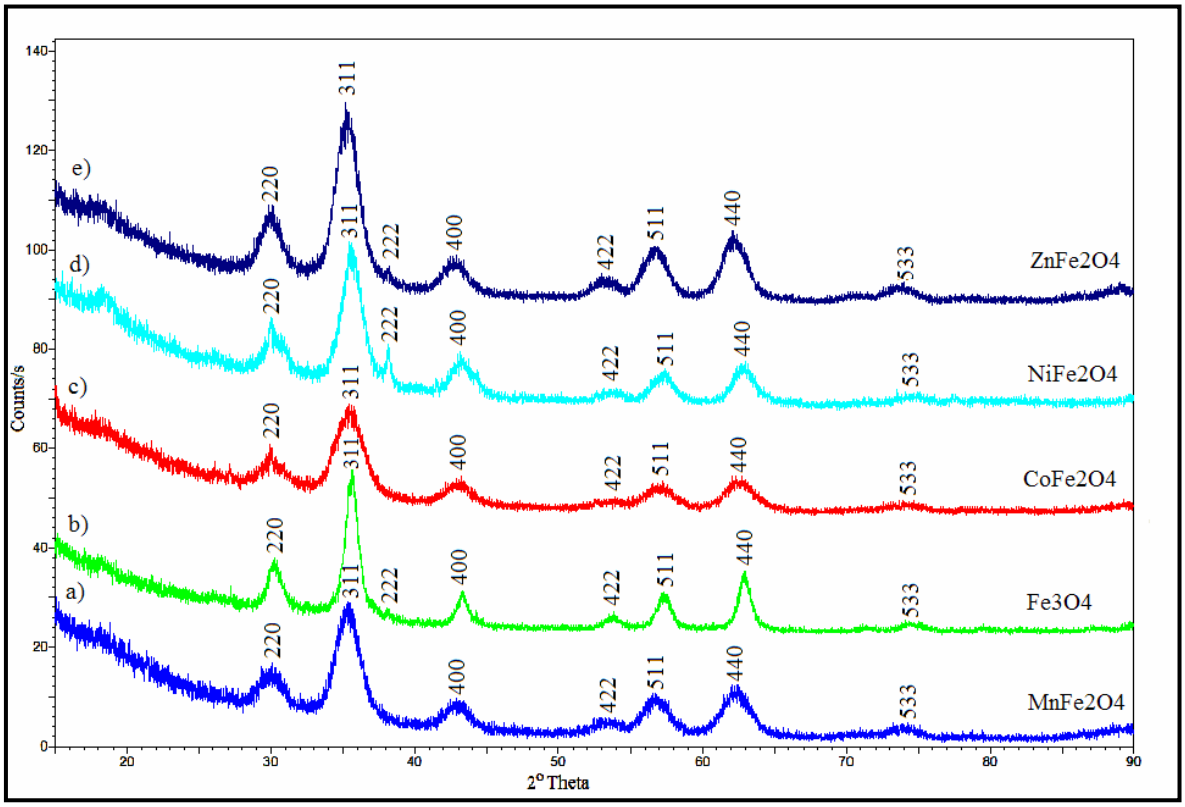

Figure 2.5. Typical powder X-ray diffractograms of $MnFe_2O_4$ (a), $FeFe_2O_4$ (b), $CoFe_2O_4$ (c), $NiFe_2O_4$ (d), and $ZnFe_2O_4$ (e); Fe ferrite was prepared using method (A), whereas Mn, Co, Ni, and Zn ferrites were synthesized using method (B).

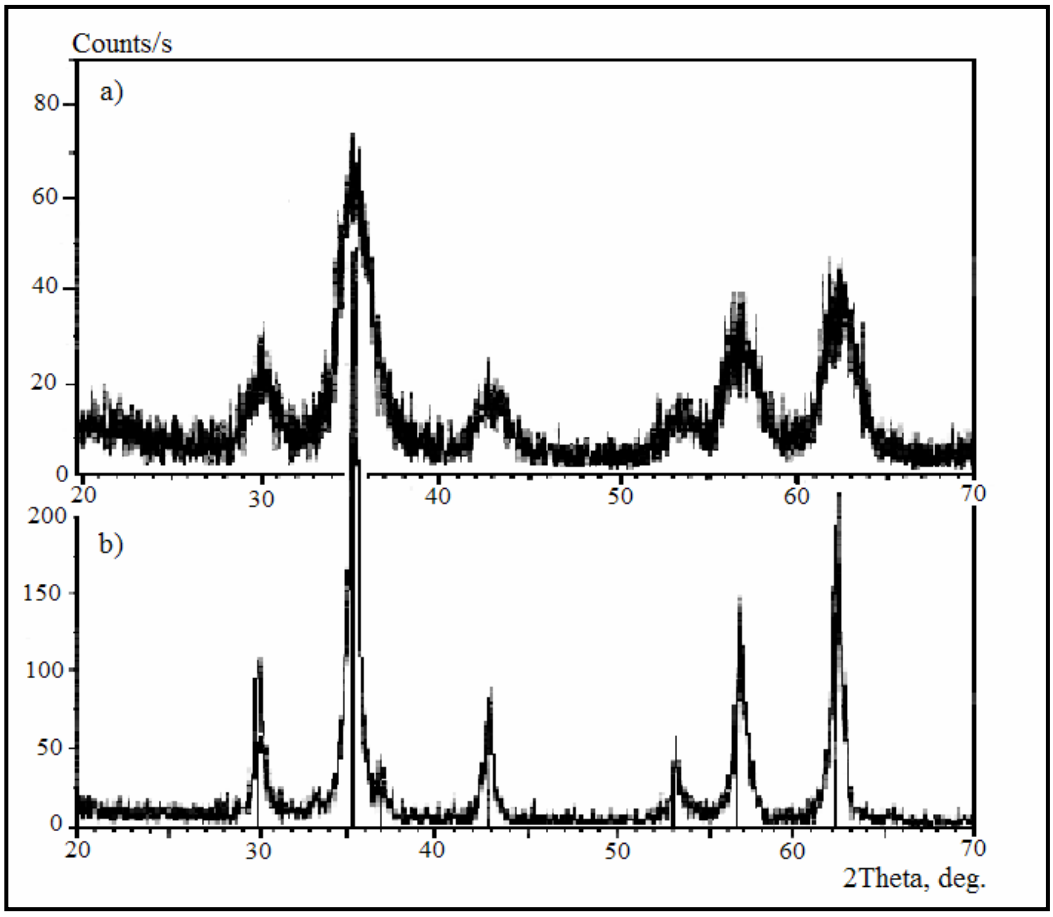

Figure 2.6. Powder X-ray diffractograms of 5.1 nm-sized $ZnFe_2O_4$ particles obtained by the elevated-temperature method (a) and bulk material obtained by sintering of the nanopowder (b).

Table 2.2. Results of Quantitative Analysis of the Obtained Nanocrystalline Ferrites

I) By room-temperature hydrolysis method

Metal ferrite	Metal oxide content (wt %)	Metal content in sintered samples (wt %)	Ratio of metals, Fe : M (M = Co, Zn)
$FeFe_2O_4$	73.9	-	N/A
$CoFe_2O_4$	48.7	Fe (51.43); Co (19.41)	2.80
$ZnFe_2O_4$	47.2	Fe (48.95); Zn (22.68)	2.53

II) By elevated-temperature hydrolysis method

Metal ferrite	Metal oxide content (wt %)	Metal content in sintered samples (wt %)	Ratio of metals, Fe : M (M = Mn, Co, Ni Zn)
$MnFe_2O_4$	78.4	Fe (54.16); Mn (21.03)	2.53
$FeFe_2O_4$	76.4	-	N/A
$CoFe_2O_4$	61.4	Fe (50.69); Co (24.30)	2.20
$NiFe_2O_4$	69.6	Fe (49.19); Ni (26.09)	1.98
$ZnFe_2O_4$	65.2	Fe (52.43); Zn (24.81)	2.47

Analytical and TEM data indicate that both room-temperature and elevated-temperature synthetic methods gave good results for iron ferrite, while, in the case of cobalt and zinc ferrites, the latter method gave products of a better quality. On the basis of the obtained metal oxide content data for the sample of $CoFe_2O_4$, a molar ratio of $CoFe_2O_4$ to oleate anion was found to be 1.905:1. This corresponds to a fraction of metal atoms bearing an oleate anion of 0.175. Evidently, these atoms are located on the surface of nanocrystals. The following steps were used to calculate the percent coverage of the surface metal atoms with oleate ligands.[30] A particle diameter of 3 nm determined by TEM was used to calculate its volume. This value and a bulk density of 5.2 g/cm^3 were used to calculate the nanoparticle mass, the number of moles, the number of $CoFe_2O_4$ formula units, and finally the number of metal atoms/particle. Similar calculations were performed for a hypothetical particle derived from the original particle with a radius of 1.5 nm minus the surface atomic layer estimated as an average M-O distance of 1.95 Å. The number of metal atoms on the surface of nanoparticles was calculated by subtracting the second value from first. Finally, the fraction of these atoms over total number of metal atoms was found to be 0.34. A similar result (0.365) was obtained by using the formula $F = 4/n^{1/3}$, where F is the fraction of the surface atoms and n is the total number of atoms.[31] As it was shown above, the fraction of metal atoms bearing oleate anion was 0.175, which is ~50% of all surface metal atoms. It is possible that every carboxylate anion acts as a bidentate bridging ligand that coordinates to two adjacent metal atoms.

2.4 Conclusion

A new method for synthesis of nanocrystalline transition metal ferrites with structure of discrete nanoparticles stabilized with carboxylate capping ligands was developed. Nanoparticles of Mn, Fe, Co, Ni, and Zn ferrites with a diameter of 3-7 nm and an isolated yield 75-90% were obtained. Since the surface of the nanoparticles is capped with long-chain carboxylate anions, they are soluble in non-polar solvents forming solutions which are stable for long periods of time. The obtained products were characterized with TEM imaging, elemental analysis, IR spectroscopy, and X-ray diffractometry. We believe this method can be used for the synthesis of other types of nanocrystalline metal oxides.

2.5. References

1. Kryder, M. H. *MRS Bull*. **1996**, *21* (9), 17.
2. Raj, K.; Moskowitz, R.; Casciari, R. *J. Magn. Magn. Mater*. **1995**, *149*, 174.
3. Häfeli, U., Schütt, W., Teller, J., Zborowski, M., *Eds. Scientific and Clinical Applications of Magnetic Carriers*; Plenum: New York, 1997.
4. Mitchell, D. G. *Magn. Reson. Imaging* **1997,** *7*, 1.
5. Ziolo, R., *US Patent*, 1984.
6. Nishinozono, I.; Iida, S.; Suzuki, N.; Kawada, H.; Murakami, H.; Ashihara, Y.; Okada, M. *Clin. Chem.* **1991**, *37*, 1639.
7. Miyawaki, F.; Ysuji, T.; Abe, M.; Kaibara, M. *Proc. XIII World Congress of Cardiology*; Rio de Janeiro, Brazil, 1998; 1133.
8. Moumen, N.; Pileni, M. P. *J. Phys. Chem*. **1996**, *100*, 1867.
9. Ngo, A. T.; Pileni, M. P. *J. Phys. Chem. B.* **2001,** *105*, 53.
10. Liu, C.; Zou, B.; Rondinone, A. J.; Zhang, Z. J. *J. Am. Chem. Soc.* **2000,** *122*, 6263.
11. Liu, C.; Zou, B.; Rondinone, A. J.; Zhang, Z. J. *J. Phys. Chem. B* **2000,** *104*, 1141.
12. Moumen, N. ; Veillet, P. ; Pileni, M. P. *J. Magn. Magn. Mater*. **1995**, *149*, 67.
13. Seip, C. T.; Carpenter, E. E.; O`Connor, C.J.; *IEEE Trans. Magn*., **1998**, 34(*4*), 1111.
14. Sun, S.; Murray, C. B. *J. Appl. Phys*. **1999**, *85* (8), 4325.
15. Petit, C.; Taleb, A.; Pileni, M. P. *Ad*v. *Mater*. **1998**, *10* (3), 259261.
16. Petit, C.; Taleb, A.; Pileni, M. P. *J. Phys. Chem. B* **1999**, *103*, 1805.
17. Alivisatos, A. P. *J. Phys. Chem*. **1996,** *100*, 13226.
18. Alivisatos, A. P. *Pure. Appl. Chem*. **2000**, *72*, 3.

19. Weller, H.*J. Colloid Interface Sci.* **1998**, *3*, 194.

20. Brus, L. *J. Phys. Chem. Solids* **1998**, *59* (4), 459.

21. Pileni, M. P. *J. Phys. Chem. B* **2001,** *105*, 3358.

22. Murray, C. B.; Kagan, C. R.; Bawendi, M. G. *Annu. Rev. Mater. Sci.* **2000**, *30*, 545.

23. Wong, E. M.; Hoertz, P. G.; Liang, C. J.; Shi, B.-M.; Meyer, G. J.; Searson, P. C. *Langmuir* **2001,** *17* (26), 8362.

24. Thimmaiah, S.; Rajamathi, M.; Singh, N.; Bera, P.; Meldrum, F.; Chandrasekhar, N.; Seshadri, R. *J. Mater. Chem.* **2001**, *11,* 3215.

25. Hyeon, T.; Lee, S. S.; Park, J.; Chung, Y.; Na, H. B. *J. Am. Chem. Soc*. **2001**, *123,* 12798.

26. Rockenberger, J.; Scher, E. C.; Alivisatos, A. P. *J. Am. Chem. Soc*. **1999,** *121*, 11595.

27. Jezequel, D.; Guenot, J.; Jouini, N.; Fievet, F. *Mater. Sci. Forum* **1994**, *152-153*, 339.

28. Wong, E. M.; Hoertz, P. G.; Liang, C.J.; Shi, B.M.; Meyer, G.J.; Searson, P.C. *Langmuir* **2001**, *17*(26), 8362.

29. Szymanski, H. A.; *Interpreted Infrared Spectra*; Plenum Press, New York, **1996.**

30. Bowen Katari, J. E.; Colvin, V. L.; Alivisatos, A. P. *J. Phys. Chem.* **1994**, *98*, 4109.

31. Edelstein, A. S.; Cammarata, R. C. *Nanomaterials: Synthesis, Properties and Applications*; Institute of Physics Publishing: Bristol, U.K., Philadelphia, PA, 1998; p26.

CHAPTER 3

Synthesis of variable-sized nanocrystals of Fe_3O_4 with high surface reactivity

3.1. Introduction

Nanocrystalline metal oxides are generally synthesized by a variety of methods based on relatively simple chemical reactions yielding products with desired composition, purity and crystal structure. Obtaining the nanocrystals with variable and uniform size is a significant challenge however because controlling the crystal growth in all its steps is not easy to accomplish. Many common methods are rooted in the ion metathesis reactions in solution. These straightforward reactions provide good yield and purity of the products, but they occur instantly on mixing and leave little possibility to control the course of the crystallization. Different techniques were developed in order to address this problem. According to one of them, ion metathesis reactions are performed under strictly controlled conditions of mixing, such as addition of the dilute reactant solutions at a restricted rate with vigorous stirring and maintaining the proper temperature.[1-9] The nanocrystal growth is controlled also by performing metathesis reactions in heterogeneous media of microemulsions where aqueous micelles of variable sizes act as microreactors.[10-15] In a third method, the precipitating agent (OH^-) is slowly generated in aqueous solution by hydrolysis of a molecular precursor (urea, urotropin, *etc*.).[16-18] The greatest advantage of these techniques is that the surface of the produced nanocrystals remains active and available for post-synthesis chemical modification.

Other methods use the nucleophilic property of water in hydrolysis of metal precursors. Reactions usually are slower than ion metathesis reactions and therefore crystallization is easier to control. Hydrolysable salts of metal ions are used for synthesis of corresponding oxides in colloidal form by their forced hydrolysis under hydrothermal conditions[19-21] or in a high-boiling solvents.[22, 23] Hydrolysis in non-aqueous solutions has been applied also to metal alkoxides[24, 25] and β-diketonates,[26-29] offering a convenient route to the uncapped nanoparticles.

A different synthetic approach replaces the hydrolysis or ion metathesis reactions by thermal decomposition of oxygen-rich molecular precursors or metal carbonyls in the presence of oxygen or oxygen donors in solutions of high-boiling nonpolar solvents.[30-38] This technique offers a convenient way to manipulate the kinetics of crystallization and therefore the nanocrystal dispersity. The thermal decomposition technique is usually used in conjunction with tactical targeting control over composition of the surface of growing nanocrystals. The synthesis reactions are performed in the presence of complexing agents that reversibly bind to the coordinatively unsaturated metal atoms at the crystal surface. These complexing agents (capping ligands) contain one or more substituents that provide steric separation between nanocrystals and adjust their affinity to the medium, stabilizing their colloids. Capping ligands[39-42] and coordinating polymers[43-45] are sometimes used also to passivate the nanocrystal surface in combination with hydrolytic and ion metathesis methods.

In this chapter we describe a new method that allows the scaled preparation of uncapped nanocrystalline metal oxides with variable size and composition and high crystallinity. The method is based on the reaction between chelate metal alkoxide

complexes and water at elevated temperature in solutions of the parent chelating alcohols. The isolated uncapped nanocrystals retain a chemically active surface that is available for further derivatization. Nanocrystals in this state are capable of forming stable aqueous colloids without using capping ligands or surfactants. The developed method represents a highly economical and facile "green" process that can be used for scaled preparations. This method may contribute to the development of new catalysts, functional magnetic and optoelectronic materials and biocompatible magnetic materials for their application in biology and medicine as diagnostic and therapeutic tools.

3.2. Experimental

3.2.1. Chemicals. The reagents and solvents were purchased from the following companies: Iron(III) chloride hexahydrate 97%, toluene 99.5%, methyl alcohol 99.8%, and hexanes 98.5% from Merck; diethylene glycol 99%, N-methyl diethanolamine 99+%, sodium hydroxide 97% (20-40 mesh beads), ethyl acetate 99.5%, and decane 99+% from Aldrich; iron(II) chloride tetrahydrate 99% from Alfa Aesar; oleic acid 90% from Fisher; and absolute ethyl alcohol from AAper Alcohol and Chemical Co. Chemicals and solvents were used without further purification. The air-sensitive chemicals were manipulated in a VAC glovebox with a nitrogen atmosphere.

3.2.2. Synthesis. All syntheses were carried out using Schlenk technique under argon atmosphere.

3.2.2.1. Preparation of magnetite nanoparticles in diethylene glycol solutions. A 2 mmol amount of $FeCl_2 \cdot 4H_2O$ and 4 mmol $FeCl_3 \cdot 6H_2O$ were dissolved in 80 g of diethylene glycol (DEG) in a Schlenk flask under protection with argon. Separately, 16

mmol of NaOH was dissolved in 40 g of diethylene glycol. The solution of NaOH was added to the solution of metal chlorides with stirring at room temperature causing an immediate color change from yellow-brown to deep green-brown. After 3 hours, the temperature of solution was raised during 1.5 h to 210^{o}C and then kept constant for 2 h in the temperature range 210-220°C. The solid product was isolated by cooling the reaction mixture to room temperature and centrifuging. A black solid was obtained and washed with ethanol twice and with a mixture of ethanol and ethyl acetate (1:1, v/v) three times to remove the excess of diethylene glycol and dried in a flow of nitrogen. The typical yield was 95-96%. When reactivity tests or the preparation of colloids were planned, the solids were used without drying.

In order to obtain iron oxide nanoparticles soluble in nonpolar solvents, a diethylene glycol solution of oleic acid (2.6 mmol oleic acid per 20 g DEG) was added to the reaction mixture at high temperature. This addition immediately precipitated the solids. The mixture was cooled to room temperature and then centrifuged. The precipitates were washed with methanol and dissolved in 20 ml toluene. The resulting solution was centrifuged and mixed with 2-3 volumes of methanol. The precipitate was separated by centrifuging, washed with methanol and kept either moistened with methanol or dispersed in nonpolar solvents (hexanes, toluene, and decane).

3.2.2.2. Preparation of magnetite nanoparticles in a mixture of diethylene glycol and N-methyl diethanolamine (3:1, w/w). A 2 mmol amount of $FeCl_2 \cdot 4H_2O$ and 4 mmol $FeCl_3 \cdot 6H_2O$ were dissolved in 60 g of diethylene glycol (DEG) in a Schlenk flask under argon. When the salts were completely dissolved, 20 g of N-methyl diethanolamine (NMDEA) was added and the solution immediately turned from yellow-brown to deep

brown-green. The resulting solution was stirred for 1 h at room temperature. Separately, 16 mmol of NaOH was dissolved in 30 g of diethylene glycol and then mixed with 10 g N-methyl diethanolamine. The solution of NaOH was added to the solution of metal chlorides with stirring at room temperature causing an immediate color change from deep brown-green to deep green. After 3 h, the temperature of solution was raised during 1.5 h to 210°C and then kept constant for 3 h in the temperature range 210-220°C. After cooling, the solid product was isolated by centrifuging, washing with ethanol twice and with a mixture of ethanol and ethyl acetate (1:1, v/v) three times and drying in a flow of nitrogen.

Magnetite nanoparticles soluble in nonpolar solvents were obtained by heating to reflux for 0.5-1 h a mixture containing 165 mg of black powder and a toluene solution of oleic acid (0.89 mmol oleic acid per 50 ml toluene). A deep brown solution was obtained and the solid product was re-precipitated by adding 1-2 volumes of methanol and then washed several times with methanol to remove the excess of oleic acid. The precipitate was kept either moistened with methanol or dispersed in nonpolar solvents (hexanes, toluene, and decane).

3.2.2.3. Preparation of magnetite nanoparticles in a mixture of diethylene glycol and N-methyl diethanolamine (1:1, w/w). A 2 mmol amount of $FeCl_2 \cdot 4H_2O$ and 4 mmol $FeCl_3 \cdot 6H_2O$ were dissolved in 40 g of diethylene glycol (DEG) in a Schlenk flask under argon. When the salts were completely dissolved, 40 g of N-methyl diethanolamine (NMDEA) was added and the solution immediately turned from yellow-brown to deep brown-green. The resulting solution was stirred for 1 h at room temperature. Separately, 16 mmol of NaOH was dissolved in 20 g of diethylene glycol and then mixed with 20 g

N-methyl diethanolamine. The solution of NaOH was added to the solution of metal chlorides with stirring at room temperature causing an immediate color change from deep brown-green to deep green. After 3 h, the temperature of solution was raised during 1.5 h to 210 °C and then kept constant for 3 h in the temperature range 210-220 °C. After cooling, the solid product was isolated by centrifuging, washing with ethanol twice and with a mixture of ethanol and ethyl acetate (1:1, v/v) three times and drying in a flow of nitrogen. The typical isolated yield of black powders was 80-90 % (for products containing 96-97 % of metal oxide).

Magnetite nanoparticles soluble in nonpolar solvents were obtained by heating to reflux for 0.5-1 h a mixture containing 80 mg of black powder and a toluene solution of oleic acid (0.5 mmol oleic acid per 25ml toluene). A deep brown solution was obtained and the solid product was re-precipitated by adding 1-2 volumes of methanol and then washed several times with methanol to remove the excess of oleic acid. The precipitate was kept either moistened with methanol or dispersed in nonpolar solvents (hexanes, toluene, and decane).

3.2.2.4. Preparation of magnetite nanoparticles in a mixture of diethylene glycol and N-methyl diethanolamine (1:3, w/w). A 2 mmol amount of $FeCl_2 \cdot 4H_2O$ and 4 mmol $FeCl_3 \cdot 6H_2O$ were dissolved in 20 g of diethylene glycol (DEG) in a Schlenk flask under argon. When the salts were completely dissolved, 60 g of N-methyl diethanolamine (NMDEA) was added and the solution immediately turned from yellow-brown to deep brown-green. The resulting solution was stirred for 1 h at room temperature. Separately, 16 mmol of NaOH was dissolved in 10 g of diethylene glycol and then mixed with 30 g N-methyl diethanolamine. The solution of NaOH was added to the solution of metal

chlorides with stirring at room temperature causing an immediate color change from deep brown-green to deep green. After 3 h, the temperature of solution was raised during 1.5 h to 210 °C and then kept constant for 4 h in the temperature range 210-220 °C. After cooling, the solid product was isolated by centrifuging, washing with ethanol twice and with a mixture of ethanol and ethyl acetate (1:1, v/v) three times and drying in a flow of nitrogen.

Magnetite nanoparticles soluble in nonpolar solvents were obtained by heating to reflux for 0.5-1 h a mixture containing 120 mg of black powder and a toluene solution of oleic acid (0.64 mmol oleic acid per 25 ml toluene). A deep brown solution was obtained and the solid product was re-precipitated by adding 1-2 volumes of methanol and then washed several times with methanol to remove the excess of oleic acid. The precipitate was kept either moistened with methanol or dispersed in nonpolar solvents (hexanes, toluene, and decane).

3.2.2.5. Preparation of magnetite nanoparticles in N-methyl diethanolamine solutions. A 2 mmol amount of $FeCl_2 \cdot 4H_2O$ and 4 mmol $FeCl_3 \cdot 6H_2O$ were dissolved in 40g of N-methyl diethanolamine (NMDEA) in a Schlenk flask under protection of argon. Separately, 16 mmol of NaOH was dissolved in 40 g of N-methyl diethanolamine. Then, a solution of NaOH was added to solution of metal chlorides while stirring at room temperature causing an immediate color change from deep brown to deep green. After 3 h, the temperature of solution was raised during 1.5 h to 210 °C and then kept constant for 4 h in the temperature range 210-220 °C. The solid product was isolated by cooling the reaction mixture to room temperature and then centrifuging. A black solid was obtained and washed with ethanol twice and with a mixture of ethanol and ethyl acetate

(1:1, v/v) three times and dried in a flow of nitrogen. The yield of black powder was 0.294 g (63%).

3.2.3. Characterization. The structure and phase purity of the nanopowders were investigated by X-ray diffractometry (XRD). The measurements were performed with a Phillips X`pert system equipped with a graphite monochromator (CuK_α radiation, λ=1.54056 Å). A JEOL JEM 2010 transmission electron microscope (TEM) at an accelerating voltage of 200 kV was used to examine the particles morphology. Additionally, high-resolution transmission electron microscopy (HRTEM) images and selected area electron diffraction (SAED) patterns were taken in order to determine the nanocrystal structure. Thermogravimetric analyses (TGA) were performed in both air and argon at a heating rate of 2 °C/min up to 600 °C using a SDTQ600 analyzer. The NMR studies were performed on a Varian Gemini-300 spectrometer. FT-IR spectra were obtained on a Perkin-Elmer 1600 spectrometer.

3.3 Results and Discussion

In our earlier studies on the synthesis of nanocrystalline spinel-structured oxides, we have found that diethylene glycol is a convenient reaction medium[46] due to its useful physical and chemical properties.[47] The high boiling point (245^{o}C) of this solvent makes it suitable for variable-temperature syntheses, which is desirable for controlling the rate of reaction and also for obtaining products with improved crystallinity. Diethylene glycol has high permittivity (ε = 32), enabling it to dissolve highly polar inorganic and a variety of organic compounds and also to promote reactions whose pathways run through highly polar or ionic intermediates.

As we found previously, the chelating ability of DEG inhibits the formation of metal hydroxides/oxides in solutions containing stoichiometric quantities of transition metal salts and sodium hydroxide.[46] Introduction of a controlled amount of water in these solutions causes hydrolysis of chelated complexes with formation of metal oxides or hydroxides depending on the temperature, with nearly quantitative yield. The structure of complexes existing in solution is not known, but there is evidence that the metal ion coordination sphere contains deprotonated DEG and Cl^- ligands (Scheme 3.1). The rate of this reaction can be easily controlled by changing the concentration of water and temperature. The course of reaction is monitored visually and as the solution turns turbid, the reaction is considered to be complete.

In our earlier studies, we next added long-chain carboxylic acids to cap the surface of nanoparticles and isolated them as nanopowders. A series of transition metal ferrites $(MO)_xFe_2O_3$ (M = Mn, Fe, Co, Ni and Zn; x = 0.7-1) was obtained.[46] In the current study we addressed the problem of tuning the particle size and the details of the surface chemistry of the nanocrystalline oxides. We focused exclusively on iron ferrite (magnetite) while keeping in mind that our results should apply also to other transition metal ferrites.

3.3.1. Synthesis. In order to obtain non-aggregated nanoparticles with a chemically active surface, we eliminated the step of capping the nanoparticles with the long-chain carboxylic acid. As a stoichiometric quantity of NaOH (8 equivalents) dissolved in DEG is added to the solution containing 1 equivalent of $FeCl_2 \cdot 4H_2O$ and 2 equivalents of $FeCl_3 \cdot 6H_2O$ dissolved in the same solvent, an immediate color change from yellow-brown to deep green-brown occurs. We explained this[46] in terms of deprotonation of the

coordinated alcohol DEG and formation of anionic chelate alkoxide complex (Scheme 3.1). The resulting solution stays unchanged indefinitely at room temperature if protected from air, but gets oxidized quickly if exposed to air and turns deep yellow. Raising the temperature to 150^{o}C and then to 210-220^{o}C causes gradual color change to red-brown and then dark brown with increasing turbidity. As this temperature is maintained for 2 hours, a black suspension forms and heating is stopped. After a simple workup procedure using ethanol and ethyl acetate, the nanopowders are isolated with high yield and tested for their crystal structure and morphology and for reactivity. We performed a series of synthetic experiments varying the rate and time of heating and concentration of the reagents and found no significant difference in the nanocrystals' shape and size with an average value of 5.7 nm (Figures 3.2a and 3.3a). If the step of aging is shortened to less than 1 hour, the quality of the nanocrystals is low, no lattice fringes can be seen, and the edges are diffuse. Our attempts to obtain larger particles by injecting an additional quantity of the reaction solution in the hot solution of the seed nanoparticles yielded a product with wider size distribution. This result indicated that nucleation and growth occurred with a similar rate.

The results show that under various conditions the particle morphology did not change significantly and prompted us to increase the complexing strength of the reaction medium. Such a change might provide a better control over the rate of hydrolysis of metal chelates, help to stabilize colloids, and therefore obtain larger nanocrystals. The thermal decomposition of triethanolamine-based chelate complexes of iron, cobalt and nickel in aqueous solution at 250^{o}C (hydrothermal synthesis) has been used to synthesize corresponding oxides as micrometer-sized crystals.[48, 49] We chose to use diethanolamine,

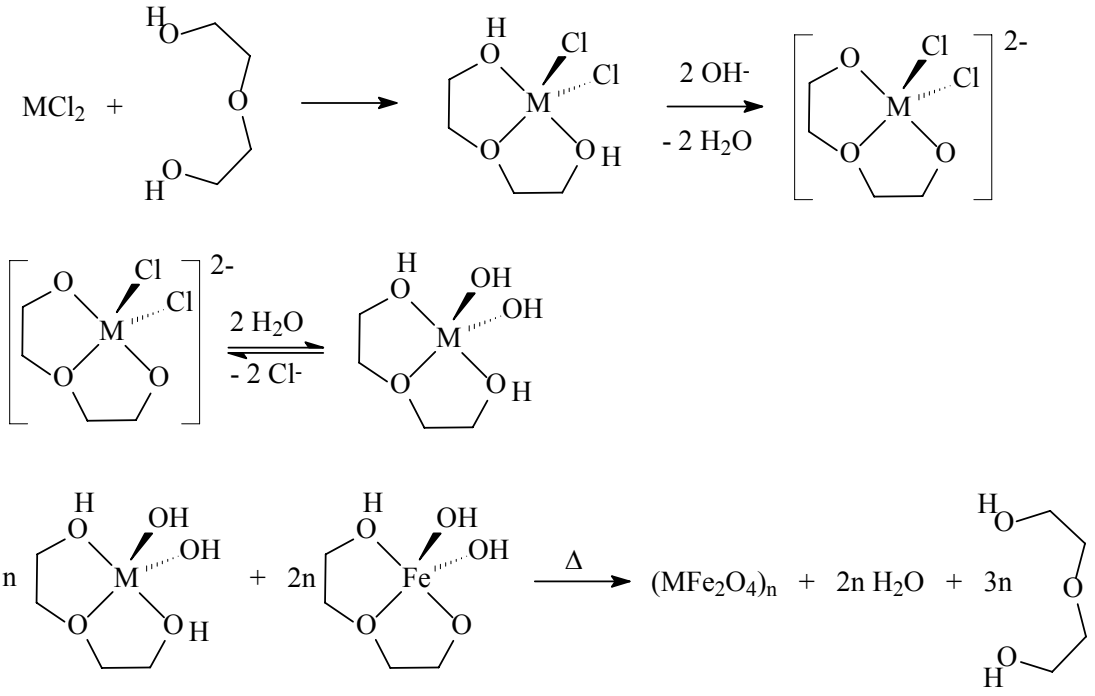

Scheme 3.1. Formation of metal chelate complex and its decomposition yielding colloidal transition metal ferrite.

a compound related to both triethanolamine and DEG and whose complexing and chelating properties are well-established.[50-53] Because diethanolamine (DEA) has hydrogen bonding more extended than DEG, its physical properties are substantially different, and it has higher viscosity and boiling point. N-methyl diethanolamine (NMDEA), on the other hand, has physical properties similar to those of DEG but complexing properties similar to diethanolamine. We performed a series of syntheses of nanocrystalline magnetite in neat NMDEA and in its 3:1, 1:1, and 1:3 mixtures with DEG while keeping all other parameters unchanged. Magnetite nanocrystals were also prepared from a 1:1 mixture of DEG and DEA and the results were compared with those obtained when NMDEA is used as a chelating solvent instead of DEA.

As a stoichiometric quantity of NaOH (8 equivalents) dissolved in 1:1 DEG/NMDEA solvent mixture is added to a solution containing 1 equivalent of $FeCl_2 \cdot 4H_2O$ and 2 equivalents of $FeCl_3 \cdot 6H_2O$ dissolved in the same solvent, the color changes from brown-green to green immediately. Upon heating, the solution becomes dark green-brown at 180-190°C and then the color gradually changes to dark brown when the temperature reaches 210°C. At this temperature, a slight turbidity becomes noticeable. The turbidity increases in time with the formation of a black suspension as the reaction mixture is exposed at 210-220°C for 3 hours. In contrast, turbidity appears at 150-160^{o}C in DEG-solution systems. The progress of crystallization was monitored by taking aliquots of solution at different time intervals after reaching 180°C. The TEM tests at early times showed shapeless 11-16 nm agglomerates formed from small (4-6 nm) nanoparticles (Figure 3.4a). High resolution images clearly showed lattice fringes on many of these agglomerates (Figure 3.4b). Remarkably, the fringes were aligned within

many agglomerates. As the annealing is continued at 210-220^{o}C for 2-3 hours, the initial shapeless solid formations are gradually converted into compact nanocrystals with an average size 12.7 nm and well-developed crystal lattice (Figures 3.2c, 3.3c and 3.4c). By varying the solvent weight ratio (DEG/NMDEA) from 1:1 to 3:1 and 1:3, changes in the final size of the magnetite nanocrystals are observed. TEM measurements showed that magnetite nanoparticles obtained from a 3:1 mixture of DEG and NMDEA have an average size of 10.2 nm (Figures 3.2b and 3.3b), whereas those prepared from a 1:3 mixture of the two chelating solvents have a mean size of 14.4 nm (Figures 3.2d and 3.3d). This is understandable since the turbidity appears at 180-190^{o}C in the 3:1 mixed solvent system and at 210-220^{o}C in the 1:3 mixed solvent system, beginning with 5 minutes of heating in this temperature range.

Reactions in neat NMDEA solvent, maintained under the same conditions as the mixed solvent system, showed similar behavior. As expected, reactions in this medium produced the largest nanocrystals (16.8 nm). While the smaller nanocrystals have spheroidal shape, the larger ones are faceted. The shape of a small number of nanocrystals indicates they formed by fusion of two or more nanoparticles (Figures 3.2e and 3.3e). Therefore, there is a substantial difference in the course of reactions in solutions of DEG and NMDEA. Hydrolysis reactions in DEG followed by nanocrystal nucleation and growth occur with high rate. Aging of the resulting colloids causes internal recrystallization of the nanoparticles without any significant mass transport. This result suggests that formation of metal oxides from chelate DEG complexes is irreversible. In contrast, hydrolysis reactions of metal chelates in solutions containing NMDEA occur at higher temperature and with slower rate. The initially formed small

nanoparticles (4-6 nm) quickly agglomerate into shapeless aggregates (11-16 nm), which then undergo slow recrystallization to produce secondary nanocrystals with sizes ranging between ~10 nm and ~15 nm in mixed solvent systems or 16.8 nm in pure NMDEA. Because this recrystallization is accompanied by significant mass transport, this step probably involves an equilibrium between solid oxide and metal complexes in solution. Coalescence of small nanocrystals followed by recrystallization and formation of larger ones has been found in many colloidal systems with metal oxides.[54-59]

3.3.2. Crystal structure and morphology of magnetite nanoparticles. The structure and phase purity of Fe_3O_4 nanoparticles with various sizes were investigated by powder X-ray diffractometry (XRD). Figure 3.1 shows the X-ray diffraction patterns of the nanopowders obtained from neat DEG (e), neat NMDEA (a), and mixtures of DEG and NMDEA with different weight ratios (b, c, and d). The patterns were found to match well with that of cubic crystalline bulk magnetite (JCPDS file No. 19-629) with no other secondary iron oxide phases. The corresponding values of the refined lattice parameter 8.419(3) Å, 8.384 Å, 8.381(7) Å, 8.365(4) Å, and 8.388(6) Å, are in good agreement with the value reported for the bulk substance (8.396 Å).[60] The peak broadening of the studied powders decreases from (e) to (a), which is indicative of the nanocrystalline nature of the materials. The crystallite size was estimated from the six most intense peaks of each X-ray diffraction pattern using Scherrer's formula;[61] the calculated average values are 6.4 nm (a), 10.6 nm (b), 12.3 nm (c), 15.4 nm (d), and 17.4 nm (e).

Details about the structure and morphology of the obtained nanoparticles were provided by TEM studies. Figures 3.2 (a-e) and 3.3 (a-e) show the TEM micrographs of different-sized Fe_3O_4 nanoparticles. The nanocrystals are clearly separated from each

other in monolayers and their shape changes with increasing size from almost spherical (a, b, c) to hexagonal (d, e). The average sizes were estimated to be 5.7 nm (a), 10.2 nm (b), 12.7 nm (c), 14.4 nm (d), 16.8 nm with corresponding standard deviation values (δ) of 16.2%, 13.2%, 8.8%, 11.4%, and 11.5% (Figure 3.5). The sizes of the nanocrystals determined by TEM were in good agreement with the size calculated from peak broadening in X-ray diffractograms, indicating that most of the nanoparticles are single-crystalline.

The selected area electron diffraction (SAED) pattern (Figure 3.6), taken from a monolayer of 12.7 nm-sized Fe_3O_4 nanoparticles, contains six well-defined spotted rings. As anticipated, the spotted appearance of the diffraction rings is due to high crystallinity of the obtained nanoparticles. The corresponding interplanar spacings calculated from the SAED pattern are presented in Table 3.1. The values obtained are consistent with those obtained from the X-ray diffraction pattern, as well as those corresponding to standard bulk Fe_3O_4 (JCPDS file No. 19-629).[62]

The HRTEM image of a typical 12.8 nm-sized Fe_3O_4 nanoparticle is presented in Figure 3.4c. The micrograph reveals highly ordered lattice fringes with a fringe separation of 4.83 Å, which corresponds to {111} lattice planes. This value agrees well with that of 4.85 Å determined from the analysis of the XRD pattern. Although most of the nanoparticles are single-crystalline, a small number of twinned nanocrystals were also observed (Figure 3.4d), supporting coalescence of the primary particles as one of the steps in their crystallization.

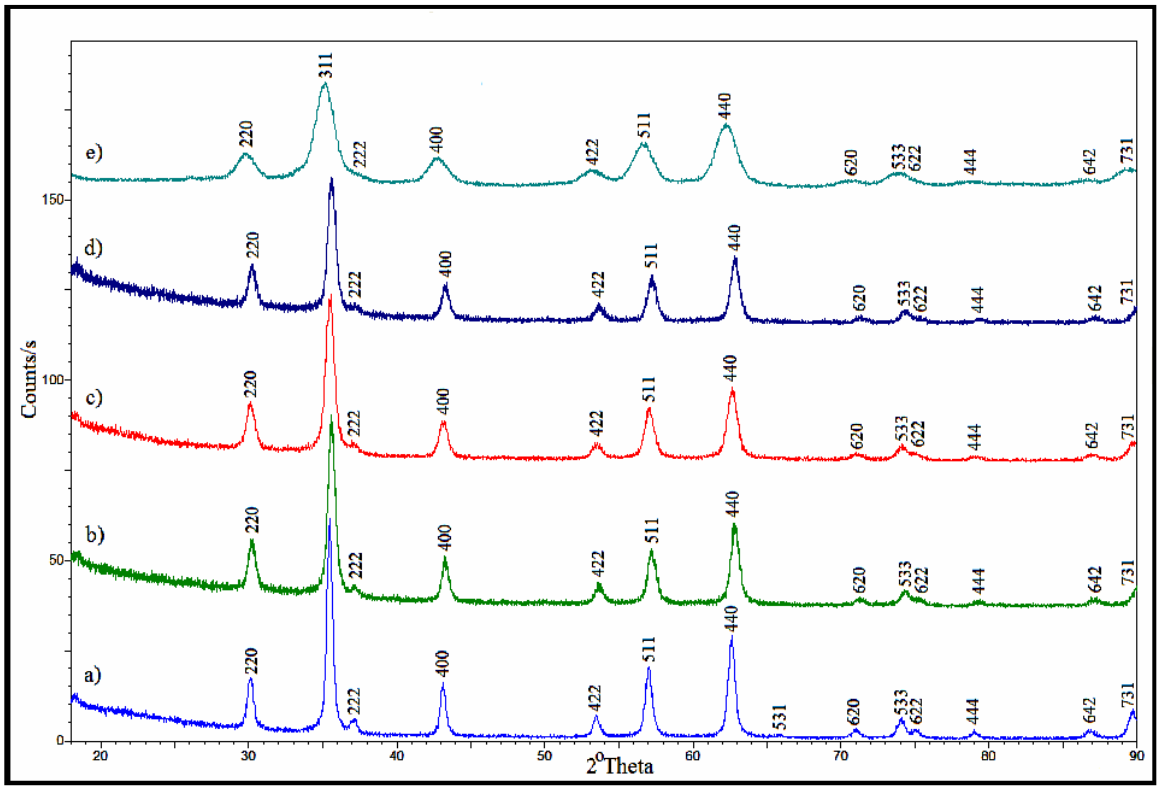

Figure 3.1. X-ray diffraction patterns of the nanopowders obtained from neat NMDEA (a), a 1:3 mixture of DEG and NMDEA (b), a 1:1 mixture of DEG and NMDEA (c), a 3:1 mixture of DEG and NMDEA (d), and neat DEG (e).

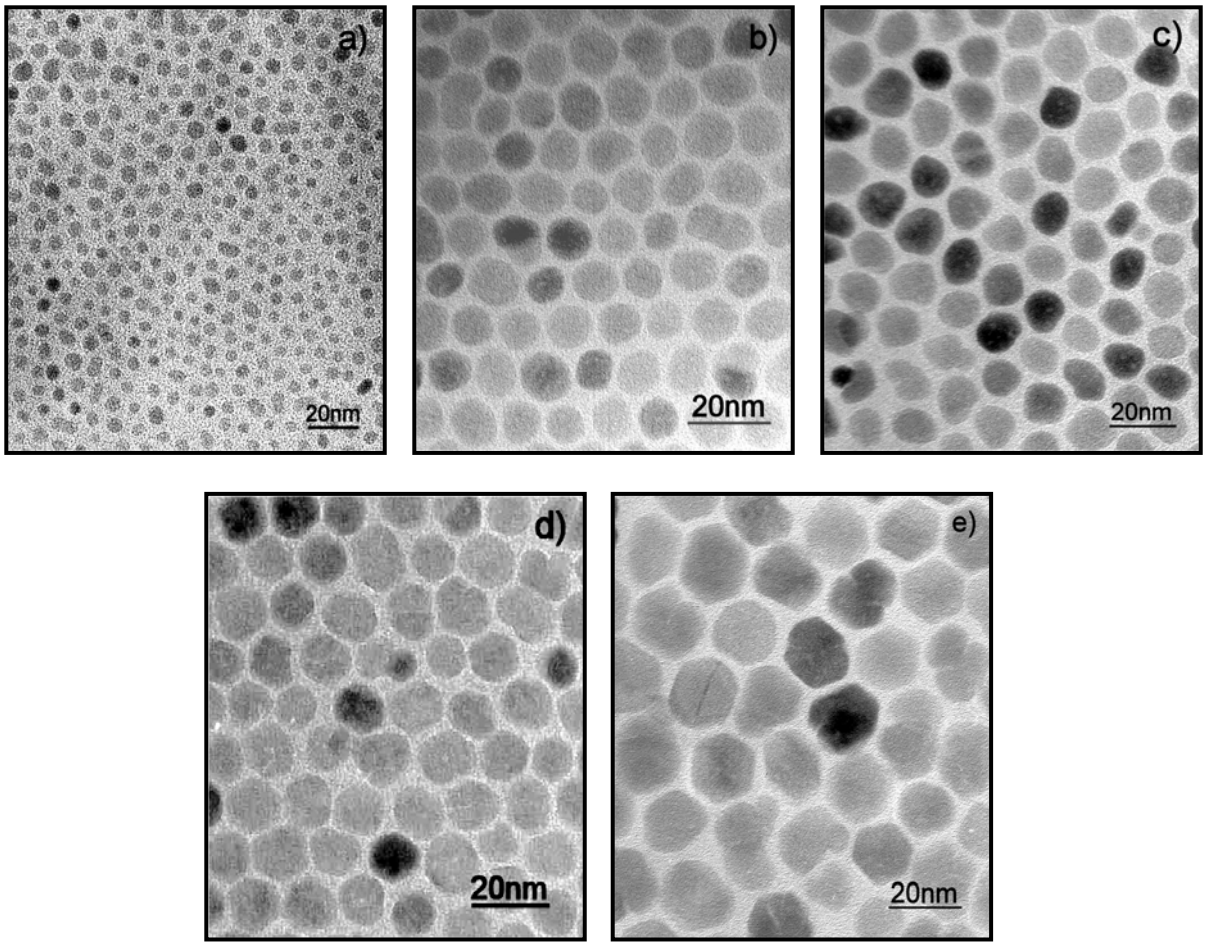

Figure 3.2. TEM bright field images of Fe_3O_4 nanoparticles obtained from DEG (a), a 3:1 mixture of DEG and NMDEA (b), a 1:1 mixture of DEG and NMDEA (c), a 1:3 mixture of DEG and NMDEA (d) , and NMDEA (e).

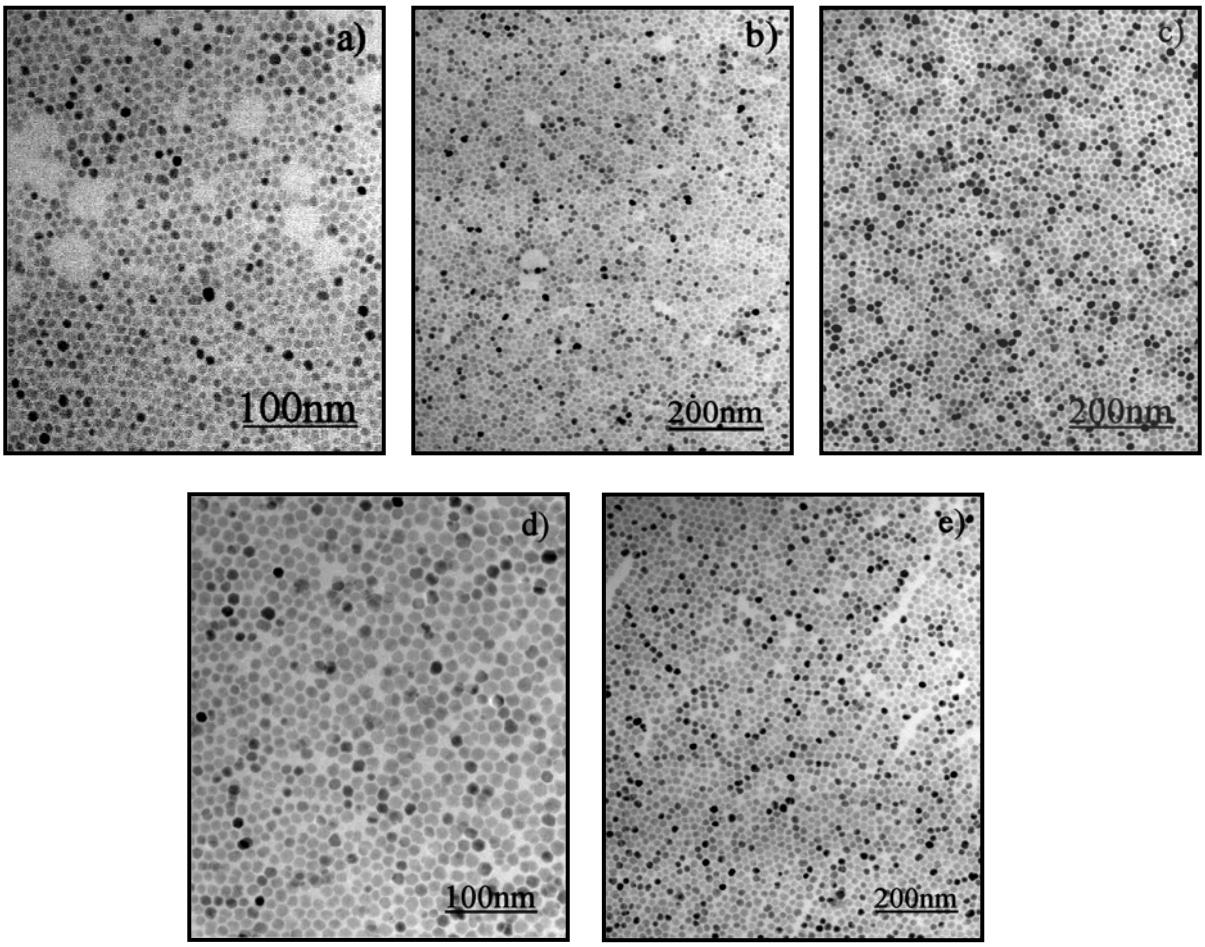

Figure 3.3. Low-magnification TEM micrographs of Fe_3O_4 nanocrystals prepared from neat DEG (a), a 3:1 mixture of DEG and NMDEA (b), a 1:1 mixture of DEG and NMDEA (c), a 1:3 mixture of DEG and NMDEA (d), and neat NMDEA (e)

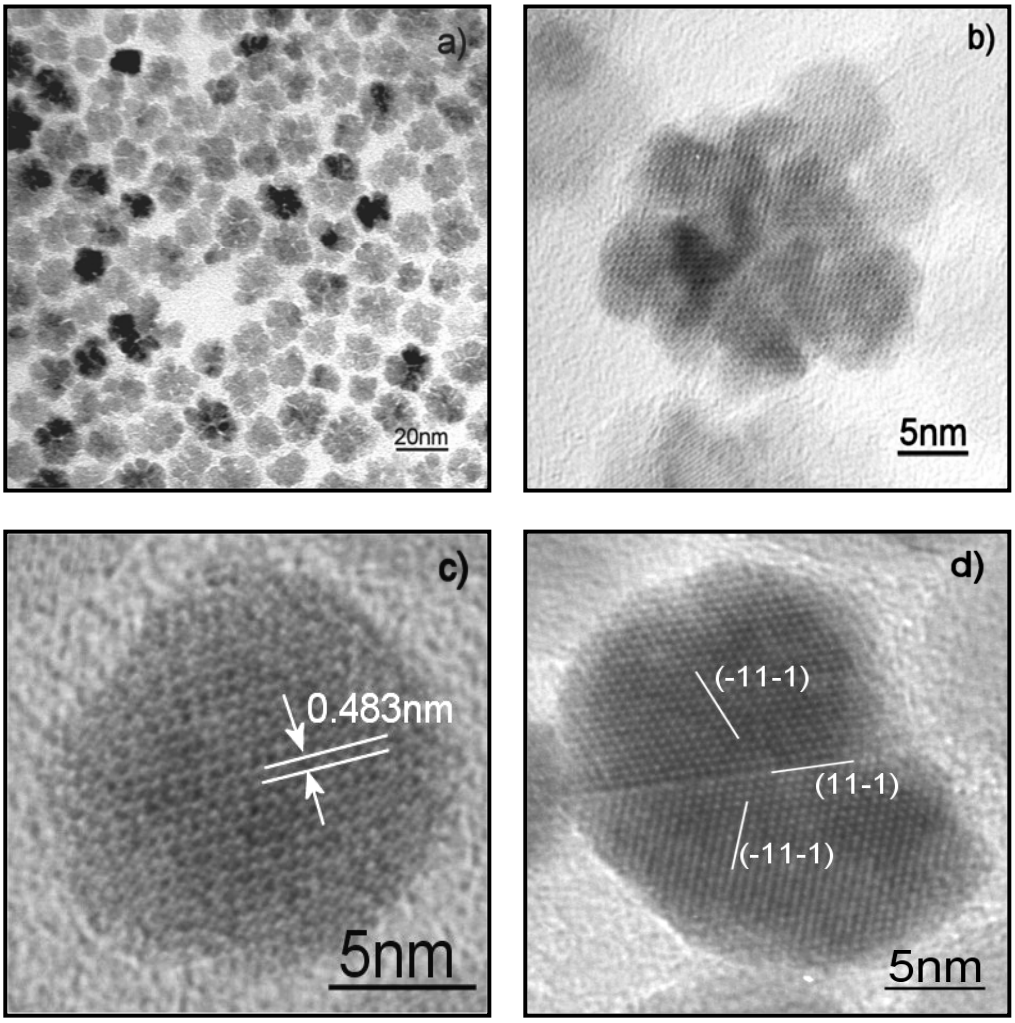

Figure 3.4. TEM bright field image of Fe_3O_4 nanoparticles obtained from a mixture of DEG and NMDEA (1:1,w/w) at the initial phase of synthesis (a), and corresponding HRTEM image of a typical agglomerate (b); HRTEM image of a single 12.8 nm-sized Fe_3O_4 nanoparticle viewed along the [10-1] zone axis (c); HRTEM image of a twinned Fe_3O_4 nanoparticle obtained from neat NMDEA (d)

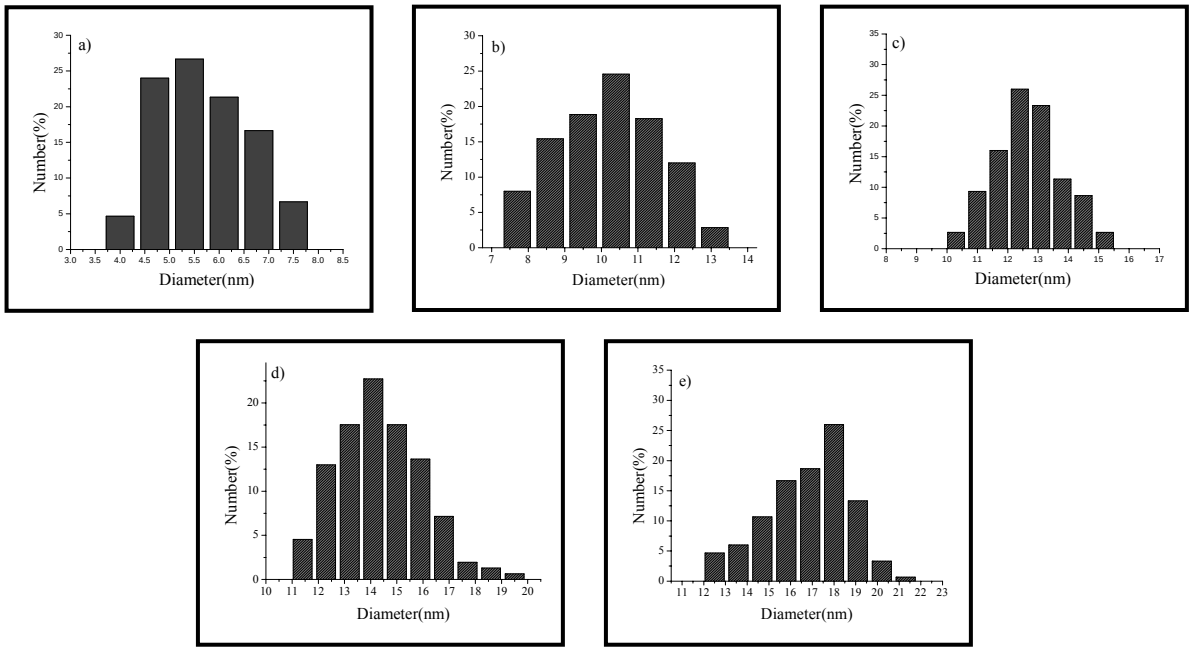

Figure 3.5. Particle size histograms of Fe_3O_4 nanoparticles prepared from neat DEG (a), a mixture of DEG and NMDEA (3:1, w/w) (b), a mixture of DEG and NMDEA (1:1, w/w) (c), a mixture of DEG and NMDEA (1:3, w/w) (d), and neat NMDEA (e).

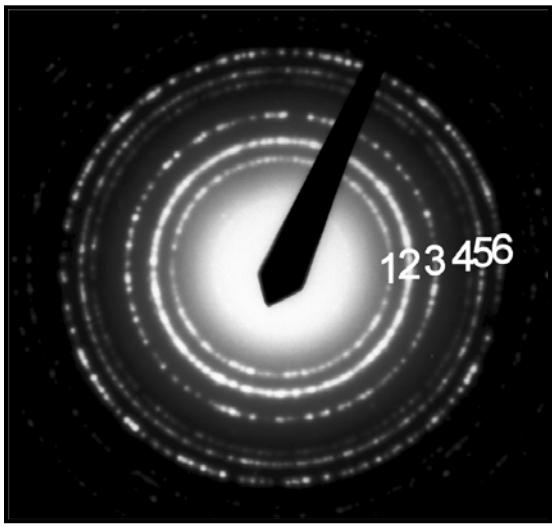

Figure 3.6. SAED pattern of Fe_3O_4 nanoparticles prepared from a mixture of DEG and NMDEA (1:1, w/w)

Table 3.1. Interplanar spacings, *d* (Å), deduced from the analysis of SAED and XRD Patterns and the values corresponding to standard bulk magnetite

Diffraction ring	1	2	3	4	5	6
SAED	3.089	2.624	2.194	1.784	1.694	1.550
XRD (Figure 3.1c)	2.965	2.526	2.095	1.710	1.613	1.481
XRD (Standard bulk Fe_3O_4)	2.967	2.532	2.099	1.714	1.615	1.484
hkl	220	311	400	422	511	440

3.3.3. Surface of magnetite nanoparticles. A thermogravimetric study of the magnetite nanoparticles obtained from DEG and NMDEA solutions was performed over the range of temperature 20-600^{o}C in air and argon atmosphere. The first and brief event of weight loss occurs below 100^{o}C and is due to evaporation of the absorbed solvent. The TGA curves corresponding to the runs in air show a weight gain effect between 125-175^{o}C, presumably attributable to oxidation of the core Fe_3O_4 to Fe_2O_3. Such a curve representing the Fe_3O_4 nanocrystals prepared from neat NMDEA is shown in Figure 3.7. The residues after decomposition of the samples in air at the temperatures 600^{o}C were identified by X-ray diffractometry as α-Fe_2O_3 (Figure 3.8). Regardless of the atmosphere, the main weight loss starts at ~175^{o}C and ends at ~ 325^{o}C when the rate of heating is 2 deg/min. The values of the mass change in the temperature range 175-600°C correlated with particle size are presented in Table 3.2. A typical TGA curve corresponding to the run in argon atmosphere and representing the 10.2 nm Fe_3O_4 nanocrystals is shown in Figure 3.9. The observed weight loss is due to evaporation of the adsorbed DEG, NMDEA and water from the surface of nanoparticles, as well as to dehydration of the surface OH-groups.

We attempted to characterize the composition of the surface by IR spectroscopy, but the quality of the spectra was unsatisfactory due to a low concentration of organic component. To solve this problem, we used destructive methods to separate the organic and inorganic constituents and then used ^{1}H NMR spectrometry for identification of the organic component and determination of its content semiquantitatively by integration.

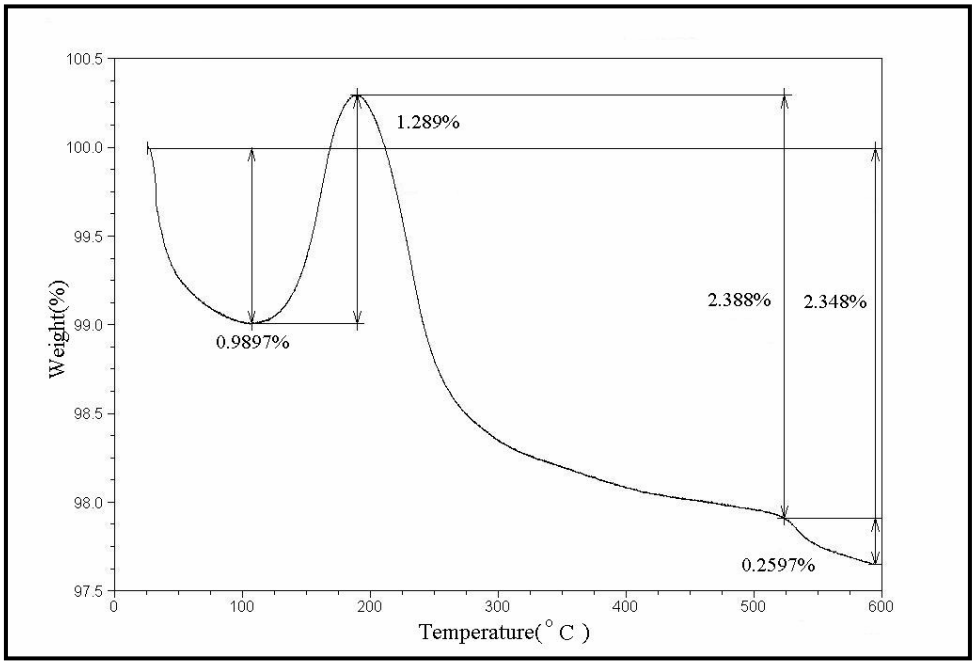

Figure 3.7. TGA curve for the uncapped Fe_3O_4 nanoparticles prepared from neat NMDEA; the measurement was performed in air with a heating rate of 2 deg/min up to 600° C.

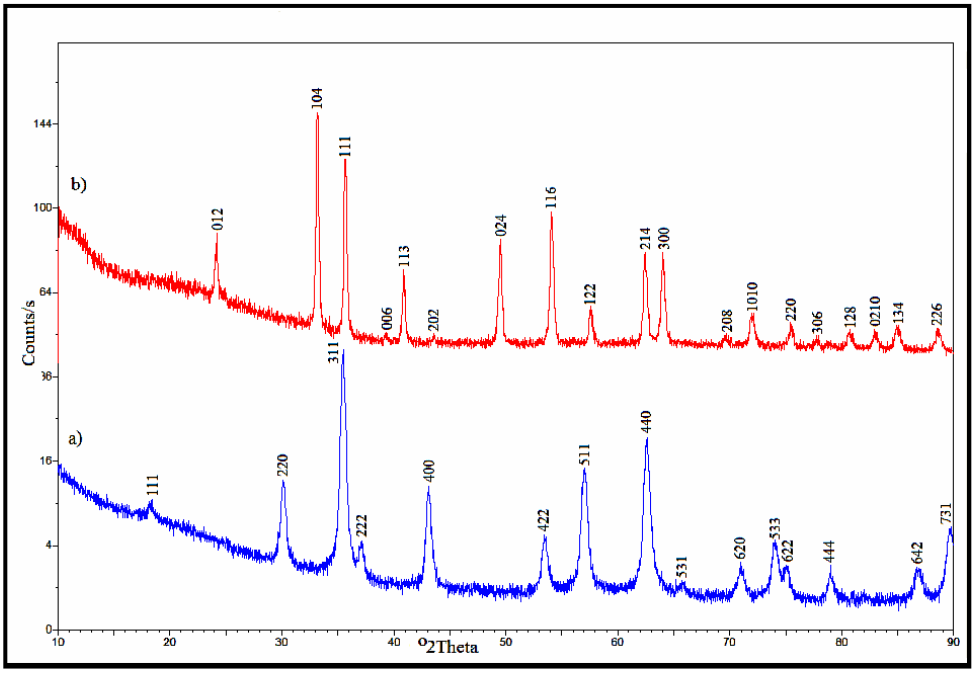

Figure 3.8. X-ray diffraction patterns for the uncapped Fe_3O_4 nanoparticles prepared from neat NMDEA (a), and α-Fe_2O_3 obtained after TGA measurement in air (b).

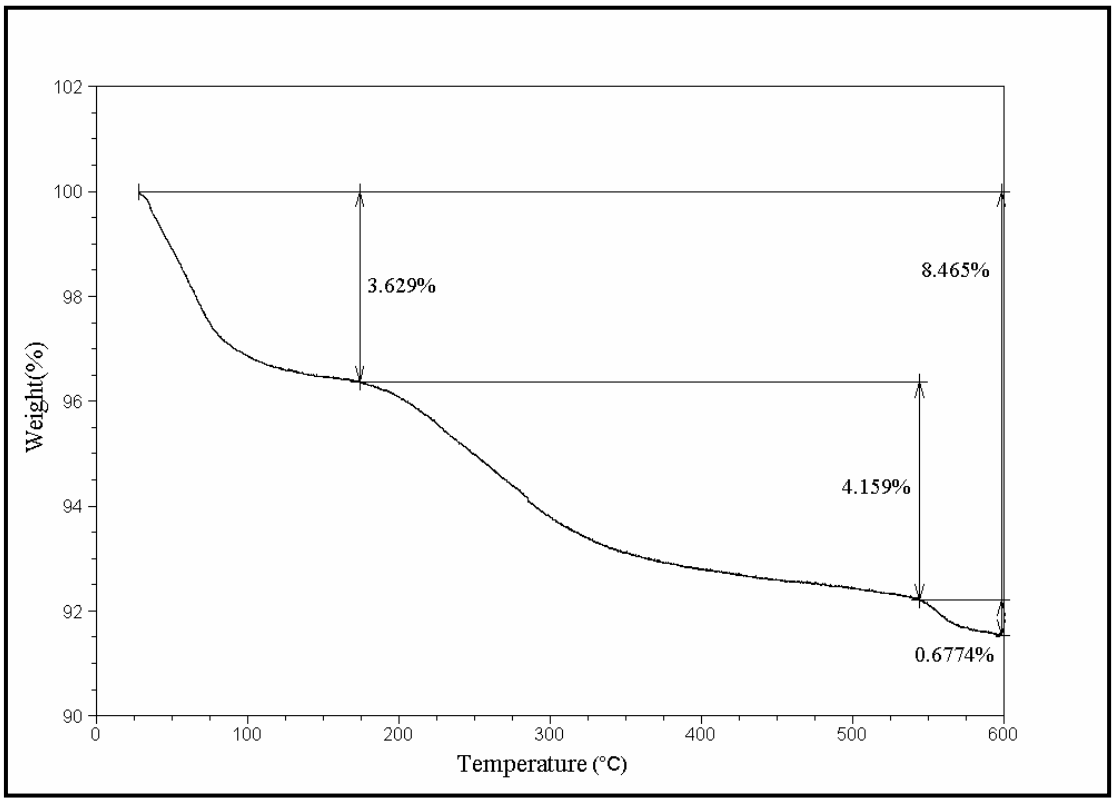

Figure 3.9. TGA curve for uncapped 10.2 nm-sized Fe_3O_4 nanoparticles prepared from a mixture of DEG and NMDEA (3:1, w/w); the measurement was performed in argon atmosphere at a heating rate of 2 deg/min up to 600° C.

Table 3.2. Correlation between particle size (nm) and weight loss (%) determined from the analysis of TGA curves corresponding to the measurements in argon atmosphere.

Sample	Particle size (TEM) (nm)	Weight loss (175 - 600° C) (%)
Fe_3O_4 (neat DEG)	5.7	5.412
Fe_3O_4 (DEG:NMDEA = 3:1,w/w)	10.2	4.827
Fe_3O_4 (DEG:NMDEA = 1:1,w/w)	12.7	4.489
Fe_3O_4 (DEG:NMDEA = 1:3,w/w)	14.4	4.334
Fe_3O_4 (neat NMDEA)	16.8	2.885

Exact quantities of nanopowder and deuterium oxide were sealed in an ampoule and heated at 100^{o}C to extract the organic constituent into solution and facilitate coagulation of iron oxide. After heating for ~ 1 hour, the ampoule was opened and the resulting clear colorless solution was separated, weighed and transferred into an NMR tube. A measured quantity of DMSO was added as a standard for integration. The sample synthesized from DEG solution revealed only DEG and DMSO peaks in its proton spectrum (Figure 3.10). The content of DEG in the nanopowders determined by integration was 2.9% by weight. Although the accuracy of this determination is subject to limitations inherent in integration, the result still clearly indicates that DEG is not merely a contaminant, but a constituent. The sample synthesized from a mixture of DEG and NMDEA formed a much more stable colloid in deuterium oxide that could be decomposed only at 170^{o}C after heating for 1 hour. The NMR spectrum showed no peaks for NMDEA, but only peaks of unidentified substance(s). A detailed analysis was not possible, since the residual paramagnetic species in solution caused substantial line broadening. Alternatively, a sample of the nanopowder was thermally decomposed at 200-350^{o}C in vacuum and the volatile products of its thermolysis were collected and analyzed by NMR. The results proved that NMDEA decomposed under these conditions results into a mixture of unidentified substances.

Thus, the only evidence of its presence in the samples was the strongly basic pH of their aqueous solutions. All nanocrystalline magnetite products contained different quantities of adsorbed volatile constituents, more for smaller nanocrystals and less for larger ones. These substances were identified as diethylene glycol and the decomposition products of N-methyl diethanolamine.

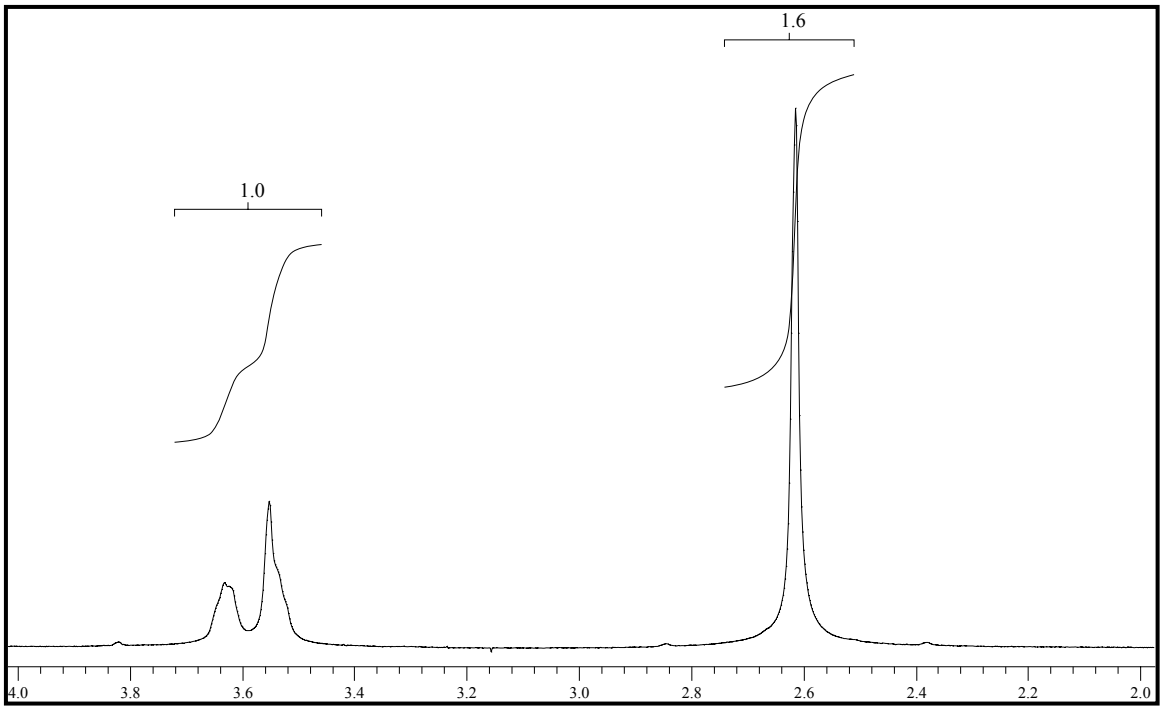

Figure 3.10. ^{1}H NMR spectrum of the product of decomposition of Fe_3O_4 nanoparticles in D_2O solution; peak at 2.61 ppm represents DMSO added as a standard for integration.

3.3.4. Nanocrystals' surface reactivity and dispersibility. The reactivity of the obtained nanocrystalline magnetite products was tested using their reaction with oleic acid in toluene solution. This test was based on the ability of inorganic nanocrystals capped with long-chain carboxylates to form colloids in hydrocarbons. Additional examination of their ability for repeated colloid formation after precipitation may be used for testing how strongly the capping ligand is bound to the nanocrystal surface. The nanopowders synthesized from DEG or NMDEA/DEG solutions exhibited high reactivity, dissolving at room temperature or after short refluxing. Addition of methanol to the resulting dispersions caused precipitation of solids that were separated, washed with methanol and tested for solubility in toluene. We determined that DEG-derived nanopowders could be re-dispersed in toluene, whether or not refluxing was used when they reacted with oleic acid. However, oleate-capped nanocrystals originating from DEG/NMDEA lost their dispersibility if refluxing was not used when they were reacted with oleic acid. As refluxing was used, the solids remained dispersible in toluene. Magnetite samples synthesized using neat NMDEA were always the least reactive. Their complete dissolution in toluene/oleic acid solution could not be achieved even after prolonged refluxing.

Analysis of the surface showed that all nanocrystals contain organic compounds, either DEG or NMDEA or both. It is not clear how these molecules are bound to the nanocrystal surface, although it is likely they partially use their chelating properties. Evidently, these organic constituents play the essential role in protecting the nanocrystals against agglomeration and consequently, their surface reactivity and dispersibility. It is likely that when the DEG-containing nanopowders react with oleic acid, the carboxyl

group binds directly to the surface metal ions, replacing DEG molecules. This chemical bonding provides stability and dispersibility, and, as we observed, the capping ligand cannot be removed by washing. The products of synthesis from NMDEA contain basic amine functions on the surface of nanocrystals, which changes their reactivity with carboxylic acids. It is likely that at room temperature the interaction is limited to the formation of hydrogen bonds between carboxylic and amino groups. Oleic acid adsorbed via hydrogen bonding can be easily removed by washing with alcohols. At an elevated temperature and in the presence of an excess of oleic acid, the final product contains oleate ligand covalently bound to the surface of nanocrystals similar to the ones obtained from DEG.

The isolated nanocrystalline magnetite was tested for dispersibility in methanol, ethanol, and water. Most of the tested samples could be dispersed in pure solvents (Figure 3.11a); however, the dissolution was dramatically facilitated by the presence of traces of mineral or carboxylic acids. Colloidal solutions of Fe_3O_4 nanoparticles prepared from 1:1 mixtures of DEG and NMDEA are obtained with concentrations as high as 32 mg/mL in water, 26.5 mg/mL in methanol, and 13 mg/mL in ethanol. Acidification not only improved the dispersing, but also caused great stabilization: both aqueous and alcohol colloids containing 75 μmol/L of HCl were stable for very long periods of time. The TEM examination of an aqueous dispersion aged for 3 months revealed their non-aggregate nature (Figure 3.11b).

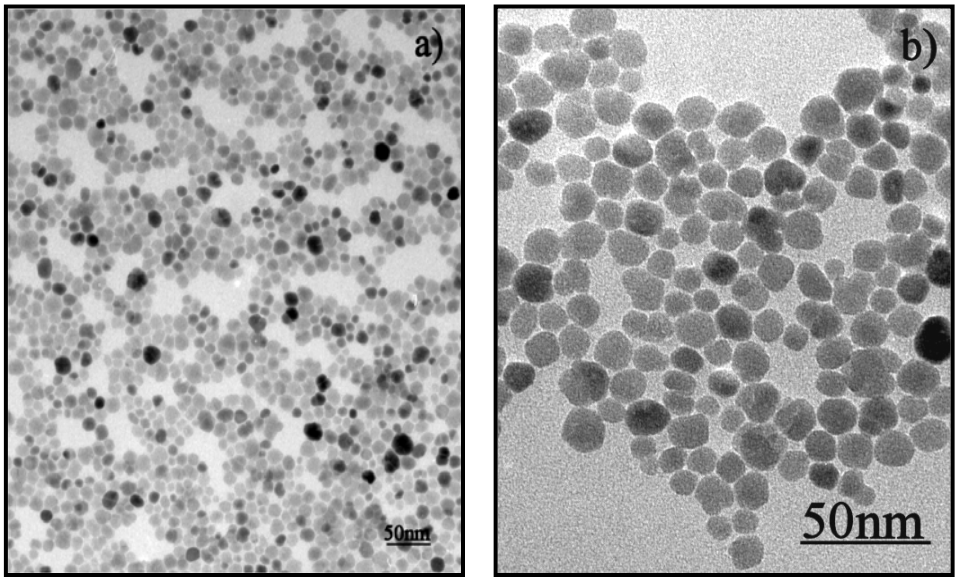

Figure 3.11. TEM micrographs of Fe_3O_4 nanoparticles prepared from a 1:1 mixture of DEG and NMDEA: freshly-prepared aqueous dispersion (a), and aqueous dispersion acidified and aged for 3 months (b).

3.4. Conclusion

The high-yield synthesis of the uncapped nanocrystals of Fe_3O_4 with chemically active surfaces is accomplished by the elevated-temperature hydrolysis of chelate iron alkoxide complexes in solutions of diethylene glycol and N-methyl diethanolamine. The rate of this reaction is easily controlled by changing the temperature and concentration of the reactants, and high yield is obtained due to the practically irreversible hydrolysis. The highly polar medium of alcohol and by-product ions (Na^+, Cl^-) stabilizes the colloids, which is essential for the nucleation and growth steps. As the stability of these colloids becomes exhausted, the oxides precipitate as nanopowders whose surface is passivated by a labile layer of the adsorbed solvent. The different donor properties of diethylene glycol and N-methyl diethanolamine affect the rate of hydrolysis and crystallization, and therefore the final size of the nanocrystals. The smallest (5.7 nm) and largest (16.8 nm) nanocrystals were obtained in the former and the latter solvents, respectively. Nanocrystals with sizes ranging from ~10 nm to ~15 nm were obtained in mixed solvent systems with different weight ratios of the two chelating solvents. We believe that this method can be used for synthesis of other metal oxides nanocrystals with various sizes and chemically active surfaces. The isolated nanocrystalline powders are easily dispersible in toluene in the presence of oleic acid and in water or alcohol (methanol and ethanol) without using a surfactant. This property of the nanoscaled magnetite, as a biologically compatible magnetic material, may promote its application in biology and medicine as a component for diagnostic and therapeutic tools.

3.5. References

1. Kang, Y. S.; Risbud, S.; Rabolt, J. F.; Stroeve, P. *Chem. Mater*. **1996**, *8*, 2209.
2. Kim, D. K.; Mikhaylova, M.; Zhang, Y.; Muhammed, M. *Chem. Mater*. **2003**, *15*, 1617.
3. McKenzie K. J.; Marken, F. *Pure Appl. Chem*. **2001**, *73*, 1885.
4. Sousa, M. H.; Tourinho, F. A.; Depeyrot, J.; da Silva, G. J.; Lara, M. C. F. L. *J. Phys. Chem. B* **2001**, *105*, 1168.
5. Aquino, R.; Tourinho, F.A.; Itri, R.; e Lara, M. C. F. L.; Depeyrot, J. *J. Magn. Magn. Mater*. **2002**, 252, 23.
6. Zaitsev, V. S.; Filimonov, D.S.; Presnyakov, I.A.; Gambino, R. J.; Chu, B. *J. Colloid Interface Sci*. **1999**, *212*, 49.
7. Babes, L.; Denizot, B.; Tanguy, G; Le Jeune, J. J.; Jallet, P. *J. Colloid Interface Sci*. **1999**, *212*, 474.
8. Sauzedde, F.; Elaïssari, A.; Pichot, C. *Colloid Polym. Sci*. **1999**, *277*, 846.
9. Marquez, M.; Robinson, J.; Van Nostrand, V.; Schaefer, D.; Ryzhkov, L. R.; Lowe, W.; Suib, S. L. *Chem. Mater*. **2002**, *14*, 1493.
10. Pileni, M. P.; Lisiecki, I.; Motte, L.; Petit, C.; Tanori, J.; Moumen, N. In : *Micelles, Microemulsions, Monolayers;* Shah, D. O., Ed.; Dekker: New York, 1998; p. 289.
11. Pileni, M. P.; Feltin, N.; Moumen, N. In: *Scientific and Clinical Applications of Magnetic Carriers*; Haefeli, U., Ed.; Plenum Press: New York, 1997; p. 117.
12. Hochepied, J. F.; Bonville, P.; Pileni, M. P. *J. Phys. Chem. B* **2000**, *104*, 905.
13. Rondinone, A. J.; Samia, A. C. S.; Zhang, Z. J. *J. Phys. Chem. B* **1999**, *103*, 6876.
14. Rondinone, A. J.; Samia, A. C. S.; Zhang, Z. J. *J. Phys. Chem. B* **2000**, *104*, 7919.

15. Liu, C.; Zou, B.; Rondinone, A. J.; Zhang, Z. J. *J. Am. Chem. Soc.* **2000**, *122*, 6263.

16. Ocana, M.; Morales, M. P.; Serna, C. J. *J. Colloid Interface Sci*. **1999**, *212*, 317.

17. Ocana, M.; Matijevic, E. *J. Mater. Res.* **1990**, *5*, 1083.

18. Verges, M. Andres; Mifsud, A.; Serna, C. J. *J. Chem. Soc., Faraday Trans*. **1990**, *86*, 959.

19. Morales, M. P.; Gonzalez-Carreno, T.; Serna, C. J. *J. Mater. Res.* **1992**, *7*, 2538.

20. Matijevic, E.; Sapieszko, R. S. *Surfactant Sci. Ser.* **2000**, *92*, 2.

21. Blesa, M. A.; Matijevic, E. *Adv. Colloid Interface Sci.* **1989**, *29*, 173.

22. Ammar, S.; Helfen, A.; Jouini, N.; Fiévet, F.; Rosenman, I.; Villain, F.; Molinié, P.; Danot, M. *J. Mater. Chem.* **2001**, *11*, 186.

23. Rajamathi, M.; Ghosh, M.; Seshadri, R. *Chem. Commun*. **2002**, 1152.

24. Liu, C.; Zou, B.; Rondinone, A. J.; Zhang, Z. J. *J. Am. Chem. Soc.* **2001**, *123*, 4344.

25. O'Brien, S.; Brus, L.; Murray, C. B. *J. Am. Chem. Soc*. **2001**, *123*, 12085.

26. Broussous, L.; Santilli, C. V.; Pulcinelli, S. H.; Craievich, A. F. *J. Phys. Chem.* **2002**, *106*, 2855.

27. Grosso, D.; Sermon, P. *J. Mater. Chem.* **2000***, 10*, 359.

28. Gamard, A.; Babot, O.; Jousseaume, B.; Rascle, M.-C.; Toupance, T.; Campet, G. *Chem. Mater.* **2000**, *12*, 3419.

29. de Monredon, S.; Cellot, A.; Ribot, F.; Sanchez, C.; Armelao, L.; Gueneau, L.; Delattre, L. *J. Mater. Chem.* **2002**, *12*, 2396.

30. Rockenberger, J.; Scher, E.C.; Alivisatos, A. P. *J. Am. Chem. Soc*. **1999**, *121*, 11595.

31. Seo, W. S.; Jo, H. H.; Lee, K.; Park, J. T. *Adv. Mater*. **2003**, *15*, 795.

32. Thimmaiah, S.; Rajamathi, M.; Singh, N.; Bera, P.; Meldrum, F.; Chandrasekhar,

N.; Seshadri, R. *J. Mater. Chem.* **2001**, *11*, 3215.

33. Sun, S.; Zeng, H. *J. Am. Chem. Soc*. **2002**, *124*, 8204.
34. Hyeon, T.; Lee, S. S.; Park, J.; Chung, Y.; Na, H. B. *J. Am. Chem. Soc.* **2001**, *123*, 12798.
35. Bourlinos, A. B.; Simopoulos, A.; Petridis, D. *Chem. Mater*. **2002**, *14*, 899.
36. Trentler, T. J.; Denler, T.E.; Bertone, J. F.; Agrawal, A.; Colvin, V. L. *J. Am. Chem. Soc*. **1999**, *121*, 1613.
37. Boal, A. K.; Das, K.; Gray, M.; Rotello, V. M. *Chem. Mater*. **2002**, *14*, 2628.
38. Shafi, K. V. P. M.; Ulman, A.; Yan, X.; Yang, N. -L.; Estournès, C.; White, H.; Rafailovich, M. *Langmuir* **2001**, *17*, 5093.
39. Wakefield, G.; Keron, H. A.; Dobson, P.J.; Hutchison, J. L. *J. Colloid Interface Sci.* **1999**, *215*, 179.
40. Wong, E. M.; Hoertz, P. G.; Liang, C. J.; Shi, B. -M.; Meyer, G. J.; Searson, P. C. *Langmuir* **2001**, *17*, 8362.
41. Rajamathi, M.; Ghosh, M.; Seshadri, R. *Chem. Commun*. **2002**, 1152.
42. O'Brien, S.; Brus, L.; Murray, C. B. *J. Am. Chem. Soc*. **2001**, *123*, 12085.
43. Skoutelas, A. P.; Karakassides, M. A.; Petridis, D. *Chem. Mater*. **1999**, *11*, 2754.
44. Guo, L.; Yang, S.; Yang, C.; Yu, P.; Wang, J.; Ge, W.; Wong, G. K. L. *Chem. Mater*. **2000**, *12*, 2268.
45. Papisov, M. I.; Bogdanov Jr., A.; Schaffer, B.; Nossiff, N.; Shen, T.; Weissleder, R. *J. Magn. Magn. Mater*. **1993**, *122*, 383.
46. Caruntu, D.; Remond, Y.; Chou, N. H.; Jun, M. J.; Caruntu, G.; He, J.; Goloverda G.; O'Connor, C. J.; Kolesnichenko, V. *Inorg. Chem.* **2002**, *41*, 6137.

47. Sobota, P.; Jozef Utko, Z.; Sztajnowska, K.; Jerzykiewicz, L. B. *New J. Chem*. **1998**, *22*, 851.

48. Sapieszko, R. S.; Matijevic, E. *J. Colloid Interface Sci*. **1980**, *74*, 405.

49. Sapieszko, R. S.; Matijevic, E. *Corrosion* **1980**, *36*, 522.

50. Crans, D. C.; Shin, P. K. *J. Am. Chem. Soc*. **1994**, *116*, 1305.

51. Saalfrank, R. W.; Bernt, I.; Chowdhry, M. M.; Hampel, F.; Vaughan, G. B. M. *Chem. Eur. J.* **2001**, *7*, 2765.

52. Vinogradova, E. A.; Kokozay, V. N.; Vassilyeva, O. Yu.; Skelton, B. W. *Acta Crystallogr., Sect. E* **2003**, *E59*, m148.

53. Hubert-Pfalzgraf, L. G. *Inorg. Chem. Communs*. **2003**, *6*, 102.

54. Pen, L. R.; Banfield, J.; *Am. Mineralogist* **1998**, *83*, 1077.

55. Banfield, J. F.; Welch, S. A.; Zhang, H.; Tomsen-Ebert, T.; Penn, L. R. *Science*, **2000**, *289*, 751.

56. Leite, E. R.; Giraldi, T. R.; Pontes, F. M. *Acta Microscopica* **2003**, *12(C)*, 325.

57. Pacholski, C.; Kornowski, A.; Weller, H. *Angew. Chem. Int. Ed.* **2002**, *41*, 1188.

58. Park, J.; Privman, V.; Matijević, E. *J. Phys. Chem.* **2001**, *105*, 11630.

59. Morales, M. P.; Gonzalez-Carreno, T.; Serna, C. J. *J. Mater. Res.* **1992**, *7*, 2538.

60. Cornell, R. M.; Schwertmann, U. *The Iron Oxides: Structure, Properties, Reactions*, *Occurrence and Uses*; VCH: New York, 1996; p. 28.

61. West, A. R. *Solid State Chemistry And Its Applications*; John Wiley & Sons: London, 1984; p. 174.

62. Ma, M.; Zhang, Y.; Yu, W.; Shen, H.; Zhang, H.; Gu, N. *Colloids Surf., Sect. A,* **2003**, *212*, 3190226.

CHAPTER 4

Magnetic Properties of Variable-Sized Fe_3O_4 Nanoparticles Synthesized from Non-Aqueous Homogeneous Solutions of Polyols

4.1. Introduction

Transition metal ferrites, $M^{II}Fe_2^{III}O_4$, are magnetic materials with a cubic spinel-type structure which have been extensively used in various technological applications in the past decades.[1, 2] Owing to their easy preparation, low fabrication cost, high chemical stability and unique electrical, optical, thermal, rheological, catalytic and magnetic properties, ferrites, either in the form of nanopowders or surface-stabilized nanoparticles suspended in a carrier liquid (ferrofluid)[3] have a widespread use in electronics[4], magneto-optics[5], magnetocaloric refrigeration[6], dynamic sealing[7], high-density information storage[8], oscillation damping[9] and catalysis.[10] Among the nanocrystalline ferrites, Fe_3O_4 and γ-Fe_2O_3 have received a particular interest as ideal candidates for different biomedical applications including enzyme encapsulation[11], biosensor design[12, 13], cell labeling/separation[14] and oligonucleotide identification[15], magnetic resonance imaging (MRI)[16-18], tumor hyperthermia[19, 20], and magnetically-targeted drug delivery[21-24] due to their dimensions comparable with the cells and biomolecules, low toxicity and biocompatibility, high saturation magnetization values and their easy manipulation with low magnetic fields.

As the size of the particles decreases below 100 nm, a large fraction of the constituting atoms will be found on the surface of the nanocrystals; this induces

significant changes in the magnetic structure and properties of the nanophase materials as compared to their bulk counterparts. Specifically, the domain wall structure encountered in the bulk crystalline ferrites is replaced by a single domain structure characteristic to each particle, thus leading to new phenomena, such as superparamagnetism[25], extra anisotropy contributions[26] and spin canting (disordered spin configuration)[27, 28]. Superparamagnetism refers to the random fluctuation of the magnetization of the single-domain particles when the thermal energy overcomes the anisotropy energy barrier. At low temperatures the magnetization of each nanoparticle is oriented parallel to a particular crystallographic direction called easy axis along which the energy of the particle is minimized. The magnetization of the nanoparticle remains blocked in this minimum energy position until an amount of energy at least equal to the anisotropy of the particle is provided to the system. Increasing the temperature above a certain value, known as the blocking temperature (T_B), the thermal energy will overcome the anisotropy energy (E_A) and the magnetization of each particle begins to fluctuate between the two directions of the easy axes. In these conditions, the magnetic system behaves as a classical paramagnet.[29] According to the Stoner-Wohlfarth theory, the blocking temperature is higher as the volume of the nanoparticles increases:

$$T_B = \frac{K}{25k_B} \cdot V ,$$

where K represents the anisotropy constant and k_B is the Boltzmann constant.[30]

In general, the magnetic behavior of the nanoparticles is the result of the interplay between the bulk magnetocrystalline characteristics, finite size effects and collective magnetostatic interactions between the particles. However, the delimitation of each individual contribution to the total magnetization of the magnetic system would require

not only the preparation of well-dispersed nanocrystals with controllable sizes and shapes, but also a strict control over the interactions between them. Finite size effects include the single domain magnetic structure and the surface spin disorder and originate from the high surface/volume ratio of the small particles, whereas the interparticle interactions refers to the exchange and dipole-dipole interactions. The study of the interparticle interactions is not trivial since they can change significantly the magnetic response of a nanosized system by increasing the anisotropy energy barrier (E_A) necessary to overcome the blocking of the magnetization of each particle. Herein, we report on the influence of the finite size effects and interparticle interactions on the magnetic properties of the oleate-capped Fe_3O_4 nanocrystals synthesized in non-aqueous homogeneous solutions of polyols (diethylene glycol and N-methyl diethanolamine). The experiments were performed on two series of samples, one containing Fe_3O_4 particles with various sizes ranging from 6.6 to 17.8 nm and the other one containing 6.6 nm particles diluted at different concentrations paraffin.

4.2. Experimental

4.2.1. Chemicals. Iron(III) chloride hexahydrate 97%, toluene 99.5%, methyl alcohol 99.8%, and hexanes 98.5% were purchased from Merck. Diethylene glycol 99%, N-methyl diethanolamine 99+%, sodium hydroxide 97% (20-40 mesh beads), ethyl acetate 99.5%, and decane 99+% were obtained from Aldrich. Iron(II) chloride tetrahydrate 99% was purchased from Alfa Aesar, oleic acid 90% from Fisher and absolute ethyl alcohol from AAper Alcohol and Chemical Co. Chemicals and solvents

were used without further purification. The air-sensitive chemicals were manipulated in a VAC glovebox with a nitrogen atmosphere.

4.2.2. Synthesis. The synthetic procedures for the preparation of oleate-capped Fe_3O_4 nanocrystals with various sizes are described in detail in the Chapter 3. For example, the ~6 nm-sized magnetite nanoparticles were prepared in diethylene glycol (DEG) solutions obtained by dissolving a mixture of 2 mmol $FeCl_2 \cdot 4H_2O$ and 4 mmol $FeCl_3 \cdot 6H_2O$ in 80 g solvent in a Schlenk flask under protection with argon. Separately, 16 mmol of NaOH was dissolved in 40 g diethylene glycol. The solution of NaOH was added to the solution of metal chlorides with stirring at room temperature causing an immediate color change from yellow-brown to deep green-brown. After 3 hours, the temperature of the solution was raised during 1.5 h to 210ºC and then kept constant for 2 h in the temperature range 210-220ºC. In order to obtain magnetite nanoparticles soluble in nonpolar solvents, a diethylene glycol solution of oleic acid (2.6 mmol oleic acid per 20 g DEG) was added to the reaction mixture at high temperature. This addition immediately precipitated the solids. The mixture was cooled to room temperature and then centrifuged. The precipitates were washed with methanol and dissolved in 20 ml toluene. The resulting solution was centrifuged and mixed with 2-3 volumes of methanol. The precipitate was separated by centrifuging, washed with methanol and kept either moistened with methanol or dispersed in nonpolar solvents (hexanes, toluene, and decane). When magnetic measurements were planned, the solids were dried in a flow of nitrogen.

The largest magnetite nanoparticles (~17 nm) were prepared following a similar synthetic procedure but using N-methyl diethanolamine (NMDEA) instead of diethylene

glycol (DEG) and heating the reaction mixture for 4h in the temperature range 210-220° C. The solid product was isolated by cooling the reaction mixture to room temperature and centrifuging. A black solid was obtained and washed with ethanol twice and with a mixture of ethanol and ethyl acetate (1:1, v/v) three times to remove the excess of N-methyl diethanolamine. Magnetite nanoparticles soluble in nonpolar solvents were obtained by heating to reflux for ~1 h a mixture containing 182 mg of black powder and a toluene solution of oleic acid (1.95 mmol oleic acid per 50 ml toluene). A deep brown solution was obtained and the solid product was re-precipitated by adding 1-2 volumes of methanol and then washed several times with methanol to remove the excess of oleic acid. The precipitate was dried in a flow of nitrogen.

For the preparation of ~11 nm-sized magnetite nanoparticles, a mixture of diethylene glycol (DEG) and N-methyl diethanolamine (NMDEA) (1:1, v/v) was used in the synthesis and the reaction mixture was heated for 3 h in the temperature interval 210-220° C. The solid product was isolated by cooling the reaction mixture to room temperature and centrifuging. A black solid was obtained and washed with ethanol twice and with a mixture of ethanol and ethyl acetate (1:1, v/v) three times to remove the excess of diethylene glycol and N-methyl diethanolamine. In order to obtain magnetite nanoparticles soluble in nonpolar solvents, a mixture containing 120 mg of black powder and a toluene solution of oleic acid (1.26 mmol oleic acid per 50 ml toluene) was heated to reflux for ~1 h. A deep brown solution was obtained and the solid product was re-precipitated by adding 1-2 volumes of methanol and then washed several times with methanol to remove the excess of oleic acid. The resulted black solid was dried in a flow of nitrogen.

4.2.3. Characterization. The morphology of the magnetite nanoparticles was examined with a JEOL JEM 2010 transmission electron microscope (TEM) at 200KV. Thermogravimetric analyses (TGA) were carried out in argon at a heating rate of 2°C/min up to 600°C using a SDTQ 600 analyzer. The magnetic measurements of both as-prepared Fe_3O_4 nanoparticles and samples diluted in paraffin were performed with a Superconducting Quantum Interference Device (SQUID) in the temperature range 5-300K and magnetic fields up to 5 T. The zero-field cooled (ZFC) curves were obtained by cooling the magnetite samples from 300 K to 5 K in the absence of an external magnetic field, followed by the measurement of the magnetization under a magnetic field of 100 Oe as the temperature is raised back to room temperature. The field-cooled measurements were carried out in a similar way, except for the cooling process which was performed under an external magnetic field of 100 Oe. The hysteresis loop measurements were performed at different temperatures ranging from 5 to 300K under magnetic fields up to 5T.

4.3. Results and discussion

Highly crystalline magnetite (Fe_3O_4) nanoparticles were prepared at elevated temperatures by the hydrolysis of chelate iron alkoxide complexes in solutions of the corresponding polyols, diethylene glycol (DEG) and N-methyl diethanolamine (NMDEA). Polyols play a multiple role in the formation of nanocrystalline Fe_3O_4 particles serving not only as solvents and complexing agents for the iron (II, III) precursors, but also as stabilizing agents for the resulting nanocrystals. Moreover, the presence of monolayers of polyol molecules adsorbed on the nanocrystals'surface

induces their solubility in polar solvents such as water, methanol, and ethanol. The polyol molecules can be exchanged at elevated temperatures for long-chain carboxylic acids which bind covalently to the surface iron ions via carboxylate groups, thereby stabilizing the particles against agglomeration and rendering them soluble in non-polar media (toluene, hexanes, and decane).[31, 32] These fatty acids are also essential in minimizing the exchange interactions between the superficial iron ions of neighboring Fe_3O_4 nanocrystals such that the interparticle interactions are dominated by the dipole-dipole ones.[33, 34]

Adjusting the complexing strength of the reaction medium by using either neat solvents (DEG or NMDEA) or a 1:1 (w/w) mixture of the two polyols, allowed tuning of the particle dimensions in the range 6-17 nm.[32] Figure 4.1 shows the transmission electron microscope (TEM) images of the Fe_3O_4 nanoparticles prepared from neat DEG (a), neat NMDEA (c), and a mixture of DEG and NMDEA (1:1, w/w) (b), respectively. As revealed by the TEM micrographs, the Fe_3O_4 nanoparticles obtained from neat DEG and the mixture of the two polyols have spheroidal shapes, whereas those synthesized from neat NMDEA are faceted. The nanocrystals are individual and relatively uniform-sized. They arrange in monolayers which exhibit a short range order due to the presence of small fractions of tiny particles and shapeless aggregates (Figures 4.1b and 4.1c) indicating that the Fe_3O_4 nanoparticles are formed through the aggregation of "primary particles".[32] The average particle sizes and the size distributions were estimated by counting 150 nanoparticles. As anticipated, the nature of the reaction medium influences significantly the size of the resulting nanocrystalline particles: while the DEG-mediated reaction leads to 6.6 nm-sized Fe_3O_4 particles (standard deviation, σ=11.3%), a mixture

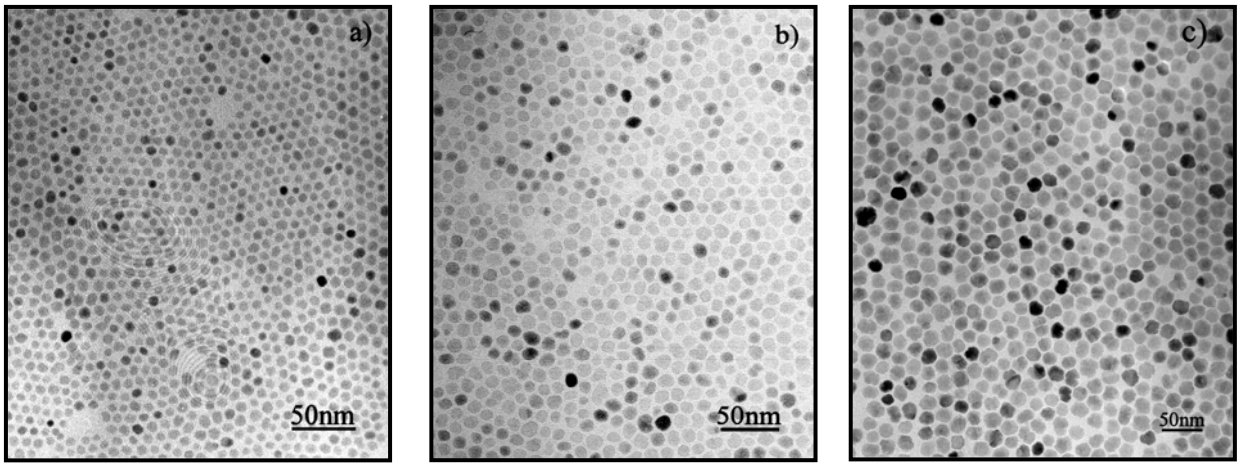

Figure 4.1. Representative transmission electron microscope (TEM) images of oleate-capped magnetite nanoparticles prepared from neat DEG (a), a mixture of DEG and NMDEA (1:1,w/w) (b), and neat NMDEA (c).

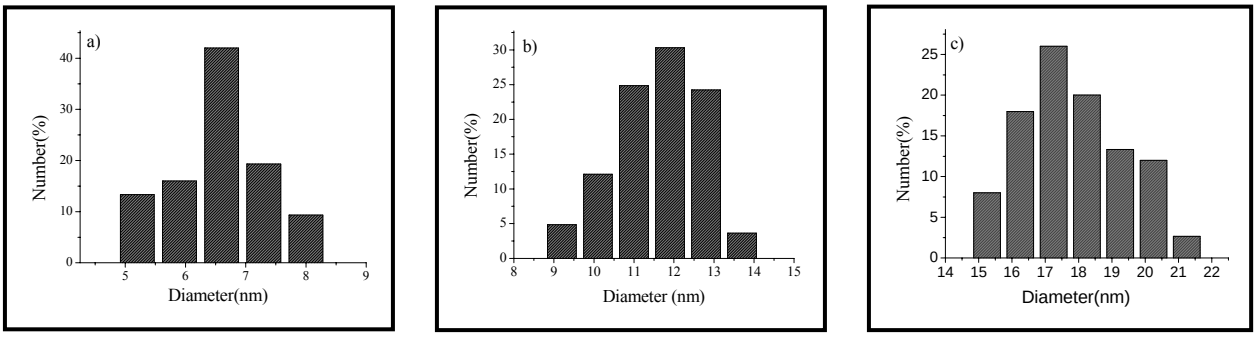

Figure 4.2. Histograms of size distribution for magnetite nanocrystals synthesized from neat DEG (a), a mixture of DEG and NMDEA (1:1, w/w) (b), and neat NMDEA (c).

of DEG and NMDEA (1:1, w/w) results in the formation of particles with an average diameter of 11.6 nm (σ=9.4%) which can be increased to 17.8 nm (σ=10.5%) when the reaction is performed in neat NMDEA (Figure 4.2). The crystallite sizes calculated from the corresponding X-ray diffraction patterns by using the Scherrer's formula led to values similar to those obtained from the TEM measurements, suggesting that the nanopowders consists of single crystalline particles. Additionally, the XRD patterns showed that nanopowders are single phase materials that crystallize into cubic-type structures with the cell parameters comparable to that of the crystalline bulk magnetite (a=8.396 Å).[32]

Figure 4.3 illustrates the temperature (T) dependence of the zero-field (ZFC) and field cooled (FC) magnetizations (M) measured for variable-sized Fe_3O_4 nanoparticles coated with oleate ligand. For the nanoparticles prepared from neat DEG (Figure 4.3(a)) and those synthesized from a 1:1 mixture of DEG and NMDEA (Figure 4.3(b)), the ZFC and FC curves, which coincide initially, start to separate and follow different trends as the temperature is decreased from 300 to 5K. In the FC mode, the magnetization either increases slightly and then levels off (Figure 4.3(a)) or decreases to eventually reach a plateau (Figure 4.3(b)), whereas the ZFC magnetization shows a maximum followed by a steady decrease to a value approaching zero in the low temperature region. The shape of the FC curves in the Figure 4.3(a, b) is the result of the presence of dipole-dipole interactions between the oleate-capped particles.[35, 36] Moreover, the variation of the magnetization in the ZFC and FC modes indicates a superparamagnetic behavior for the 6.6 nm and 11.6 nm-sized Fe_3O_4 particles. The maximum in the ZFC curve defines the blocking temperature T_B, where the thermal energy becomes comparable with the anisotropy energy barrier (E_A). For temperatures below T_B, the magnetization of each

nanoparticle aligns with the direction of the easy axis and cannot be further changed due to the existence of the anisotropy energy barriers. Owing to the random orientation of the easy axes of the nanoparticles, the total magnetization approaches zero at low temperatures. However, when the sample is progressively warmed up to 300 K, an increasing number of particles will acquire a thermal energy comparable to the anisotropy energy, thus switching their magnetizations from the easy axes to the direction of the magnetic field. This leads to a progressive increase of the magnetization of the sample. At temperatures higher than T_B, the magnetization of each particle begins to fluctuate between the two directions of the easy axis (superparamagnetic relaxation). The values of the blocking temperature were found to vary between 203K for the particles obtained from neat DEG (6.6 nm) to 264K for those prepared from a 1:1 mixture of DEG and NMDEA (11.6 nm). In the case of particles synthesized from neat NMDEA (17.8 nm), no maximum was observed in the ZFC curve. However, since the ZFC curve presents a shoulder in the high temperature region, we assume that the blocking temperature of the biggest nanocrystals is situated above 300K. The observed variation of the blocking temperature with the average size of the Fe_3O_4 nanocrystals is consistent with the Stoner-Wohlfarth theory which predicts an increase of the anisotropy energy barrier (E_A) and, consequently, an increase of the blocking temperature (T_B) as the volume of the nanoparticles increases.

Assuming that the particles are non-interacting and possess a uniaxial anisotropy, the corresponding blocking temperatures (T_B) can be used to estimate the values of the anisotropy energy constant (K) of the oleate-capped Fe_3O_4 nanocrystals. The calculated values of the constant are $K=4.74\cdot10^5$ J/m^3 for the particles with an average diameter of

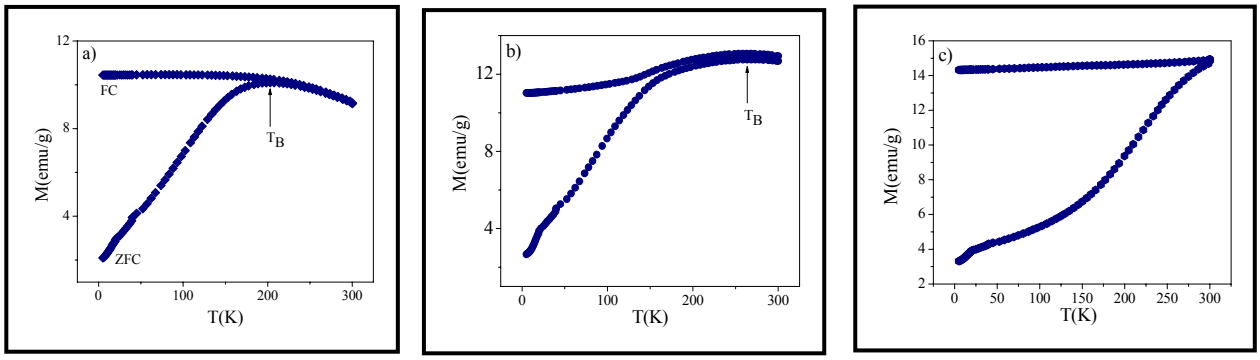

Figure 4.3. Magnetization (M) versus temperature (T) measured in both the zero-field cooled (ZFC) and the field cooled (FC) modes for oleate-capped magnetite nanocrystals with various sizes: 6.6 nm (a), 11.6 nm (b), and 17.8 nm (c).

6.6 nm and $K=1.11\cdot10^5$ J/m^3 for those with a mean size of 11.6 nm, respectively. These values are about one order of magnitude higher than that of the bulk material ($K_{(bulk)}=0.135\cdot10^5$ J/m^3)[28] and were found to increase with decreasing the size of the nanoparticles. Additionally, they are slightly larger, but yet in good agreement with the K values estimated by Mössbauer spectroscopy for 6 nm ($K=1.4\cdot10^5$ J/m^3) and 12 nm ($K=0.9\cdot10^5$ J/m^3)[38] particles or by using the equation $KV=25k_BT$ for 7 nm Fe_3O_4 particles ($K=2.8\cdot10^5$J/m^3)[26], but much lower than that corresponding to 3-7 nm-sized particles obtained by the water-in-oil microemulsion technique ($K=10^6$ J/m^3)[39]. The anisotropy constant (K) of the nanocrystalline materials can incorporate different contributions from magnetocrystalline, shape and surface anisotropy.[26, 40] Thus, assuming that the magnetocrystalline anisotropy of the Fe_3O_4 nanoparticles prepared in the polyol media is invariant to the reaction conditions (the nature of the solvent, the heating time) and the shape of the nanoparticles does not change significantly with their size, the variation trend in K can be ascribed to the concurrent effect of the interparticle interactions[41] and the surface anisotropy[40]. Specifically, the decrease in size of the Fe_3O_4 nanoparticles results in an increased surface spin disorder due to a higher fraction of superficial iron ions with incomplete coordination environments and broken bonds.[27] In such conditions, the surface effects become dominant eventually leading to the increase of the anisotropy energy constant.[42] In Figure 4.4 are represented the hysteresis loops of the three samples of oleate-coated Fe_3O_4 nanocrystals measured at 300 (a) and 5K (b). The corresponding values of saturation magnetization (M_S), squarness ($SQ=M_R/M_S$) and coercivity (H_C) are summarized in Table 4.1. In agreement with the ZFC/FC measurements, the M(H) curves recorded at 300K confirm that the 6.6 nm and 11.6 nm Fe_3O_4 particles present a

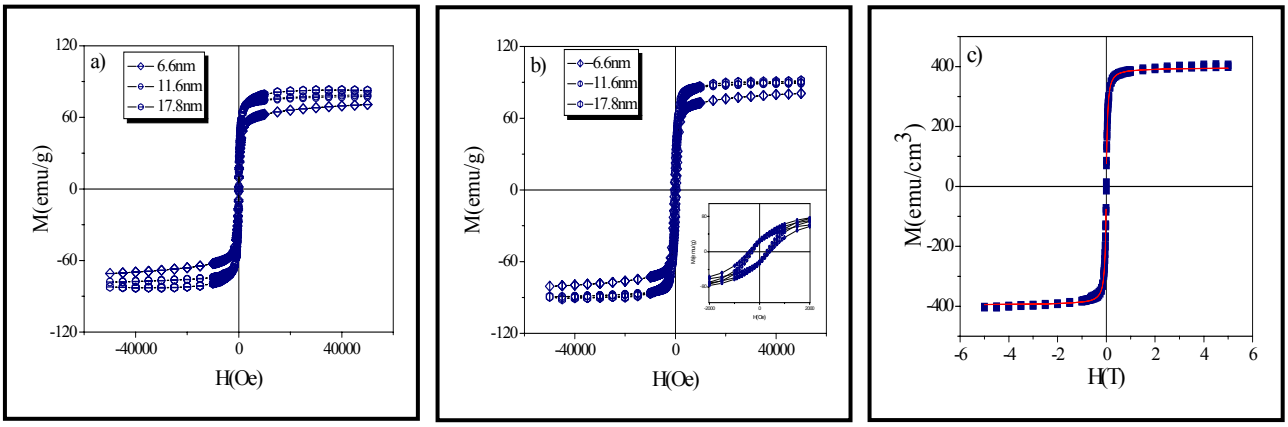

Figure 4.4. Magnetization (M) as a function of the magnetic field (H) measured at 300 (a) and 5K (b) for oleate-capped magnetite nanocrystals with average sizes of 6.6 nm, 11.6 nm, and 17.8 nm, respectively; the fit of M versus H curve recorded at 300K for 11.6 nm-sized Fe_3O_4 nanoparticles (c).

Table 4.1. Magnetic Properties of Variable-Sized Magnetite Nanocrystals Capped with Oleate Ligand.

Average Size (nm)		T_B(K)	M_S (emu/g)		H_C(Oe)		SQ	
TEM	Fit		5 K	300 K	5K	300 K	5 K	300 K
6.6	5.84	203	80.8	70.7	405.6	15.7	0.280	0.0240
11.6	9.95	263.6	89.2	77.4	278.2	14.7	0.250	0.0312
17.8	-	>300	91.3	82.5	379.4	3.4	0.293	0.0076

superparamagnetic behavior, whereas those with a size of 17.8 nm are ferromagnetic exhibiting very low remanence (M_R) and coercivity (H_C). In the superparamagnetic state, the M(H) curves of the nanosized materials can be described by the Langevin function:

$$M(T) = M_S L(x) = M_S\left[\coth(x) - \frac{1}{x}\right] = M_S\left(\frac{e^x + e^{-x}}{e^x - e^{-x}} - \frac{1}{x}\right),$$

where M(T) is the magnetization of the nanosized material at the temperature T, M_S represents the saturation magnetization of the nanosized material, $x=\mu H/k_BT$ and the magnetic moment of the nanoparticles $\mu=M_{S(bulk)}V$ (V stands for the average volume of the nanoparticles).[43] The fit of the M(H) curve for the Fe_3O_4 particles with the average diameter of 11.6 nm (as determined from the TEM measurement) is represented in the Figure 4.4(c), whereas the "magnetic" sizes of the nanoparticles prepared from neat DEG and a 1:1 mixture of DEG and NMDEA are presented in Table 4.1. The diameters of the oleate-capped Fe_3O_4 nanocrystals determined from the fitting of the M versus H curves are consistently smaller than those estimated from the TEM measurements.

Such a discrepancy was previously reported in the literature, being ascribed to the existence of a "dead layer" at the surface of the nanoparticles.[44] Due to their broken bonds, the iron ions contained in the "dead layer" will present a random orientation of their magnetic moments, thereby leading to a decrease of the total magnetization of each individual nanoparticle.[38] The data presented in Table 4.1 show that the saturation magnetization (M_S) of the oleate-capped Fe_3O_4 nanocrystals increases continuously with increasing their average diameter, whereas the coercivity (H_C) follows an opposite trend. The values of the saturation magnetization at 300K are systematically lower than those measured at 5 K presumably due to the thermal fluctuations of the magnetic moments of the nanoparticles at higher temperatures. At 300K, the saturation magnetization increases

from 70.7 emu/g for the nanocrystals prepared from neat DEG (6.6 nm) to 82.5 emu/g for the nanoparticles obtained from neat NMDEA (17.8 nm). Nanocrystalline Fe_3O_4 particles synthesized from the 1:1 mixture of the two polyols (11.6 nm) have an intermediate value of 77.4 emu/g for the saturation magnetization. The M_S values are comparable with those of Fe_3O_4 nanoparticles having similar sizes obtained by other non-aqueous approaches. Specifically, while the 16 nm-sized Fe_3O_4 particles prepared at ~300°C by the "seed-mediated growth" method possess a saturation magnetization of 83 emu/g[46], those with a diameter of 11 nm obtained at 180°C by a solvothermal technique in ethylene glycol medium have a M_s value of 79.2 emu/g[47]. It is worth noticing that for the particles prepared in DEG solutions (6.6 nm), the saturation magnetization is much higher than 49 emu/g, the M_s value measured experimentally for 7 nm Fe_3O_4 particles synthesized at 88°C in aqueous solution by the coprecipitation of the iron salts.[48] The decrease of the saturation magnetization (M_S) with the reduction of the nanocrystal size is associated with the existence of a surface layer where the iron ions possess unsaturated coordination spheres. This is due to the absence of some oxygen ions from the spinel lattice and/or the capping of the nanoparticles with long chain carboxylate ligands which are bound directly to the iron ions. Such structural modifications create a surface spin disorder which induces significant changes in the magnetic properties of the nanocrystalline materials.[27, 39, 45, 49, 50] It was demonstrated that the nature of the capping ligand can also exert an important role on the magnetic properties of the nanoparticles. For example, Gao and coworkers showed that for Fe_3O_4 particles with similar sizes (8 nm) prepared by the solvothermal method, M_s increases from 89.8 emu/g_{Fe} to 96.6 emu/g_{Fe} when tri-*n*-octylphosphine oxide (TOPO) is used as capping ligand instead hexadecylamine (HDA).

Such an increase of the M_s value was attributed to the π-acceptor properties of the tri-*n*-octylphosphine oxide. Unlike the hexadecylamine, the TOPO molecules accept electrons from the iron ions once attached to the nanocrystals' surface, thus altering the exchange interactions between the neighboring iron ions and eventually leading to the decrease of the saturation magnetization of the Fe_3O_4 nanoparticles.[47]

Assuming that each nanoparticle consists of a magnetic core having the magnetic structure of the bulk material and a magnetically disordered shell, Chen and coworkers calculated the thickness of the shell (t) from the variation of the saturation magnetization (M_S) with the reciprocal of the average diameter (1/d) of the particles:[51]

$$M_S = M_{S(bulk)}\left(1 - \frac{6t}{d}\right)$$

The linear fitting of our data obtained at 30K (Fig. 4. 5) yielded a value for the saturation magnetization of the bulk material ($M_{S(bulk)}$) of 88.65 emu/g and a thickness of the magnetically inert layer (t) of 2.26 Å, whereas at 5K the calculated values were 98.18 emu/g ($M_{S(bulk)}$) and 1.92 Å (t), respectively. The t values obtained from our calculations for oleate-capped Fe_3O_4 nanocrystals are much smaller than those of 4.5 Å (at 20K)[29], 5 Å (at 5 K)[51] and 6 Å (at 300 K)[52] reported in the literature for nanosized $MnFe_2O_4$ particles prepared by other wet chemical methods (w/o microemulsion method and coprecipitation in aqueous solutions) or 10 Å (at 5K)[45] observed in the case of $CoFe_2O_4$ nanoparticles synthesized by co-precipitation in aqueous solution followed by calcination.

Additionally, the coercivity was found to decrease with increasing the volume of the Fe_3O_4 nanoparticles. Such a variation is in good agreement with the Stoner-Wolhfarth

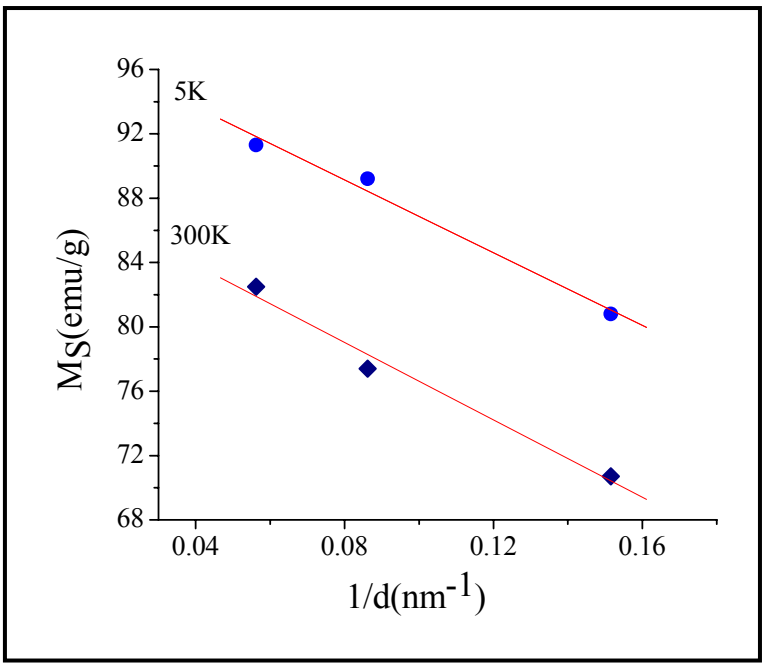

Figure 4.5. Saturation magnetization (M_S) *vs*. the reciprocal of the average diameter (1/d) of the oleate-capped Fe_3O_4 nanoparticles.

theory for single-domain particles with uniaxial anisotropy, which predicts that the coercivity (H_C) of the nanosized materials depends on both the anisotropy constant (K) and the saturation magnetization (M_S): $H_C = \frac{2K}{\mu_0 M_S}$, where μ_0 is the permeability constant of the vacuum.[53, 54] Thus, the decrease of the coercivity with increasing the size of the nanoparticles is consistent with both the decrease of the anisotropy constant and the increase of the saturation magnetization. The inset of the Figure 4.4b shows the hysteresis loops of the variable-sized Fe_3O_4 nanoparticles recorded at 5 K. In all cases the samples present a ferromagnetic behavior with the saturation magnetization (M_S) ranging from 80.8 to 91.3 emu/g and coercivities varying between 278.2 and 405.6 Oe. The values of the reduced remanence or squarness ($SQ=M_R/M_S$) calculated from the M(H) loops at 5K range between 0.25 and 0.29. They are considerable smaller than the theoretical value SQ=0.5 suggesting that the oleate-capped Fe_3O_4 nanoparticles are single-domain and possess a uniaxial anisotropy.[55]

In order to demonstrate the influence of the dipolar interparticle interactions on the magnetic properties of the oleate-capped Fe_3O_4 nanoparticles, DC magnetization measurements were performed on samples consisting of particles prepared from neat DEG (6.6 nm) and dispersed in paraffin. The concentration of the nanosized particles in the magnetite-paraffin solid solution was varied in a wide range (from 0.25 to 100 wt %), thus allowing us to tune the interparticle distances. In Figure 4.6 are plotted the typical temperature dependence magnetization curves measured in the ZFC mode under a static magnetic field of 100 Oe for different concentrations of the 6.6 nm Fe_3O_4 particles in the

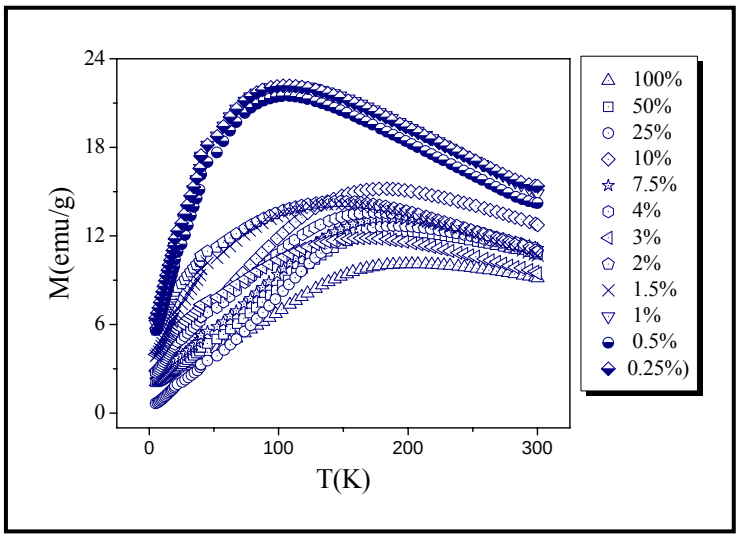

Figure 4. 6. Typical zero-field cooled (ZFC) curves of the 6.6 nm-sized Fe_3O_4 particles capped with oleate ligand and diluted in paraffin; the concentration of the nanoparticles in the magnetite-paraffin solid solution varies between 0.25 and 100 wt %.

paraffin matrix. As a general feature, the magnetization decreases with increasing the concentration of the nanosized particles. For example, the highest magnetization (M=22.2 emu/g) corresponds to the most diluted sample (c=0.25%), whereas the lowest value of magnetization (M=10.1 emu/g) was obtained for the sample containing bare Fe_3O_4 nanoparticles (c=100%). A similar trend was reported by El-Hilo *et al.* in the case of 10 nm Fe_3O_4 particles obtained by coprecipitation in aqueous medium and suspended in a liquid carrier.[56] However, for the intermediate concentrations, the magnetization does not increase regularly with the dilution, the results being analogous with those obtained by Vestal and coworkers for 8 nm-sized $MnFe_2O_4$ particles synthesized by the "seed-mediated growth" method and dispersed in eicosane.[57] Although the origin of these discrepancies was not completely elucidated, the variation of the magnetization with the dilution strongly suggests that the interactions between the nanoparticles play an important role in modifying the anisotropy energy barriers of the magnetic system.

In Figures 4.7(a) and (b) are displayed the variations of the blocking temperature (T_B) and coercivity (H_C) with the dilution in paraffin. As seen in the Figure 4.7(a), T_B decreases slightly from 203K to 183K as the particle concentration is decreased from 100 to 7. 5% and then drops sharply to a value of 108K as the concentration reaches 1%. After this abrupt decrease, the further reduction of the particle concentration to 0.25% does not change the value of the blocking temperature. Likewise, the coercivity decreases from 409 to 397 Oe in the same concentration range and then drops abruptly to 185 Oe for a concentration of 0.25% (Figure 4.7(b)). Such similarities in the variation pattern of both the blocking temperature and the coercivity with the particle concentration suggest that they have the same origin, that is, the interactions between nanoparticles.

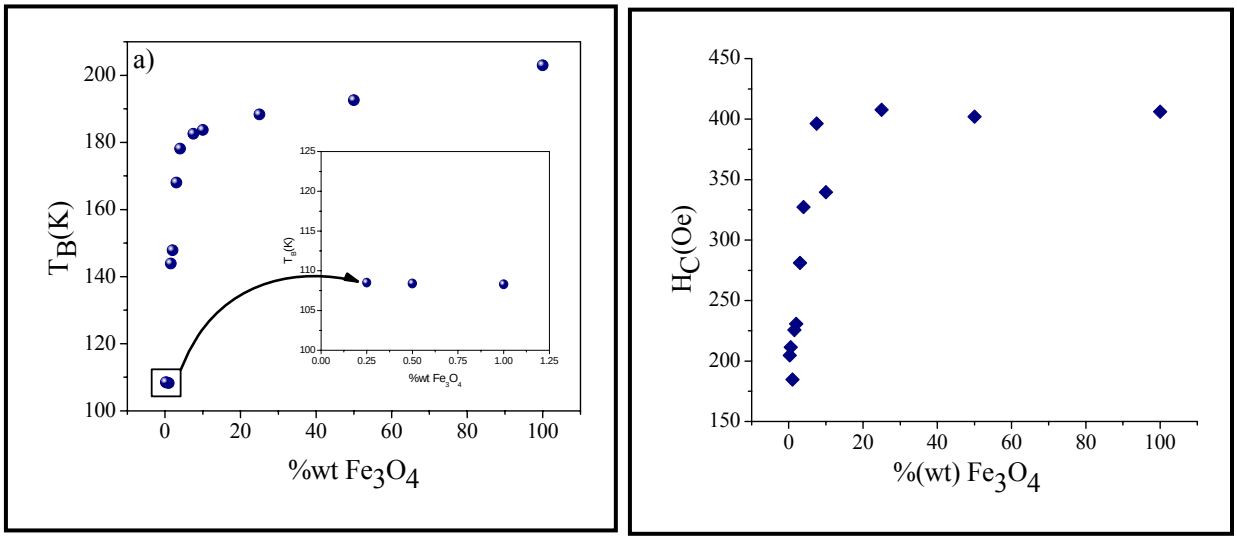

Figure 4.7. Variation of the blocking temperature (a) and coercivity (b) with the concentration of the 6.6 nm-sized Fe_3O_4 particles in the paraffin matrix.

This can be explained by the Dormann-Bessais-Fiorani (DBF) model which introduces an extra energy factor (B_i) in the expression of the anisotropy energy barrier (E_A) of a magnetic system with interparticle interactions:

$$E_A = KV \sin^2 \theta + B_i ,$$

where K represents the anisotropy constant, V is the volume of the magnetic particle, θ stands for the angle between the easy axis of the magnetic particle and the magnetization direction in an applied magnetic field, and B_i is an energy factor describing the interparticle interactions.[58, 59] Usually, the magnetostatic interactions between the particles include the exchange and the dipole-dipole interactions. However, when the nanocrystals' surface is functionalized with long-chain organic molecules the exchange couplings are minimized and, the energy factor B_i from the expression of the anisotropy energy barrier (E_A) is dominated by the dipolar interactions. For a magnetic system of single-domain particles, the energy corresponding to the dipole-dipole interactions can be expressed as: $E_{dipole-dipole} = -\frac{\mu_0 m_0^2}{4\pi d^3}$, where μ_0 represents the permeability constant of the vacuum and m_0 stands for the magnetic moment of the particle.[51] According to the above equation, the increase of the interparticle separation (d) induces the reduction of the strength of the dipolar interactions leading, eventually, to the decrease of the anisotropy energy barrier (E_A). In these conditions, the decrease of the blocking temperature and the coercivity with increasing the interparticle separation can be explained by the lowering of the anisotropy energy barriers when the concentration of the oleate-capped Fe_3O_4 particles in the paraffin matrix is reduced. Below a critical concentration (c=1%), the interparticle interactions become extremely weak so that a further decrease of the concentration to 0.25% will induce no variation in the value of the blocking temperature.

The M(H) curves of a sample containing 6.6 nm oleate-capped Fe_3O_4 particles dispersed in paraffin (c=1%) were measured at different temperatures ranging from 10 to 300 K (Figure 4.8(a)) and the values of the saturation magnetization (M_S) were determined. The variation of the high-field magnetization with the temperature for a ferro- or ferrimagnetic system can be described by the Bloch law:

$$M_S(T) = M_S(0)(1 - BT^{\alpha}),$$

where $M_S(0)$ is the saturation magnetization at 0K, B represents the Bloch constant and α stands for the Bloch exponent.[60, 61] The values of $M_S(0)$, B and α obtained by fitting the experimental data to the above equation (Figure 4.8(b)) are: 93.5 emu/g, $10^{-5}K^{-1.67}$ and 1.67, respectively. As a feature of the oleate-capped Fe_3O_4 nanoparticles, the Bloch exponent in the fitting equation is slightly larger than the value of 1.5 characteristic to the bulk crystalline material[62] and which was previously reported for 3.3 nm $CoFe_2O_4$ nanoparticles obtained by the same technique[43]. Such a deviation from the Bloch law was observed for various nanoparticulate oxides, where the exponent α increases with reducing the size of the nanoparticles.[51, 63] Furthermore, the wide range of values of the Bloch exponent was ascribed to the influence of various factors such as the high surface/volume ratio, the preparative route, the chemical composition of the nanoparticles, as well as their surface modification.[62] For example, Chen *et al.* suggested that in the case of the $MnFe_2O_4$ nanocrystals with sizes varying between 5 and 15 nm the values of the Bloch exponent fall within the range 1.6-2, whereas a value of 1.66 was reported for 12 nm $La_{0.8}Sr_{0.2}MnO_{3-\delta}$ nanoparticles obtained by a ball-milling process, which is substantially bigger than α=0.9 calculated by Xiong and coworkers for 8.1 nm $CoCrFeO_4$ nanoparticles prepared by a sol-gel approach.[51, 63, 64]

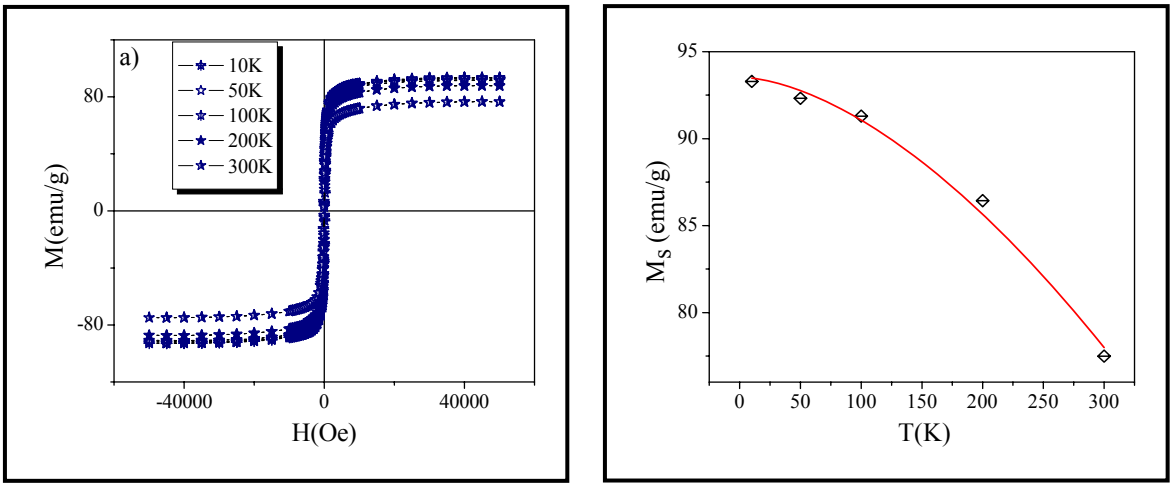

Figure 4.8. M(H) curves of the 6.6 nm-sized Fe_3O_4 particles dispersed in paraffin (c=1%) measured at different temperatures ranging from 10 to 300 K (a); the temperature dependence of the saturation magnetization.

4. 4. Conclusions

The magnetic properties of the variable-sized Fe_3O_4 nanoparticles prepared in non-aqueous homogeneous solutions of polyols were investigated by performing DC magnetization measurements at various temperatures and under different magnetic fields. Both finite size and interparticle interaction effects were identified to influence the magnetic behavior of the oleate-capped nanosized particles. At low temperatures the Fe_3O_4 nanocrystals exhibit a ferromagnetic behavior with blocking temperatures which increase with increasing the average particle size, whereas at room temperature, except for the largest nanoparticles (17.8 nm), they undergo a superparamagnetic relaxation. However, the 17.8 nm-sized particles are ferromagnetic at room temperature, their blocking temperature being higher than 300K.

The squarness values calculated from the corresponding magnetization curves indicate that the Fe_3O_4 nanoparticles possess a uniaxial anisotropy and their easy axes are randomly oriented. Both the anisotropy constant (K) and the coercivity (H_C) of the oleate-capped Fe_3O_4 nanoparticles were found to decrease with increasing their average size, whereas an opposite trend was observed for the saturation magnetization (M_S). Moreover, for all samples, the M_s values are slightly smaller than that of the bulk material, suggesting the existence of a disordered spin configuration on their surface. The thickness of the magnetically inert layer was estimated at 1.92 Å (5 K) from the size dependence of the magnetization. While the exchange interactions are minimized due to the protective layer of the capping ligand, the dipole-dipole interactions between the nanosized particles can be tuned by changing the interparticle distances. This could be achieved by dispersing the oleate-capped Fe_3O_4 nanoparticles in paraffin at different

concentrations ranging from 0.25 to 100 wt%. As the strength of the interactions decreases with dilution, the anisotropy energy barrier is substantially lowered, thereby inducing a drastic decrease of both the blocking temperatures and the coercivity with decreasing the concentration of the nanosized particles in the paraffin matrix.

4.5. References

1. West, A. R. *Basic Solid State Chemistry*; John Wiley & Sons Ltd.: 1984, p. 57
2. Smart, L.; Moore, E. *Solid State Chemistry: An Introduction*; Fong & Sons Printers Pte Ltd.: Singapore, 1992; p. 24
3. Makovec, D.; Košak, A.; Drofenik, M. *Nanotechnology* **2004**, *15*, S160.
4. Regan, B. O.; Gratzel, M. *Nature* **1991**, *353*, 737.
5. Makovec, D.; Košak, A.; Drofenik, M. *Nanotechnology* **2004**, *15*, S160.
6. McMichael, R. D.; Shull, R. D.; Swaertzendruber, L. J.; Bennett, L. H. *J. Magn. Magn. Mater.* **1992**, *111*, 29.
7. Shen, L.; Laibinis, P. E. ; Alan Hatton, T. *Langmuir*, **1999**, *15*(2), 447.
8. Chou, S. Y.; Wei, M. S.; Kraus, P. R.; Fischer, P. B. *J. Appl. Phys.* **1994**, *76*, 6673.
9. Raj, K.; Moskowitz, R. *J. Magn. Magn. Mater.* **1990**, *85*, 233.
10. Si, S.; Li, C.; Wang, X.; Yu, D.; Peng, Q.; Li, Y. *Crystal Growth & Design* **2005**, *5*(2), 391.
11. Koneracka, M.; Kopcansky, P.; Timko, M.; Ramchand, C. N.; de Sequeira, A.; Trevan, M. *J. Mol. Catal. B: Enzym.* **2002**, *18*, 13.
12. Ferreira, H. A.; Graham, D. L.; Freitas, P. P.; Cabral, J. M. S. *J. Appl. Phys*. **2003**, *93(10)*, 7281.

13. Cao, Y. C.; Jin, R.; Nam, J.; Thaxton, C. S.; Mirkin, C. A. *J. Am. Chem. Soc.* **2003**, *125*, 14676.

14. Manent, J.; Oguievetskaia, K.; Bayer, J.; Ratner, N.; Giovannini, M. *J. Neurosci. Methods* **2003**, *123*, 167.

15. Doyle, P. S.; Bibette, J.; Bancaud, A.; Viovy, J. L. *Science* **2002**, *295*, 2237.

16. Kim, D. K.; Mikhaylova, M.; Wang, F. H.; Kehr, J.; Bjelke, B.; Zhang, Y.; Tsakalakos, T.; Mamoun, M. *Chem. Mater.* **2003,** *15,* 4343.

17. Babes, L.; Denizot, B.; Tanguy, G.; Le Jeune, J. J.; Jalet, P. *J. Colloid Interface Sci*. **1999**, *212,* 474.

18. Papisov, M. I.; Bogdanov, A., Jr.; Schaffer, B.; Nossiff, N.; Shen, T.; Weissleder, R.; Brady, T. J. *J. Magn. Magn. Mater*. **1993**, *122*, 383.

19. Jordan, A.; Scholtz, R.; Wust, P.; Schbirra, H.; Schiesel, T.; Schmidt, H.; Felix, R. *J. Magn. Magn. Mater*. **1999**, *194*, 185.

20. Wunderbaldinger, P.; Josephson, L.; Weissleder, R. *Bioconjugate Chem*. **2002**, *13*, 264.

21. Gupta, P. K.; Hung, C. T.; Lam, F. C.; Perrier, D. G. *Int. J. Pharm.* **1988**, *43*, 167.

22. Alexiou, C.; Arnold, W.; Klein, R. J.; Parak, F. G.; Hulin, P.; Bergemann, C.; Erhardt, W.; Wagenpfeil, S.; Lubbe, A. S. *Cancer Res.* **2000**, *60*, 6641.

23. Jain, T. K.; Morales, M. A.; Sahoo, K. S.; Leslie-Pelecky, D. L.;Labhasetwar, V. *Molec. Pharm*. **2005**, *2(3)*, 194.

24. Ibrahim, A.; Couvreur, P.; Roland, M.; Speiser, P. *J. Pharm. Pharmacol.* **1982**, *35*, 59.

25. Awschalom, D. D.; DiVencenzo, D. P. *Phys. Today* **1995**, *48*(4), 43.

26. Si, S.; Kotal, A.; Mandal, T. K.; Giri, S.; Nakamura, H.; Kohara, T. *Chem. Mater.* **2004**, *16*(18), 3489.

27. Kodama, R. H.; Berkowitz, A. E.; McNiff, E. J.; Foner, S. *J. Appl. Phys.* **1997**, *81*(8), 5552.

28. Morales, M. P.; Veintemillas-Verdaguer, S.; Montero, M. I.; Serna, C. J.; Roig, A.; Casas, Ll.; Martínez, B.; Sandiumenge, F. *Chem. Mater.* **1999**, *11*(11), 3058.

29. Liu, C.; Zhang, Z. J.; *Chem. Mater.* **2001**, *13* (6), 2092.

30. Sorensen, C. M. in *Nanoscale Materials in Chemistry*; Klabunde, K. J., Ed.; Wiley: New York, 2002, p.169.

31. Caruntu, D.; Remond, Y.; Chou, N. H.; Jun, M. J.; Caruntu, G.; He, J.; Goloverda G.; O'Connor, C. J.; Kolesnichenko, V. *Inorg. Chem.* **2002**, *41*, 6137.

32. Caruntu, D.; Caruntu, G.; Chen, Y.; Goloverda, G.; O'Connor C. J.; Kolesnichenko, V. *Chem. Mater.* **2004**, *16*, 5527.

33. Djurberg, C.; Svedlindh, P.; Nordblad, P.; Hansen, M. F.; Bødker, F.; Mørup, S. *Phys. Rev. Lett.* **1997**, *79*(25), 5154.

34. Jonsson, T.; Nordblad, P.; Svedlindh, P. *Phys. Rev. B* **1998**, *57*(1), 497.

35. del Barco, E.; Asenjo, J.; Zhang, X. X; Pieczynski, R.; Julìa, A.; Tejada, J.; Ziolo, R. F.; Fiorani, D.; Testa, A. M. *Chem. Mater.* **2001**, *13*(5), 1487.

36. Suber, L.; Imperatori, P.; Ausanio, G.; Fabbri, F.; Hofmeister, H. *J. Phys. Chem. B*

2005, *109*(15), 2005.

37. Ma, M.; Wu, Y.; Zhou, J.; Sun, Y.; Zhang, Y.; Gu, N. *J. Magn. Magn. Mater.* **2004**, *268*, 33.

38. Morup, S.; Topsoe, H. *J. Appl. Phys.* **1976**, *11*, 63.

39. Lee, Y.; Lee, J.; Bae, C. J.; Park, J.-G.; Noh, H.-J.; Park, J.-H.; Hyeon, T. *Adv. Funct. Mater.* **2005**, *15*(3), 503.

40. Tung, L. D.; Kolesnichenko, V.; Caruntu, G.; Caruntu, D.; Remond, Y.; Golub, V. O.; O'Connor, C. J.; Spinu, L. *Physica B*, **2002**, *319*, 116.

41. Yokoyama, M.; Ohta, E.; Sato, T.; Sato, T. *J. Magn. Magn. Mater.* **1998**, *183*, 173.

42. Park, J.; An, K.; Hwang, Y.; Park, J.-G.; Noh, H.-J.; Kim, J.-Y.; Park, J.-H.; Hwang, N.-M.; Hyeon, T. *Nature Mater.* **2004**, *3*, 891.

43. Charles, S. W.; Popplewell, J. in *Ferromagnetic Materials*; Wohlfarth, H., Ed.; North-Holland Publishing: Amsterdam, 1982; vol.2.

44. Kommareddi, N. S.; Tata, M.; John, V. T.; McPherson, G. L.; Lee, Y.-S.; O'Connor, C. J.; Akkara, J. A.; Kaplan, D. L. *Chem. Mater.* **1996**, *8*(3), 801.

45. Grigorova, M.; Blythe, H. J.; Blaskov, V.; Rusanov, V.; Petkov, V.; Masheva, V.; Nihtianova, D.; Martinez, Ll. M.; Muñoz, J. S.; Mikhov, M. *J. Magn. Magn. Mater.* **1998**, *183*, 163.

46. Sun, S.; Zeng, H.; Robinson, D. B.; Raoux, S.; Rice, P. M.; Wang, S. X.; Li, G. *J. Am. Chem. Soc.* **2004**, *126*(1), 273.

47. Hou, Y.; Yu, J.; Gao, S. *J. Mater. Chem.* **2003**, *13*, 1983.

48. Gee, S. H.; Hong, Y. K.; Erickson, D. W. Park, M. H.; Sur, J. C. *J. Appl. Phys.* **2003**,

93(10), 7560.

49. Vestal, C. R.; Zhang, Z. J. *Int. J. Nanotechnology* **2004**, *1*(1/2), 240.
50. Tung, L.D.; Kolesnichenko, V.; Caruntu, D.; Chou, N. H.; O'Connor, C., J.; Spinu, L. *J. Appl. Phys.* **2003**, *93*(10), 7486.
51. Chen, J. P.; Sorensen, C. M.; Klabunde, K. J.; Hadjipanayis, G. C.; Devlin, E.; Kostikas, A. *Phys. Rev. B* **1996**, *54*(13), 9288.
52. Zheng, M.; Wu, X. C.; Zou, B. S.; Wang, Y. J. *J. Magn. Magn. Mater.* **1998**, *183*, 152.
53. McCurrie, R. A. *Ferromagnetic Materials-Structure and Properties*; Academic Press: London, 1994; p16.
54. Vestal, C. R.; Zhang, Z. J. *Chem. Mater*. **2002**, *14*(9), 3817.
55. Stoner, E. C.; Wohlfarth, E. P. *Phil. Trans. R. Soc.* **1948**, *A240*, 559.
56. El-Hilo, M.; O'Grady, K.; Chantrell, R. W. *J. Magn. Magn. Mater.* **1992**, 114, 295.
57. Vestal, C. R.; Song, Q.; Zhang, Z. J. *J. Phys. Chem. B* **2004**, *108*(47), 18222.
58. Frankamp, B. L.; Boal, A. K.; Tuominen, M. T.; Rotello, V. M. *J. Am. Chem. Soc.* **2005**, *127*(27), 9731.
59. Dormann, J. L.; Fiorani, D.; Tronc, E. *J. Magn. Magn. Mater.* **1999**, *202*, 251.
60. Balzar, D.; Ledbetter, H. *J. Appl. Crystallogr.* **1993**, *26*, 97.
61. Bloch, F. *Z. Phys.* **1931**, *61*, 206.
62. Hochepied, J. F.; Bonville, P.; Pileni, M. P. *J. Phys. Chem. B* **2000**, *104*(5), 905.
63. Roy, S.; Dubenko, I.; Edorh, D. D.; Ali, N. *J. Appl. Phys.* **2004**, *96*(2), 1202.
64. Xiong, G.; Mai, Z.; Xu, M.; Cui, S. *Chem. Mater.* **2001**, *13*(6), 1943.

CHAPTER 5

Attachment of Gold Nanograins onto Colloidal Magnetite Nanocrystals

5.1 Introduction

In the last few years, magnetite nanoparticles have become increasingly important for cutting-edge applications in biomedicine due to both their biocompatibility and attractive magnetic properties.[1] Superparamagnetic magnetite nanocrystals possess high magnetic susceptibility, low remanence, low coercivity and high saturation magnetization, making them ideal candidates for applications in magnetic resonance imaging (MRI), cancer/HIV diagnosis, magnetically-controlled drug delivery, biological separation, enzyme and protein immobilization, magnetic cell sorting, RNA and DNA purification, retinal detachment therapy, biosensors and magnetocytolysis.[2-7] Additionally, although nanocrystalline Fe_3O_4 presents a lower saturation magnetization than its metallic congeners, it exhibits a much higher chemical stability against oxidation, which enables magnetite nanocrystals to be easily dispersed in blood and directed to a specific target upon applying an external magnetic field.

For high-performance applications, magnetite nanoparticles are required to possess a narrow size distribution, smooth surface, uniformity of the spherical shape and the ability to form colloidal suspensions in physiological fluids. This last condition has proven to be a critical shortcoming for practical applications because magnetic particles have the tendency to cluster and precipitate, which drastically reduce their efficiency. Advanced manipulation of magnetite nanoparticles for *in-vivo* diagnostic tests necessitates magnetic

nanoparticles conjugated with bioactive molecules such as antibodies, nucleic acids, lipids, peptides, enzymes, proteins or DNA. Biomolecule immobilization often requires chemical modification of the surface by complicated synthetic procedures.[8] This could be greatly simplified by coating magnetite nanoparticles with metallic nanoshells. Gold represents an excellent candidate by virtue of its easy reductive preparation, high chemical stability, biocompatibility, and its affinity for binding to amine/thiol terminal groups of organic molecules.[9] Ideally, gold nanoshells should be thin enough to induce minimal alteration of the magnetic properties of the magnetite core. Several recent papers have reported the synthesis of core-shell Fe_3O_4@Au nanocomposites, but, in most cases, the coating of individual magnetite nanoparticles and the tunability of the shell-thickness still remain unresolved.[10, 11]

Here, we report a facile, highly reproductive two-step synthetic process enabling the attachment of 2-3 nm gold clusters onto (3-aminopropyl)triethoxysilane (APTES)-coated Fe_3O_4 nanoparticles obtained by functionalization of Fe_3O_4 particles with a mean diameter of 10.5 nm (Scheme 5.1). This work exploits the strong ability of gold metal to bind covalently to the lone pair of the terminal $–NH_2$ groups of organic entities, interactions that can be further enhanced by mutually attractive electrostatic interactions when the two components are oppositely charged. Though such a method has proven to be simple, inexpensive and versatile, little emphasis has been placed on the design of nanocomposite architectures with tailorable properties and complex functionalities by the immobilization of metal nanoclusters onto different kinds of nanoparticles.

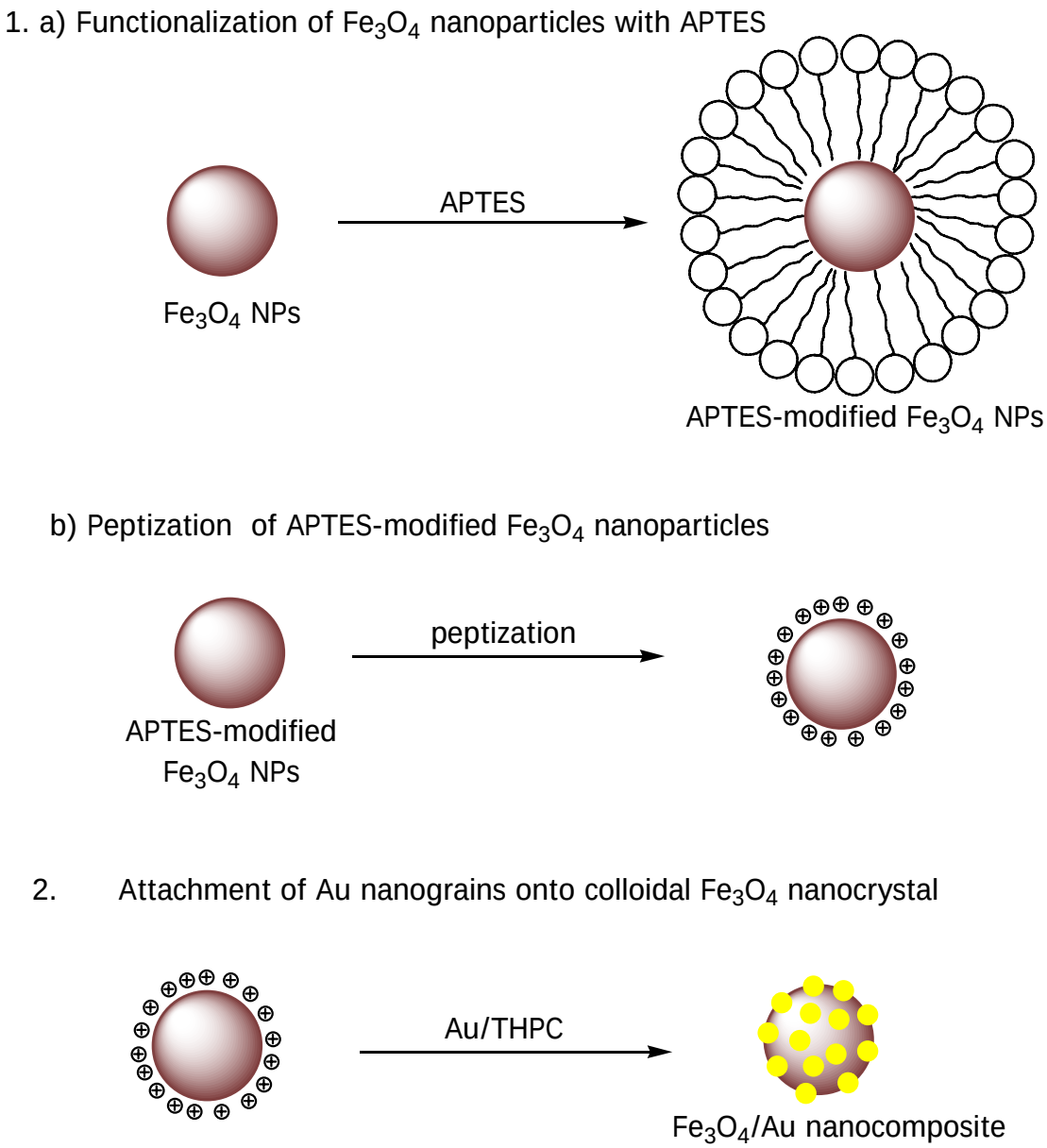

Scheme 5.1. Synthetic approach to the attachment of Au nanograins onto colloidal Fe_3O_4 nanoparticles; APTES is (3-aminopropyl)triethoxysilane and THPC is tetrakis(hydroxymethyl)phosphonium chloride.

Previous attempts include the work of Halas and coworkers, who designed a bottom-up approach for the preparation of core-shell SiO_2@Au nanocomposites by the sequential attachment of gold nanoparticles to the surface-modified SiO_2 nanocrystals.[12] The growth of these attached gold nanoparticles by a subsequent reduction of Au^{3+} in aqueous solutions finally results in the formation of a continuous thin gold layer at the surface of the SiO_2 nanocrystals. Recently, Sun and coworkers have reported the preparation of dumbbell-like bifunctional Au-Fe_3O_4 nanocomposites by the thermal decomposition of $Fe(CO)_5$ at 300^oC in presence of Au nanoparticles dispersed into a noncoordinating solvent and an inert atmosphere[13]. Additionally, all the other related papers cover extensively the immobilization of noble metals onto different bare/surface-functionalized inorganic nanocrystals having applications in optical devices and catalysis.[14-17] Though Fe_3O_4/Au nanocomposites represent a relevant system with superior magnetic properties and potential widespread use in biomagnetics, such composites have been largely ignored in favor of Fe_3O_4@Au core-shell nanostructures.

5.2 Experimental

5.2.1 Synthesis of the magnetic nanoparticles

Highly crystalline magnetite nanoparticles were prepared by the hydrolysis of chelated iron alkoxide complexes at elevated temperature in solutions of diethylene glycol (DEG) and *N*-methyl diethanolamine (NMDEA) (3:1, w/w). In a typical experiment, a 4 mmol amount of $FeCl_2 \cdot 4H_2O$ and 8mmol of $FeCl_3 \cdot 6H_2O$ were dissolved in 120 g of diethylene glycol (DEG) in a Schlenk flask under protection with argon.

When the salts were completely dissolved, 40 g of NMDEA was added and the solution immediately turned from yellow-brown to deep brown-green. The resulting solution was allowed to stir for 1h. Separately, 32 mmol of NaOH was dissolved in 60 g of DEG and then mixed with 20 g NMDEA. The solution of NaOH was added to the solution of metal chlorides while stirring at room temperature, causing an immediate color change from deep brown-green to deep green. After 3 h, the temperature of the solution was raised during 1.5 h to 210°C and then kept constant for 3 h in the temperature range of 210-220°C. After cooling the reaction mixture to room temperature, the obtained black solid was isolated by centrifugation, washed with a mixture of ethanol and ethyl acetate (1:1, v/v) three times and then dispersed in methanol.

As shown in the chapter 3, the surface of the as-prepared Fe_3O_4 nanocrystals are passivated by the molecules of the adsorbed solvents (DEG and NMDEA), which bind the superficial Fe ions via the ligand's lone pairs, thus rendering the nanoparticles soluble in polar solvents (water, methanol, and ethanol).[18] Furthermore, organic molecules such as DEG and NMDEA are known to possess the ability to act as tridentate ligands for a transition metal ion, forming two-ring, chelating complexes.[19] Although the mechanistic pathway of the bonding of these organic molecules to the oxide nanocrystals' surface is not completely elucidated, it is likely that when adsorbed on the surface, these molecules partially use their chelating properties and leave some of the hydroxo groups available for further derivatization.

5.2.2 Synthesis of the Fe_3O_4/ Au nanocomposites

For the synthesis of the nanocomposite material, we used colloidal solutions of Fe_3O_4 nanoparticles in methanol that exhibit long sedimentation times, being stable against agglomeration for several months. The first step of the synthetic process consists of functionalizing the Fe_3O_4 nanocrystals with 3-aminopropyltriethoxysilane (APTES). Recently, two independent papers reported the functionalization with APTES of magnetite nanoparticles obtained by co-precipitation of Fe^{2+} and Fe^{3+} salts in aqueous solution.[20-21] The authors demonstrated that the hydroxy groups on the magnetite surface react with the ethoxy groups of the APTES molecules with the formation of Si-O bonds and leave the terminal $–NH_2$ groups available for enzyme immobilization.[21] However, in both cases the APTES functionalization of individual Fe_3O_4 nanoparticles is hampered by the relatively high agglomeration level of the co-precipitated nanopowders. In contrast to the co-precipitation procedure, our non-aqueous synthetic approach allows the two chelating solvents (DEG and NMDEA) to protect the nanocrystals against agglomeration, induce their solubility in polar solvents, and favor the reactions at the nanocrystal's surface, thus rendering them more suitable for individual functionalization with organic molecules. For the functionalization of Fe_3O_4 nanocrystals with 3-aminopropyltriethoxysilane (APTES), 2 mL of ferrofluid (~10 mg Fe_3O_4/mL methanol solution) was diluted to 50 mL with absolute ethanol and sonicated for 2-3 min. The resulting colloidal solution was transferred to a three-neck flask equipped with a condenser, a thermometer, and a heating mantle. Then, 180 μL APTES was injected into the flask and the mixture was vigorously stirred at room temperature for about 1 h and

then heated to reflux for 2 h under protection with argon. After cooling the mixture to room temperature, the solid product was magnetically separated, washed with ethanol five times and then redispersed in 10 mL of ethanol by sonicating for 10 min. In order to induce positive charges at the surface of the APTES-coated Fe_3O_4 nanocrystals, 10 drops of HNO_3 solution (prepared by mixing 0.05 mL of 6 M HNO_3 with 20 mL ethanol) was introduced into the ethanolic dispersion of APTES-coated Fe_3O_4 and then stirred for 4 h. The second step in the synthesis of Fe_3O_4/Au nanocomposites is the attachment 3 nm gold particles onto APTES-coated Fe_3O_4 nanoparticles. Negatively charged gold nanoparticles were prepared by a modification of the method of Duff *et* al.[22] In a typical experiment, a volume of 5 mL of 1 M NaOH was diluted with 18 mL of distilled water and then mixed with 10 mL of tetrakis(hydroxymethyl)phosphonium chloride (THPC) (0.67 mmol) solution. The THPC stock solution was prepared separately by diluting 0.6 mL of 80% THPC (3.375 mmol) aqueous solution with 50 mL distilled water. The resulting solution containing the reducing agent was allowed to stir for 5 min. Then, 20 mL of 1% $HAuCl_4$ solution was added slowly to the above mixture kept under vigorous stirring to yield a deep red-brown solution indicating the formation of Au nanoparticles. The resulting colloidal gold solution was stirred continuously for 10 min. Once prepared, the negatively charged gold nanoparticles contained in the colloidal solution were attached to the surface of aminosilane-coated Fe_3O_4 nanocrystals. Thus, 30 mL of colloidal gold solution was introduced into a round bottom flask containing 10 mL of the ethanolic dispersion of amine-functionalized Fe_3O_4 nanoparticles and the mixture was stirred overnight at room temperature. The solid product was collected by magnetic separation, washed in sequence with ethanol and distilled water five times to remove the

excess of gold particles, and then redispersed in ethanol by sonication. From these solutions, samples for the XRD and magnetic measurements were prepared by drying the solid material at room temperature under flowing nitrogen.

5.3. Characterization of the Fe_3O_4/ Au composite nanopowders

Figure 5.1 shows the transmission electron microscopy (TEM) images of (a) the Fe_3O_4 nanoparticles obtained from a mixture of DEG and NMDEA (3:1, w/w), (b) the colloidal gold particles, (c) the as-prepared Fe_3O_4/Au nanocomposite material, and (d, e) and (f, g) the ethanolic dispersion of Fe_3O_4/Au nanocomposites aged for two and seven months, respectively and sonicated for 60 minutes. The micrographs clearly show that the attachment of gold nanoparticles to individual Fe_3O_4 nanocrystals was successful. However, as seen in Fig. 5.1 (c), some agglomeration of the Fe_3O_4/Au nanocomposites is observed, but the initial spherical Fe_3O_4 nanoparticles can still be individually distinguished. We observe that the parent Fe_3O_4 nanoparticles are slightly aggregated, most of them appearing as discrete units which exhibit individual spherical shapes. At the same time, the Fe_3O_4/Au nanosized composites show a remarkable resistance to sonication; most of the gold particles are still attached onto the surface of Fe_3O_4 nanocrystals even after sonication for 1 h. While the attaching mechanism is still unclear, TEM data suggest that the bonding of colloidal gold nanoparticles to the surface of APTES-modified Fe_3O_4 nanoparticles is relatively strong and probably not strictly electrostatic. From the HRTEM image (Fig. 5.2), one can easily identify the 2-3 nm gold

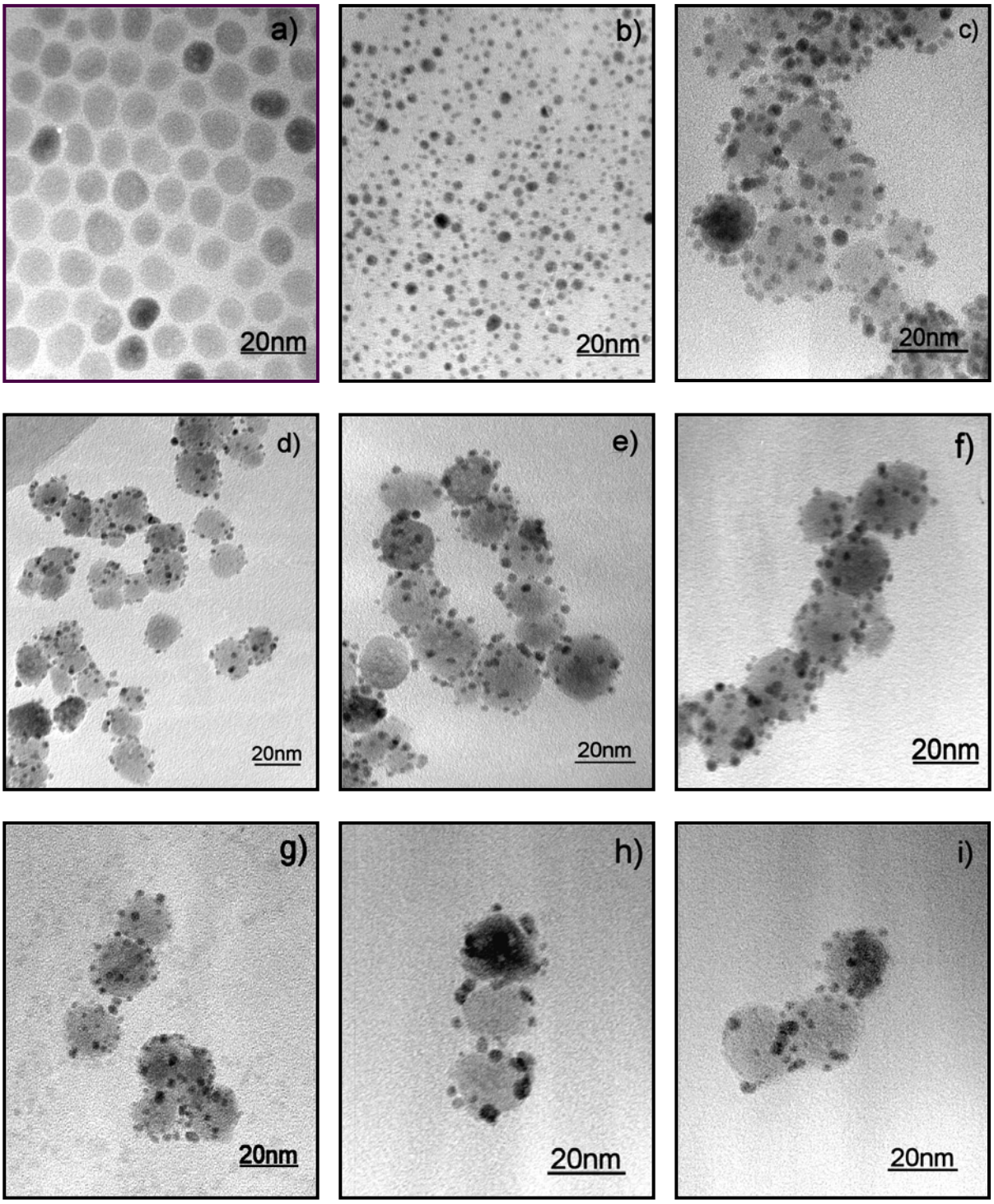

Figure 5.1. Typical TEM images of the as-prepared Fe_3O_4 nanoparticles obtained from a mixture of DEG and NMDEA (3:1, w/w) (a), the colloidal Au particles (b), the freshly prepared Fe_3O_4/Au nanocomposite material (c), and the Fe_3O_4/Au nanocomposite material aged for 2 (d, e), 5 (f, g), and 7months (h, i) and sonicated for 60 minutes.

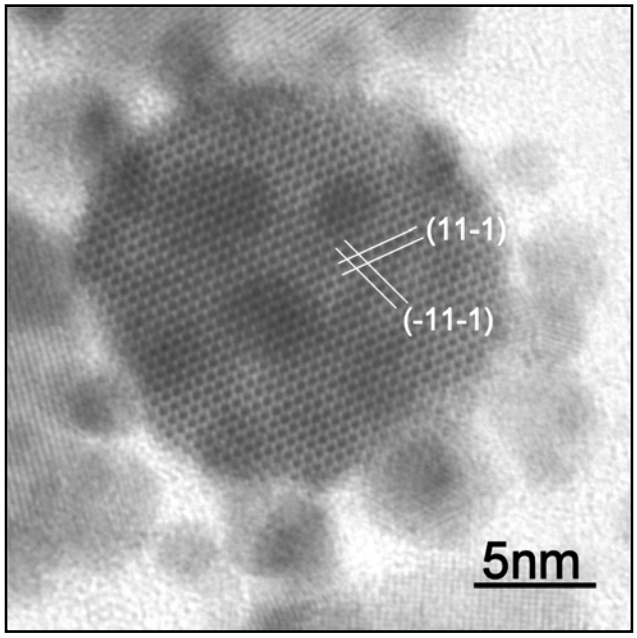

Figure 5.2. Representative high resolution TEM image of a typical Au-decorated Fe_3O_4 nanocrystal viewed along [011] zone axis.

particles (smaller, darker dots) attached to spherical ~10 nm Fe_3O_4 nanocrystals. Because of their small size, the lattice fringes of the 2-3 nm attached gold particles cannot be distinguished, whereas for the larger Fe_3O_4 nanocrystals, lattice fringes corresponding to the (11-1) and (-1 1 -1) atomic planes are easily identified. The interplanar distance calculated from the corresponding HRTEM image is 4.85Å, whereas the zone axis is [011]. Although the number of gold particles attached to each individual Fe_3O_4 nanocrystal varies between neighboring particles, no uncoated magnetite nanocrystals were observed.

From the X-ray powder diffraction (XRD) pattern in Figure 5.3, all reflections can be ascribed to nanocrystalline Fe_3O_4, whereas the most intense reflection of Au, specifically the (111), is identified by a broad, low-intensity peak centered at 38 $^{o}2\theta$. The absence of individual peaks corresponding to gold is likely due to the low concentration of gold in the composite material, the very small size of the gold particles and/or their amorphous nature resulting from reduction of the $AuCl_4^-$ ions in the presence of THPC. The small amount of gold attached to the magnetite nanoparticles was further confirmed by inductive coupled plasma (ICP) spectroscopy, which gave a weight percentage of 43.67% Fe_3O_4, 8.31% Si and 48.01% Au, respectively. Figure 5.4(a). illustrates the UV-vis spectra of the freshly prepared gold nanoparticles dispersed in water and ethanol, as well as the spectrum of an ethanolic dispersion of Fe_3O_4/Au nanocomposites. When dispersed in water, the as-prepared colloidal gold nanoparticles exhibit a plasmon peak at 515 nm that is shifted to 537 nm when the gold nanoparticles are dispersed in ethanol. The characteristic gold plasmon peak was not observed in the Fe_3O_4/Au nanocomposite. We hypothesize that the absence of the plasmon peak is due to both the low concentration

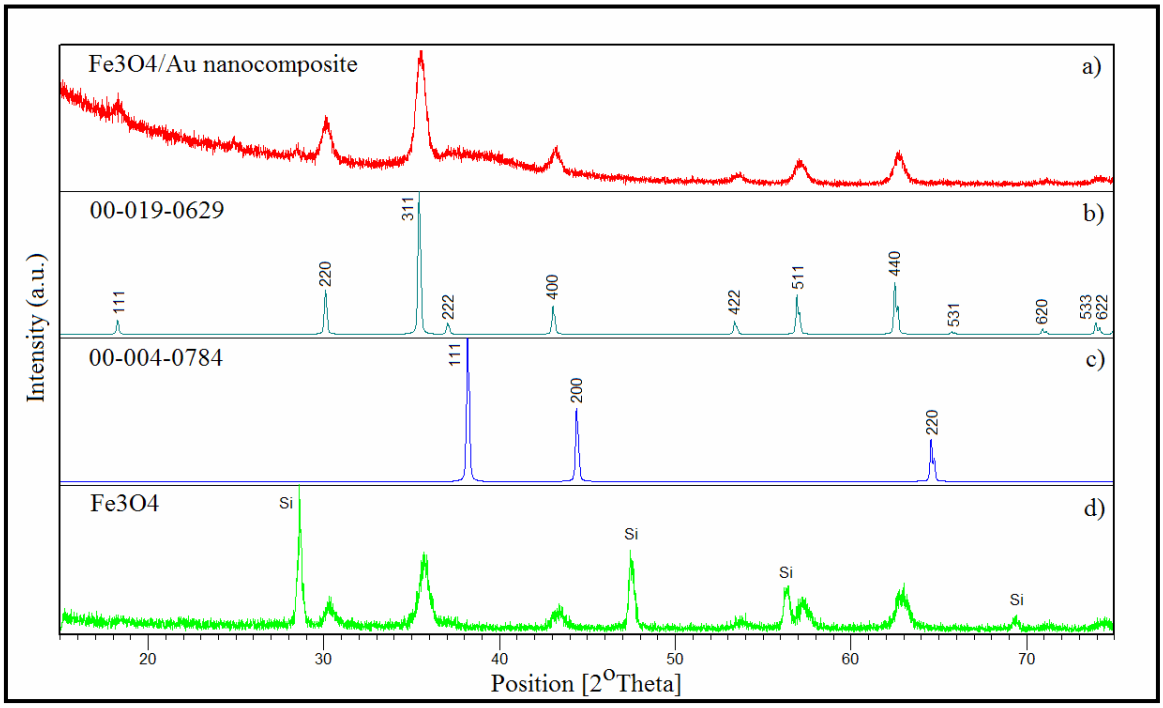

Figure 5.3. XRD pattern of the Fe_3O_4/Au nanocomposite (a) with simulated reference patterns of magnetite (b) and gold (c), and the Fe_3O_4 nanoparticles prepared from a mixture of DEG and NMDEA (3:1, w/w).

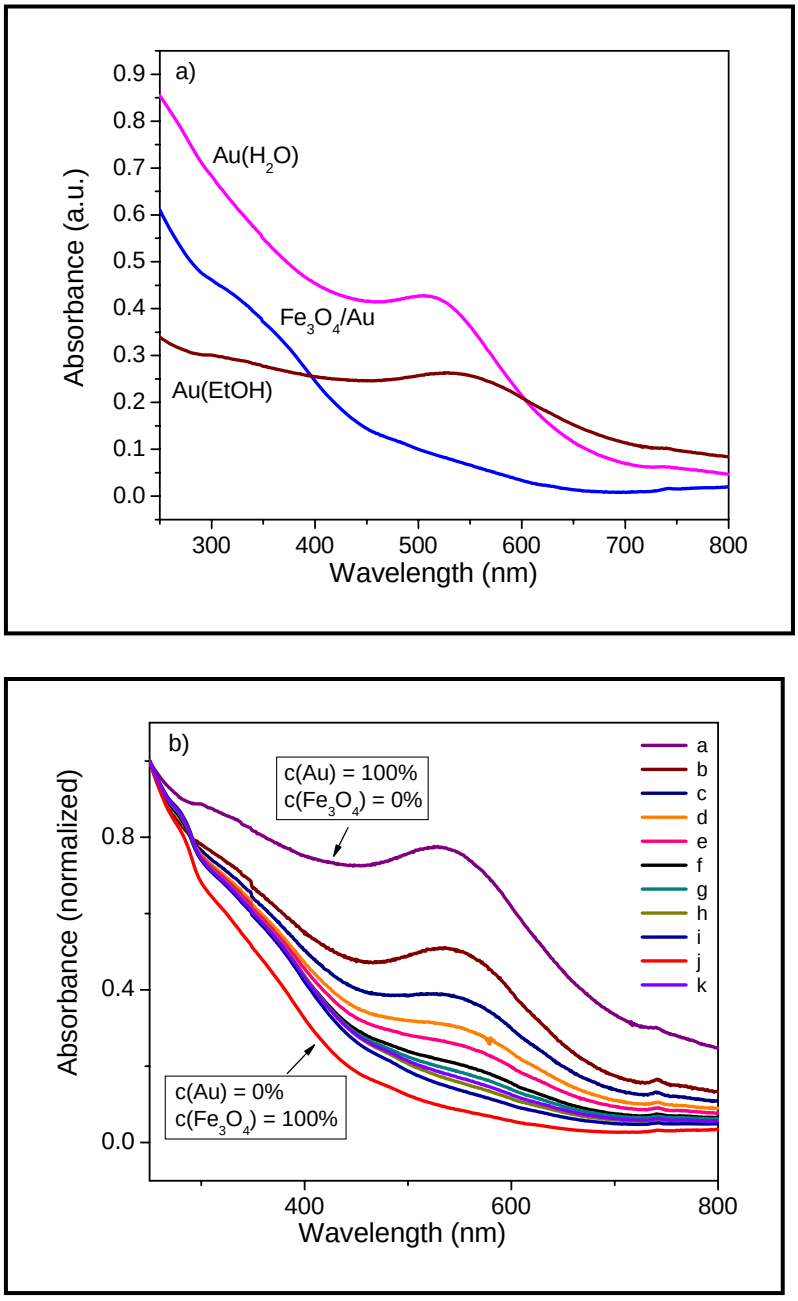

Figure 5.4. UV-vis spectra of the Fe_3O_4/Au nanocomposite material (a) and physical mixtures of colloidal Au nanoparticles and Fe_3O_4 nanocrystals dispersed in ethanol (b).

of gold particles in the composite material and their small size. The influence of the gold concentration on the intensity of the gold plasmon peak was investigated by recording the UV-vis spectra of physical mixtures of ethanolic dispersions of Fe_3O_4 nanocrystals and gold nanoparticles (Figure 5.4(b)). The intensity of the plasmon absorption peak at 537 nm (typical for THPC gold nanoparticles dispersed in ethanol) decreases monotonically as the concentration of gold in the physical mixture decreases. The curves (*a*) *to* (k) differ by 10% increments of the Au concentration from 100% (curve (*a*)) to 0% (curve (k)). Interestingly, we observed that the immobilization of the gold nanoparticles onto the Fe_3O_4 nanocrystals is size-selective. Careful examination of TEM micrographs reveals that the as-prepared gold nanoparticles exhibit a relatively broad size distribution, with sizes ranging between 2 and 7 nm in diameter, whereas the gold nanoparticles immobilized onto the Fe_3O_4 nanocrystals are significantly smaller, ranging between 1 and 4 nm (Figure 5.5). Fitting the size distribution profiles with a Gaussian function gives an average particle size of 3.4 nm (SD = 0.7) for the as-prepared Au nanoparticles and 2.5 nm (SD = 0.6) for the gold in the composite material. This strongly suggests that size effects play an important role in the formation of the Fe_3O_4/Au nanocomposites and that the ~10 nm APTES-coated Fe_3O_4 nanocrystals preferentially bind smaller gold nanoparticles. Consequently, the plasmon peak observed in the UV-vis spectra of both the aqueous and ethanolic gold colloids is attributed to the larger gold nanoparticles, whereas the Fe_3O_4/Au nanocomposites produce a plasmonless UV-vis spectrum. This observation agrees with the suggestion of other authors that for a collection of very small gold nanoparticles ($d<3$ nm), finite-size effects become significant, thus suppressing the characteristic plasmon peak in the corresponding UV-vis spectrum (since the main

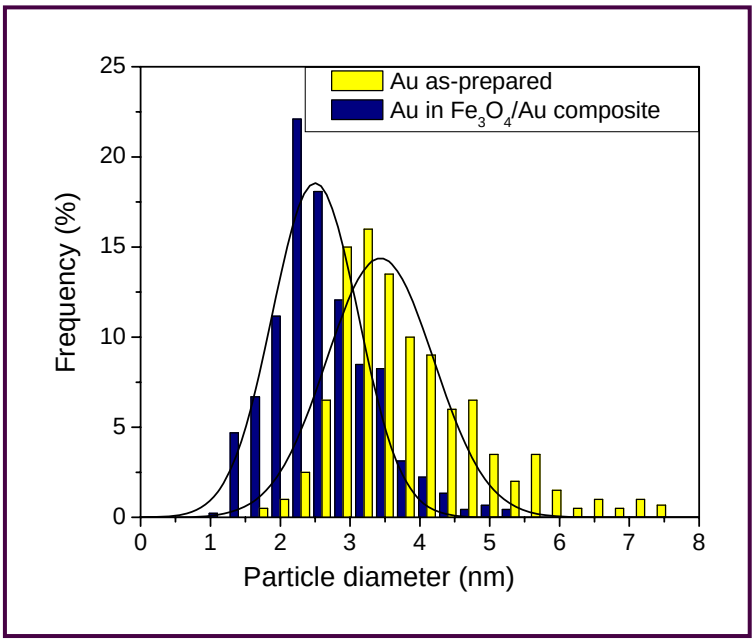

Figure 5.5. Size distribution plots of the as-prepared Au nanoparticles and Au nanoparticles immobilized onto 10.5 nm-sized Fe_3O_4 nanocrystals. Solid lines represent the fitted Gaussian distribution functions.

contribution to the plasmon peak mainly originates from the surface scattering of the conduction electrons, its intensity follows a 1/r dependence with the size of the particle).[23]

5.4. Magnetic properties of the Fe_3O_4/ Au composite nanopowders

The ZFC/FC curves of the gold-decorated Fe_3O_4 nanoparticles and the as-prepared Fe_3O_4 nanoparticles measured in a field of 100 Oe on a superconducting quantum interference device (SQUID) magnetometer are plotted in Figure 5.6. The absence of a well-defined maximum in the ZFC curve indicates that both the as-prepared 10.5 nm-sized Fe_3O_4 nanoparticles and Fe_3O_4/Au nanocomposites exhibit blocking temperatures (T_B) above room temperature. Furthermore, no visible difference between the two curves was detected upon immobilization of 2-3 nm gold particles onto the ~10 nm Fe_3O_4 particles. It is known that the maximum of the ZFC curve for a collection of superparamagnetic non-interacting single-domain nanoparticles is dependent on the size of nanocrystals, their degree of clustering, as well as on the mutual dipolar interactions between them.[24] However, in the case of Fe_3O_4/Au nanocomposites, the ZFC and FC curves diverge at T = 198 K, which is a much lower temperature than the T = 228 K observed in the case of the as-prepared Fe_3O_4 nanoparticles. This could be associated with a lowering of the anisotropic energy barrier for the Fe_3O_4/Au nanocomposites with respect to that of the as-prepared Fe_3O_4 nanocrystals.The hysteresis loops of the as-prepared Fe_3O_4 nanoparticles and Fe_3O_4/Au nanocomposites, recorded at 300 K and 5 K, are represented in Figure 5.7. As expected from the shape of the ZFC/FC curves, the

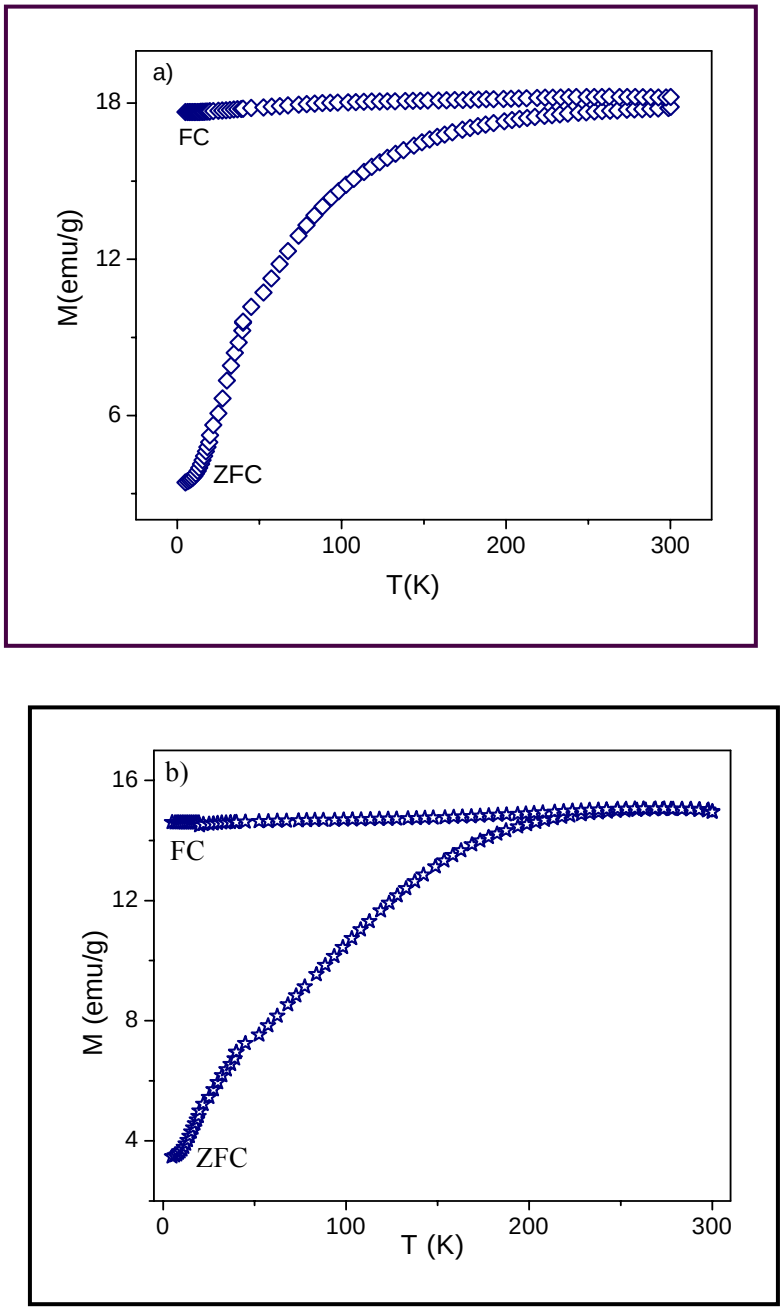

Figure 5.6. ZFC/FC curves of the as-prepared Fe_3O_4 nanoparticles (a), and Fe_3O_4/Au nanocomposite material (b).

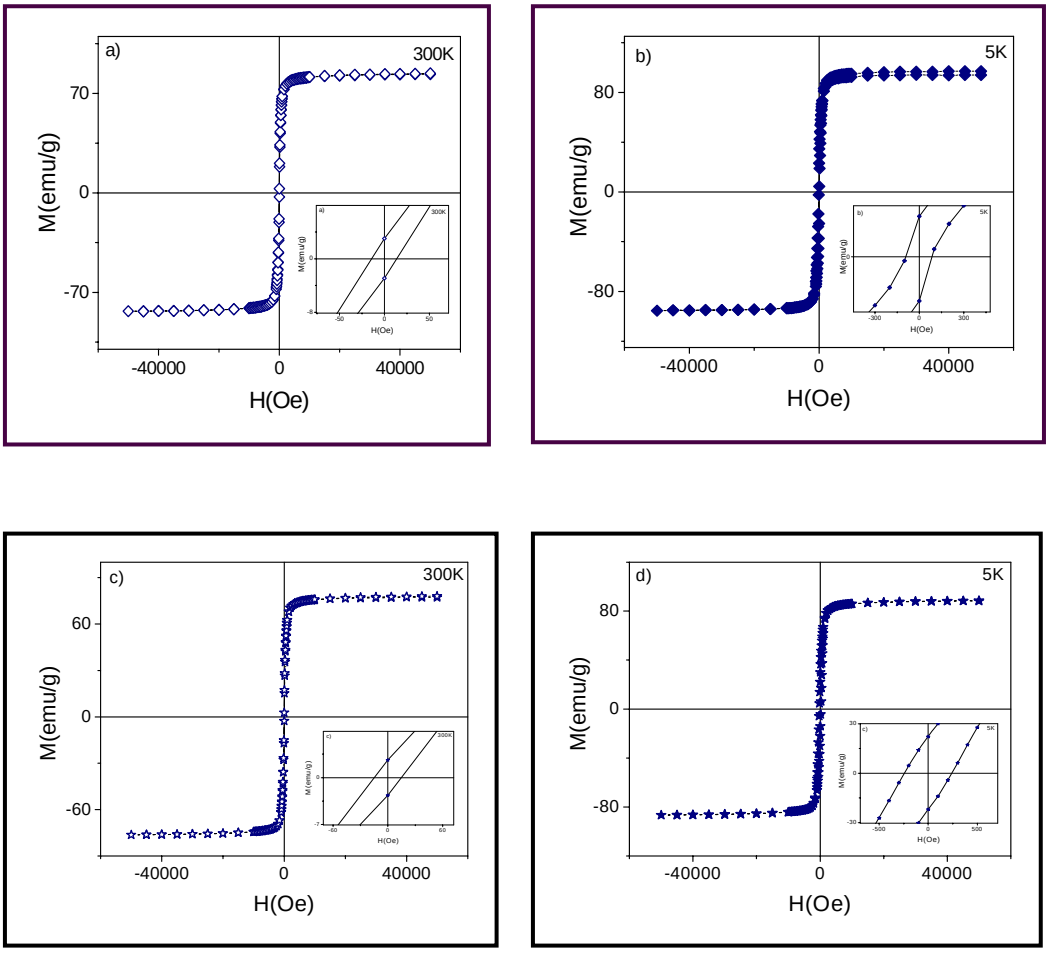

Figure 5.7. Hysteresis loops of as-prepared Fe_3O_4 nanoparticles obtained from a mixture of DEG and NMDEA (3:1, w/w) measured at 300K (a) and 5K (b) and of Fe_3O_4/Au nanocomposite material recorded at 300 K (c) and 5K (d).

Table 5.1. Magnetic Properties of the As-Prepared Fe_3O_4 nanoparticles and the Fe_3O_4/Au Nanocomposite Material

Material	300 K			5 K		
	H_C(Oe)	M_S(emu/g)	SQ	H_C(Oe)	M_S(emu/g)	SQ
Fe_3O_4	14	83.5	0.036	85	94	0.25
Fe_3O_4/Au	14.8	78	0.034	242	88.7	0.25

Fe_3O_4/Au nanopowders exhibit a hysteretic behavior at both temperatures. The coercivity (H_c) and squareness (SQ) are found to increase from H_c = 14.8 Oe and SQ = M_r/M_s = 0.034 at 300 K to H_c = 242 Oe and SQ = 0.25 at 5 K, respectively (Table 5.1.). The magnetic data show that the room temperature saturation magnetization of the 10.5 nm-sized Fe_3O_4 particles is 83.5 emu/g, close to the value of 92 emu/g reported for bulk material.[25] The saturation magnetization of the Fe_3O_4/Au nanocomposites was found to be 78 emu/g at 300 K and 88.7 emu/g at 5K, respectively. The values of M_s for the Fe_3O_4/Au nanocomposites were normalized to the weight of the magnetic core as resulting from the inductive coupled plasma (ICP) experiments. Moreover, the room temperature saturation magnetization of Fe_3O_4/Au nanocomposites is very close to the value of 80 emu/g reported for 3-14 nm Au-Fe_3O_4 dumbbell nanoparticles synthesized by Sun and coworkers[13] and undoubtedly show that the saturation magnetization of Fe_3O_4 nanoparticles is minimally influenced by the immobilization of gold nanoparticles on their surfaces.

5.5. Conclusions

In summary, we describe a simple and feasible sequential approach to immobilize 2-3 nm gold particles onto the chemically modified surface of ~10 nm Fe_3O_4 particles prepared from a non-aqueous, homogeneous solution of diethylene glycol and *N*-methyldiethanol amine (3:1, w/w). The process is size-selective and in the case of Fe_3O_4/Au nanocomposites, both the low concentration and the small size of the gold

particles immobilized on the ~10 nm Fe_3O_4 nanoparticles obscure the gold plasmon peak. The attached gold particles provide chemically active sites on the surface of the magnetite nanocrystals, enabling their potential derivatization with different multifunctional organic molecules. This effective approach can be readily extended to the immobilization of other noble metals onto the chemically modified surface of magnetite nanocrystals, also opening up new potential routes for the functionalization of these nano-ensembles and their further manipulation in specific biochemical applications.

5.6. References

1. Mornet, S.; Vasseur, S.; Grasset, F.; Duguet, E. *J. Mater. Chem*. **2004**, *14*, 2161.
2. Tartaj, P.; Morales, M. P.; Veintemillas-Verdaguer, S.; Gonzales-Carreno, T.; Serna, C. J. *J. Phys. D: Appl. Phys.* **2003**, *36*, R182.
3. Kim, D. K.; Mikhaylova, M.; Zhang, Y.; Muhammed, M. *Chem. Mater.* **2003**, *15*, 1617.
4. Mykhaylyk, O.; Cherchenko, A.; Ilkin, A.; Dudchenko, N.; Ruditsa, V.; Novoseletz, M.; Zozulya, Y. *J. Magn. Magn. Mater.* **2001**, *225*, 241.
5. Knauth, M.; Egelhof, T.; Roth, S. U.; Wirtz, C. R.; Sartor, K. *Am. J. Neuroradiol*. **2001**, *22*, 99.
6. Bergemann, C.; Muller-Schulte, D.; Oster, J.; Brassard, L.; Lubbe, A. S. *J. Magn. Magn. Mater.* **1999**, *194*, 45-52.
7. Roullin, V. G.; Deverre, J. R.; Lemaire, L.; Hindre, F.; Julienne, M. C. V.; Vienet, R.; Benoit, J. P. *Eur. J. Pharm. Biopharm.* **2002**, *53*, 293.
8. Landfester, K.; Ramirez, L. P. *J. Phys.: Condens. Matt*er **2003**, *15*, S1345.
9. Daniel, M.-C.; Astruc, D. *Chem. Rev*. **2004**, *104*, 293.
10. Lyon, J. L.; Flemming, D. A.; Stone, M. B.; Schiffer, P.; Williams, M. E. *Nano Lett.* **2004**, *4*, 719.
11. Mikhaylova, M.; Kim, D. K.; Bobrysheva, N.; Osmolowsky, M.; Semenov, V.; Tsakalatos, T.; Muhammed, M. *Langmuir* **2004**, *20*, 2472.
12. Westcott, S. L.; Oldenburg, S. J.; Lee, T. R.; Hallas, N. J. *Langmuir* **1998**, *14*, 5396.
13. Yu, H.; Chen, M.; Rice, P. M.; Wang, S. X.; White, R. L.; Sun, S. *Nano Lett.*

2005, *5(2)*, 379.

14. Serp, P.; Feurer, R.; Kihn, Y.; Kalck, P.; Faria, J. L.; Figueiredo, J. L. *J. Mater. Chem*. **2001**, *11*, 1080.
15. Zhang, F.; Guan, N.; Li, Y.; Zhang, X.; Chen, J. ; Zhang, H. *Langmuir* **2003**, *19*, 8230.
16. Mandal, S.; Roy, D.; Chaudhari, R. V.; Sastry, M. *Chem. Mater*. **2004**, *16*, 3714.
17. Zhang, F.; Chen, J.; Zhang, X.; Gao, W.; Jin, R.; Guan, N.; Li, Y. *Langmuir*, **2004**, *20*, 9329.
18. Caruntu, D.; Caruntu, G.; Chen, Y.; Goloverda, G.; O'Connor C. J.; Kolesnichenko, V. *Chem. Mater.* **2004**, *16*, 5527.
19. Greenwood, N. N.; Earnshaw, A. *Chemistry of Elements*, 2nd ed.; Butterworth & Heinneman: Oxford, 1997; p 906.
20. Ming; M.; Zhang, Y.; Yu, W.; Shen, H.; Zhang, H.; Gu, N. *Colloids Surf., A* **2003**, *212*, 219.
21. Shen, X. C.; Fang, X. Z.; Zhou, Y. H.; Liang H. *Chem. Lett*. **2004**, *33*, 1468.
22. Duff, D. G.; Baiker, A.; Edwards, P. P. *Langmuir* **1993**, *9*, 2301.
23. Vogel, W.; Duff, D. G.; Baiker, A. *Langmuir* **1995**, *11*, 401.
24. Hou, Y.; Yu, J.; Gao, S. *J. Mater.Chem*. **2003**, *13*, 1983.
25. Cornell, R. M.; Schwertmann, U. *The Iron Oxides: Structure,Properties, Reactions, Occurrence and Uses*; VCH: New York, 1996.

VITA

Daniela Caruntu was born on October 4, 1969 in Suceava (Romania). She graduated from "Petru Rares" High School in Suceava (Romania) in 1988 and was valedictorian. She performed her undergraduate studies at the "Al. I. Cuza" University in Iasi (Romania) and graduated in 1993 as the third of 98 students with a B. S. in Chemistry. During her undergraduate studies she was recipient of the Romanian Government Fellowship for Outstanding Undergraduate Studies. In 2003 she earned a M.S. in Chemistry at the University of New Orleans with a thesis describing the reactivity of the 3d transition metal cations in diethylene glycol solutions. Her graduate work was directed by Professor Charles J. O'Connor at the Advanced Materials Research Institute in New Orleans, Louisiana. She graduated with a PhD in Chemistry in 2006.